

Advances in Non-Planar Electromagnetic Prototyping

by

Isaac M. Ehrenberg

B.A., Yeshiva University (2005)

S.M., Massachusetts Institute of Technology (2009)

Submitted to the Department of Mechanical Engineering
in partial fulfillment of the requirements for the degree of

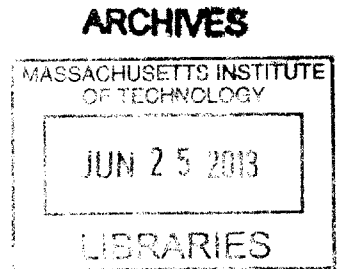
Doctor of Philosophy in Mechanical Engineering

at the

MASSACHUSETTS INSTITUTE OF TECHNOLOGY

June 2013

©Isaac Ehrenberg, 2013.



The author hereby grants to MIT permission to reproduce and to distribute publicly paper and electronic copies of this thesis document in whole or in part in any medium now known or hereafter created.

Author
Department of Mechanical Engineering
April 12, 2013

Certified by
Sanjay E. Sarma
Fred Fort Flowers and Daniel Fort Flowers Professor of Mechanical
Engineering
Thesis Supervisor

Accepted by
David E. Hardt
Chairman, Department Committee on Graduate Theses

Advances in Non-Planar Electromagnetic Prototyping

by

Isaac M. Ehrenberg

Submitted to the Department of Mechanical Engineering
on April 12, 2013, in partial fulfillment of the
requirements for the degree of
Doctor of Philosophy in Mechanical Engineering

Abstract

The advent of metamaterials has introduced new ways to manipulate how electromagnetic waves reflect, refract and radiate in systems where the range of available material properties now includes negative permittivity, permeability, and refractive index. While analytical and numerical tools are equipped to analyze the complex configurations of materials and geometry that constitute many proposed devices, realizations have been limited in part due to fabrication. The fabrication processes used to construct the majority of metamaterial media are optimized to produce 2D products, including printed circuit board and microfabrication techniques, making the transition from two dimensional proof-of-concept to three dimensional prototype challenging.

In the last decade, several reports have documented the use of additive manufacturing to fabricate 3D electromagnetic devices, including gradient index lenses at both microwave and optical frequencies, and radio frequency lenses that attain resolution beyond the diffraction limit. Though primarily used for facsimile display models, additive manufacturing is uniquely capable of addressing the needs of 3D electromagnetic designs which incorporate non-planar geometries and material inhomogeneity. The application of additive manufacturing to functional electromagnetic devices, however, is still uncommon, as the simultaneous layering of conductive and insulating materials remains complicated.

To further advance the state of the art, we report our application of additive manufacturing in conjunction with other fabrication tools to fabricate several electromagnetics devices. The first involved the design of an artificial magnetic conducting substrate to enhance UHF RFID tags in close proximity to metal surfaces, which normally detune antennas and destructively interfere with any transmitted waves. The substrate incorporates 3D metamaterial unit cells, the fabrication and assembly of which were enabled by additive manufacturing. Additive manufacturing was then used to fabricate lightweight, self-supporting interconnected metamaterial structures. These structures exhibited minimal losses, making them ideal for a plano-concave microwave lens capable of focusing at 10GHz with the highest gain measured for a metamaterial lens to date. Other achievements include the fabrication of frequency selective surfaces and antenna elements conformal to non-planar surfaces. Though many challenges remain to be overcome, it is clear that additive manufacturing has significant potential to contribute to the study and fabrication of electromagnetic elements.

Thesis Supervisor: Sanjay E. Sarma

Title: Fred Fort Flowers and Daniel Fort Flowers Professor of Mechanical Engineering

Acknowledgments

It is with boundless appreciation that I acknowledge the many individuals that have aided, encouraged and inspired me to undertake and ultimately complete my graduate education in general and this thesis in particular.

Credit first goes to my Organic Chemistry teacher Prof. Bruce Hrnjez for suggesting that this Yeshiva boy apply to MIT, and Rosalyn Falk for ensuring the quality of that application. Upon acceptance, Lesley Regan and Joan Kravit both greeted me with warmth that has yet to dissipate despite the New England weather but which they periodically recharge regardless. It was they who directed me to Prof. Rohan Abeyaratne, whose door was always open during those overwhelming months before I joined Sanjay's lab.

After my initial conversation with Professor Sanjay E. Sarma, he told me to read two theses and call him in the morning. Two theses later, Sanjay's maniacal cunning and unwavering support continue to cultivate an atmosphere of camaraderie, education and innovation which I consider myself fortunate to have experienced. Despite his humble assertions to the contrary, neither thesis would have been possible without him.

Though one's own advisor has a vested interest in ensuring the success of his student's work, I am particularly grateful to Professors Timothy Gutowski and Nicholas Fang, who volunteered to serve as members of my thesis committee. They were generous with their time, complimentary of my research and always constructive with their criticisms.

In the end of the day, I owe much to the post-doctoral fellows, students and staff that populated the MIT Auto-ID Laboratory before and during my tenure as an MIT student, including Drs. Christian Floerkemeier, supervisor of my master's research, Stephen Ho, who among his other important duties diligently read a draft of this thesis, Ajay Deshpande, who is the only explanation of how I came to pass Dynamics, Sriram Krishnan, who answered the call on many occasions to assist my research and writing efforts in any way that he could, and Rahul Bhattacharyya, lab mate par excellence. Thanks also go to the ace Sumeet Kumar, for his help with the organization of this thesis, the magical powers of Dylan Erb, as well as Kat Donnelly, Austin Oehlerking, Justin Miller, Long Phan, Abraham Rosenfeld, and Erik Wilhelm, who all played a part, and Joshua Siegal, who coached me when it counted.

Despite spending a significant portion of my time at MIT on the second floor of Building 35, most of the heavy lifting that went into this thesis was done in the LMP machine shop with the help of David Dow and Patrick McAtamney, in the Edgerton student shop run by the one and only Mark Belanger, and at the MIT Microsystems Technology Laboratories under the supervision of Eric Lim and Kurt Broderick. It was the energy, kindness and concern of these unique individuals that made getting my research done both possible and enjoyable.

Indispensable contributions were made to every chapter of this thesis by Dr. Bae-Ian Wu. I first met Dr. Wu in the spring of 2007 while taking 6.013 with our teacher Prof. Jin Au Kong, of blessed memory, and since then his patience, perfectionism and his insistence on making the second effort pushed me through to the end and beyond.

In addition to those above, I must acknowledge the Jewish communities at MIT, Harvard, BU, Brookline, M.A. and the surrounding cities that provided me with the infrastructure needed to function as an Orthodox Jew while in graduate school. Particular thanks are due to many friends near and far including the Barabans, Eleffs, Untermans, Zytos, Rabbi Levi Altein, Erez Lieberman, Rabbi Gershon Segal, Jordan Whistler and many, many others.

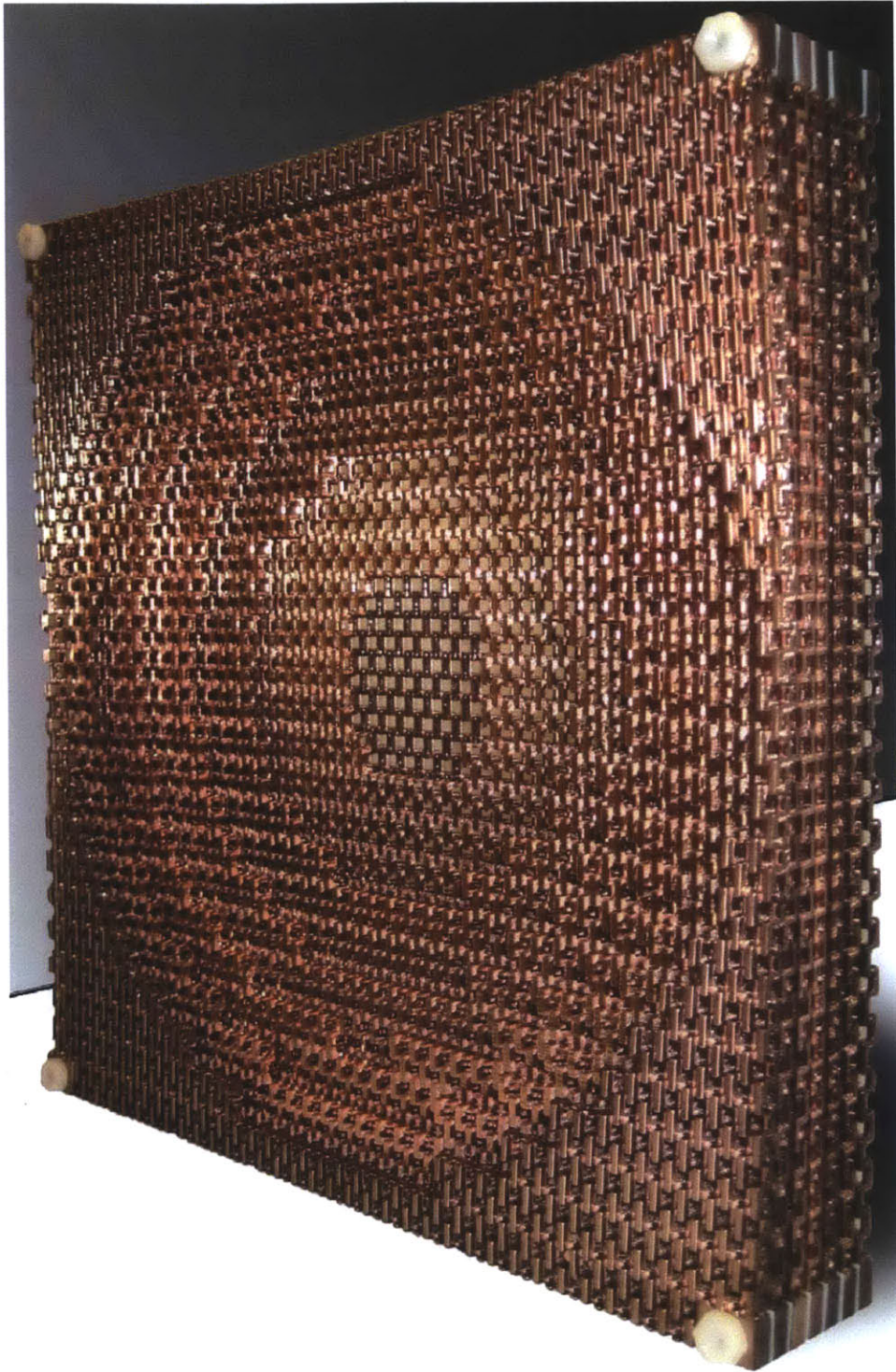
My entire family has always been a source of inspiration and strength, from my grandmothers Bubby Genie and Bubby Sylvia, may they live and be well, to my nieces and nephews, with all my aunts, uncles, siblings and cousins in between. I hope and pray that our family continues to grow together.

My wife Rahel has displayed remarkable fortitude over the last few years as I struggled to put together this thesis. While some credit for her resolve is attributable to the beautiful example set by her parents who prepared her so well for what to expect as the spouse of an MIT PhD student, I dedicate this thesis to Rahel in recognition of the uncountable frustrated hours for which it kept me distant from her, the faith she had in me that I would eventually prevail, and her desire for us to excel in all aspects of our lives.

Finally, I cannot begin to elaborate on the gratitude and appreciation I have towards my parents. I know it not for this thesis, nor this degree, for which they are most proud.

for Rahel,

words of pleasantness are a honeycomb, sweet to the soul and healing to the bone



Contents

1	Introduction	13
1.1	The Role of Geometry and Material Parameters in Electromagnetic Systems	14
1.1.1	Geometry Control	15
1.1.2	Material Property Control	16
1.2	Material Parameter Control with Metamaterials	18
1.2.1	Challenges in Using Metamaterials	20
1.3	Thesis Contributions	21
1.4	Thesis outline	22
2	Metamaterial Electromagnetics and Fabrication	23
2.1	Derivation of Constitutive Parameters for Metamaterial Structures	23
2.1.1	Analytic Approach	24
2.1.2	Parameter Extraction from Reflection and Transmission Data	27
2.2	Review of Metamaterial Fabrication	30
2.2.1	Common Fabrication Processes for Metamaterial Structures	31
2.2.2	Multilayer and Non-Planar Metamaterial Fabrication	34
2.3	Additive Manufacturing for Complex 3D metamaterials	35
2.3.1	List of Additive Processes	36
2.3.2	Process Capabilities and Limitations	37
2.3.3	Additively Manufactured Metamaterials	38
2.3.4	Surface Modification of Additively Manufactured Structures	39
2.3.5	Usage of Additive Manufacturing in this Thesis	39
2.4	Chapter Conclusions	40

3	Artificial Reflection in Depth	41
3.1	RFID Background	41
3.1.1	RFID Physics	42
3.2	The RFID Metal Problem	44
3.2.1	Possible Solutions to the Metal Problem	44
3.2.2	The Ideal Solution	47
3.3	The AMC solution	48
3.3.1	AMC for UHF RFID	50
3.3.2	Related Work	51
3.3.3	New Unit Cell Design	52
3.3.4	Initial Prototype Fabrication and Characterization	53
3.3.5	Antenna Simulations	56
3.3.6	Antenna Experiments	57
3.3.7	Extension to RFID frequencies	59
3.3.8	Unit Cell Redesign	60
3.4	Conclusions	67
3.4.1	AMC Implications	68
3.4.2	Fabrication Implications	68
4	Lost in Transmission	69
4.1	Motivation for 3D Structures: Minimization of Loss	70
4.1.1	Self-Supporting Metamaterial Designs	70
4.2	S-Ring Metamaterial Unit Cell	71
4.2.1	Early S-ring Examples	72
4.2.2	Additively Manufactured S-Rings	72
4.2.3	Fabrication and Testing	73
4.3	S-Ring Metamaterial Lens	75
4.3.1	Negative Index Lenses	76
4.3.2	Related Metamaterial Lens Work	77
4.3.3	S-Ring Lens Design	79

4.3.4	Lens Fabrication	80
4.3.5	Single Layer Transmission	85
4.3.6	Copper Lens Evaluation	86
4.4	Conclusion	90
5	Conformable Coverage and Orthomorphic Radiance	91
5.1	Introduction	91
5.2	Conformal Masking	94
5.2.1	Other Masking Methods	94
5.2.2	A Non-Conformist Solution	95
5.3	Conformal FSS	96
5.3.1	FSS Applications	96
5.3.2	State of the Art FSS Fabrication	97
5.3.3	FSS Unit Cell Design	98
5.3.4	Conformal FSS Design	99
5.3.5	Conformal FSS Fabrication	101
5.3.6	FSS Evaluation	107
5.4	Conformal Antenna Array	108
5.4.1	Non-planar Substrate	109
5.4.2	Planar and Conformal Patch Antenna	110
5.4.3	Array Antenna Simulations	114
5.4.4	Fabrication	119
5.4.5	Antenna Array Testing	121
5.5	Conclusion	122
6	Conclusion	125
6.1	Metamaterial Fabrication	125
6.2	Summary of Contributions	126
6.3	Future Work	127
6.3.1	Thin AMC Manufacturing	127
6.3.2	Self-Supporting Metamaterials Devices	128

6.3.3 Conformal Masking Process Development 128
6.3.4 Combining 3D and Non-Planar 129
6.3.5 Changing the Mindset 130

Chapter 1

Introduction

In this thesis, I study the fabrication of three-dimensional (3D) and conformal geometries and their affect on how electromagnetic waves reflect, refract and radiate. Recent innovations in areas such as communications, imaging, defense and security have generated significant interest in a wide array of 3D and conformal electromagnetic structures, sought after for their unique and often unnatural electromagnetic characteristics that are advantageous to both traditional and emerging applications [1, 2, 3].

I begin this introductory chapter by describing the components of a generic electromagnetic system, and how the behavior of electromagnetic waves in that system is a function of both geometry and material parameters. After giving examples of how electromagnetic devices incorporate both geometry and material parameters, I discuss the recent development of metamaterials, which have introduced a new level of control in electromagnetic system design. I then review several proposed metamaterial applications that have redefined the limits of conventional electromagnetics, but remain difficult to realize in practice partly due to complications associated with fabrication. This chapter concludes with a summary of the thesis contributions, and an outline for the remainder of the thesis.

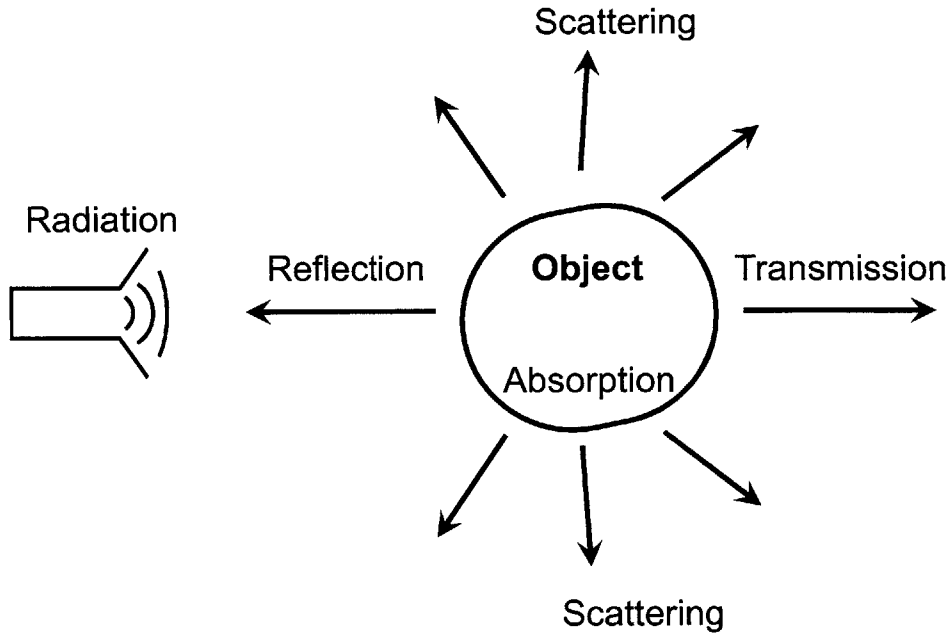


Figure 1-1: A generic electromagnetic system consisting of a radiation source and an object. When radiation emitted from the source is incident upon the object, it results in reflection, transmission, absorption and scattering.

1.1 The Role of Geometry and Material Parameters in Electromagnetic Systems

The electromagnetic system sketched in Fig. 1-1 depicts an object illuminated by electromagnetic waves emanating from a radiation source. When incident waves from the source encounter the object, the result is a combination of reflection, scattering, absorption and transmission. The nature of these phenomena is described by Maxwell's Equations

$$\nabla \times \mathbf{H} = \mathbf{J} + \epsilon \frac{\partial \mathbf{E}}{\partial t} \quad (1.1)$$

$$\nabla \times \mathbf{E} = -\mu \frac{\partial \mathbf{H}}{\partial t} \quad (1.2)$$

$$\nabla \cdot \mathbf{E} = \frac{\rho}{\epsilon} \quad (1.3)$$

$$\nabla \cdot \mathbf{H} = 0 \tag{1.4}$$

where \mathbf{E} and \mathbf{H} are the electric and magnetic fields, \mathbf{J} is the current density, ρ is the charge density, and ϵ and μ are the permittivity and permeability of the medium. When fully solved, Maxwell's Equations reveal the time changing electric and magnetic fields of the entire system. The inputs required to solve for all the unknowns in these equations are initial conditions of any source terms, boundary conditions and material parameters. Considering the scenario of Fig. 1-1, boundary conditions and material parameters refer to the overall geometry and constituent materials that make up the radiant antenna, the incident upon object, and the background environment. The geometry and material makeup of these three elements afford an avenue to influence electromagnetic fields, and design an electromagnetic system to produce specific outcomes. While any outcome is the result of many intertwined physical factors, in the following sections we will highlight several examples of how geometry and material parameters individually can provide control over different aspects of an electromagnetic system.

1.1.1 Geometry Control

Radiation from Antennas

The crucial role played by geometry in the design of radiative system components is apparent from the fact that many antenna properties are dependent on geometry, resulting in different antenna types for different applications. Towering mast antennas are used to broadcast long wavelength signals for AM or FM radio stations, while arrays of smaller patch antennas optimized for transmitting and receiving at much shorter wavelengths sit atop cell phone towers. Aside from operation frequency, physical dimensions are also important for key antenna performance parameters such as bandwidth and gain, and the overall radiation pattern.

Reflection off Reflectors

While control over antenna geometry can go a long way towards building a functional system, propagating electromagnetic waves often require redirection, which can be achieved through the proper design of reflectors. Reflectors are surfaces shaped to reflect incident waves in a particular way. A common example is a parabolic reflector dish, which are used in many applications such as radio astronomy and satellite television. These same curved dishes can also be used to redirect and collimate, or spread out, the signals of radiation sources.

Transmission Through Lenses

When reflection is impractical, transmissive devices can be used to redirect electromagnetic waves. Transparent objects with properly configured surface curvatures, referred to as lenses, can focus or spread incident radiation. Tight control over surface geometry allows focal lengths to be optimized for purposes such as imaging or tumor ablation. One example of such a lens is the human eye, which constantly refocuses on objects near and far as muscles alter the shape of its lens.

Scattering for Stealth

Scattering is often an undesired byproduct in systems designed to reflect or transmit, with the misdirection of waves caused by imperfections in surface geometry. Though care is taken during the fabrication process for many applications to reduce surface roughness and limit scattering, other applications such as stealth technology rely on increased scattering and reduced reflection. By scattering most of the energy away from a mono-static radar station, the radar cross section of an object can be significantly reduced to help avoid detection.

1.1.2 Material Property Control

While the previous section focused on the relationship between function and geometry, materials and their properties also play a crucial role in electromagnetic system design. The electromagnetic material properties used for system design are:

- Permittivity (ϵ), which includes the electrical properties of free space and the ratio of the electric dipole moment per unit volume of the material. The electric dipole moment can be permanent, or induced by the migration of electric charges [4].
- Permeability (μ), which includes the magnetic properties of free space, and the permanent or induced magnetic moments within the material.

Permittivity and permeability together describe how electromagnetic waves interact with materials, including the velocity v at which waves travel through material,

$$v = \frac{c}{\sqrt{\mu\epsilon}}, \quad (1.5)$$

where c is the speed of light in vacuum, the wavelength λ with which they travel

$$\lambda = \frac{c}{\omega\sqrt{\mu\epsilon}}, \quad (1.6)$$

where ω is the angular frequency, how quickly energy is absorbed within a material, and wave behavior at the interface of two different materials. All these material effects and their consequences need to be considered when designing an electromagnetic system.

Material Effects on Radiation

While many antennas consist of metallic radiative elements, materials surrounding those elements can have a significant impact on antenna parameters. For example, a substrate with a high dielectric constant can lower the resonance frequency and bandwidth of a patch antenna. Dielectrics are also used as radiating elements themselves, especially at higher frequencies where metals radiate less efficiently.

Dielectric Reflection

The precise arrangement of materials with different properties can be used to build reflective elements. By properly layering materials of higher and lower dielectric constants, waves incident on a material boundary above the critical angle can be forced to undergo total

internal reflection. This effect is useful for the guiding of waves in fiber optic cables, or the construction of highly reflective dielectric mirrors and quarter wave elements.

Transmission through Dielectrics

Material parameters are also important for the design of transmissive devices. Lens properties such as focal length are dependent on the material's refractive index in addition to the lens surface curvature. Lenses made from higher refractive index material have shorter focal lengths than lenses with lower indices.

Reduced Scattering with (Lossy) Materials

Aside from geometric considerations, scattering can be controlled and reduced through the incorporation of radar absorbent materials. These materials often have permeabilities that feature a significant imaginary part. In the process of absorbing the incident radiation, reflection and transmission are also reduced, which can be useful for stealth or electromagnetic noise cancellation purposes.

1.2 Material Parameter Control with Metamaterials

The recent development of electromagnetic metamaterials has provided additional freedom to electromagnetic system designers by extending the range of available material parameters. Natural and synthetic bulk materials only provide a limited range of permittivity and permeability values, mostly concentrated in the top right quadrant of Fig. 1-2. In contrast, metamaterials have shown extreme or unique electrical properties not previously observed in natural materials [5]. To generate these unnatural material properties, metamaterials incorporate heterogeneous mixtures of different materials, often in intricate predetermined geometric patterns. These constructs interact with incident electromagnetic waves and change the response of the composite material to something different than the constituent bulk materials. By purposefully designing the size, shape, periodicity and material of any inclusions, researchers have introduced new ways of controlling how electromagnetic waves radiate, reflect, transmit and scatter.

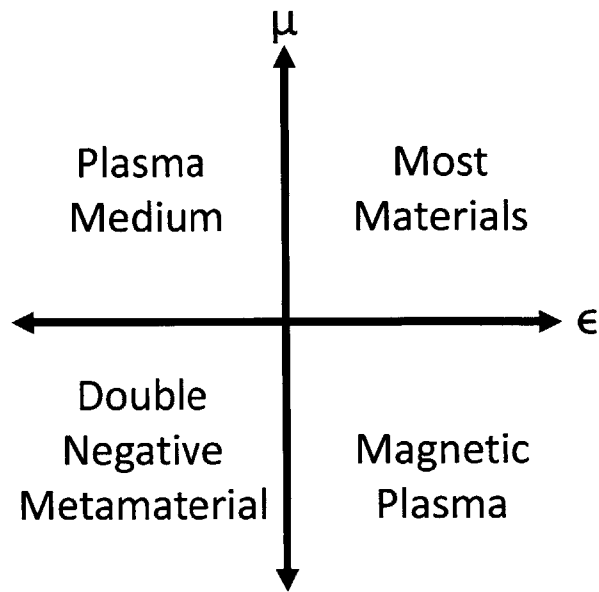


Figure 1-2: The range of electromagnetic parameters, with most materials belonging to the upper right hand quadrant, and double negative metamaterials existing in the bottom left hand quadrant.

Altering Radiation with Metamaterials

Several studies show how metamaterials can be used to affect antenna properties [6, 7, 8, 9]. In one example, a spherical shell structure was designed to alter the radiation pattern of an antenna so that it mimics the pattern of an antenna with a larger aperture [10]. The proposed method applied to generate this aperture transformation also provides a methodology for designing antennas with arbitrarily high levels of directivity.

Artificial Reflection Surfaces with Metamaterials

Metamaterials have been used to alter the properties of reflective surfaces [11, 12]. Normally, metal surfaces reflect electromagnetic waves with an added phase of 180° . However, by covering the surface with a thin layer of metamaterial, the phase accrued by the reflected waves can be precisely controlled. This allows for the design of reflectors without large curvatures, and other substrates that are beneficial for near metal antenna designs [13, 14].

Enhanced Transmission with Metamaterials

Lenses made from regular materials are useful for focusing and imaging but their resolution is capped by the diffraction limit, which sets the minimum spot size for imaging through a lens [15]. Lenses made from metamaterials, however, are not subject to the same diffraction limit [16]. Several studies have confirmed that lenses made from slabs of metamaterial with a refractive index of $n = -1$ are capable of imaging point sources with sub-diffraction limited resolution, or super-resolution [17, 18].

Reduced Scattering with Metamaterials

Metamaterials can also be used to completely eliminate unwanted reflections and scattering. Other scattering reduction methods which redirect or absorb incident waves are only capable of evading detection by mono-static radar systems, where the source of the radar signal is also the detector. In the mono-static case, as long as reflected or scattered waves don't return to the radar antenna, the stealth object remains undetected. These methods fail in the case of bi-static detection systems, which act like trip-wires by detecting changes or interruptions to transmitted signals. To avoid detection in this scenario, a metamaterial shell can be designed to surround an object and redirect all the incident radiation so that the signal can be transmitted without any scattering. Metamaterials designed for this purpose are called invisibility cloaks, as they render a would-be scatter invisible to incoming radiation [19, 20].

1.2.1 Challenges in Using Metamaterials

Though metamaterials have been a topic of great interest to the electromagnetics community for over a decade, there remain significant issues that need to be overcome before metamaterials can realize their potential to greatly enhance electromagnetic systems and enable new devices.

- Loss: Many metamaterials suffer from significant losses that preclude their use in practical devices. One source is ohmic loss, or energy dissipated as a result of current flow through materials with a finite conductivity. Ohmic loss is particularly problematic in metamaterials that contain metallic inclusions and are active around resonances

which generate high currents and field levels. Non-conductive dielectrics are a second source of loss, causing impedance mismatches that result in unwanted reflections, and propagation losses as transmitted waves propagate through the material [21].

- **Bandwidth:** For any particular design and prototype, metamaterial properties are only observed over a finite frequency band. This is typical of the resonance phenomenon inherent to many designs, where the resonance frequency and quality factor are highly dependent on the physical dimensions of metamaterial inclusions. Bandwidth is also limited by the frequency response of the constituent materials used to fabricate the metamaterial [22, 23].
- **Fabrication:** Metamaterials fabrication is challenging because it requires complex patterns involving at least two materials with different properties. The task of creating such patterns lends itself to layered manufacturing processes. Layered processes, which are usually combinations of selective 2D additions and subtractions of material using combinations of patterns, binders, resists and etchants, have understandably been the most common approaches to metamaterial fabrication in the literature. While 2D metamaterials have been successfully fabricated and used to demonstrate interesting phenomena, many metamaterial designs and applications such as those mentioned above require non-planar and 3D geometries, which can be difficult to achieve with standard 2D fabrication techniques.

1.3 Thesis Contributions

In this thesis, I propose both new 3D designs and the use of alternative fabrication methods to overcome some of the challenges and limitations imposed by conventional methodologies on the fabrication of metamaterials. My specific contributions are:

- The fabrication of a new 3D metamaterial unit cell for use with planar dipole RFID tag antennas.
- The fabrication of a lightweight, self-supporting plano-concave 3D metamaterial lens with low loss.

- Proposal of a new methodology called “Conformal Masking” for conformal electromagnetic fabrication on curvilinear surfaces.
- The fabrication of a conformal frequency selective surface using a conformal mask.
- The fabrication of a conformal patch antenna array using a conformal mask.

1.4 Thesis outline

The remainder of this thesis is organized as follows. Chapter 2 gives a brief tutorial on the electromagnetics of metamaterials and overview of the techniques used to fabricate 2D and 3D metamaterials, with a focus on additive manufacturing techniques which are utilized in subsequent chapters. In chapter 3, as a motivation for the study of metamaterial reflection enhancement, I present a brief discussion of the problems encountered when operating RFID tags in close proximity to metal surfaces. That is followed by an analysis of a potential metamaterial solution to the RFID metal problem, and the proposal of a 3D metamaterial design and its fabrication. In chapter 4, I present an overview of the challenges faced by transmission based metamaterial designs, followed by the fabrication and implementation of a self-supporting lightweight plano-concave lens built from 3D metamaterial unit cells. In light of the fabrication insights garnered from the previous chapters, chapter 5 introduces a new method for the fabrication of conformal electromagnetic structures. This method is then used for the fabrication of a conformal frequency selective surface (FSS) and conformal patch antenna array. I conclude with a review of the thesis contributions, and future directions for this work in Chapter 6.

Chapter 2

Metamaterial Electromagnetics and Fabrication

To place the design and fabrication of metamaterials and other electromagnetic structures in context, I begin this chapter with a brief tutorial on the electromagnetics of metamaterials. Using the example a split-ring resonator, I derive relative material parameters from both an analytic and simulation perspective.

Following the tutorial is a review of common manufacturing methods utilized to fabricate metamaterial structures. I then discuss the use of additive manufacturing processes as a means of prototyping complex 3D metamaterials structures and other electromagnetic devices. Though the primary focus of these additive techniques in the past has been mechanical design, in this thesis I leverage the flexibility afforded by such processes to further the boundaries of electromagnetic device design and fabrication.

2.1 Derivation of Constitutive Parameters for Metamaterial Structures

Maxwell's Equations as presented in Section 1.1 are the fundamental laws governing electromagnetic fields in both free space and within materials. The material parameters ϵ and μ that appear in those equations are abstractions that encapsulate the effect of matter on

electromagnetic fields or propagating waves relative to the electric and magnetic effects of free space, which are universal physical constants represented by ϵ_0 and μ_0 .

In the case of bulk materials, the contributing factors to ϵ and μ are sub-atomic, atomic and molecular structures. For metamaterials, the contributing factors to ϵ and μ are instead the result of properly designed and oriented mixtures of bulk materials. In some situations, it is possible to analytically derive ϵ and μ of metamaterials from first principles. When analytical methods are not available, ϵ and μ maybe be extracted from relative measurements or simulations. In the following two sections, the effective permeability of a split ring resonator will be derived according to both of these approaches [24, 4].

2.1.1 Analytic Approach

Consider an infinitely periodic 2D array of split ring resonator cells, where at the center of each unit cell rests a split ring of radius R (Fig. 2-1). The unit cells are square and have a dimension of l . The fractional area encompassed by the ring is $f = \frac{\pi R^2}{l^2}$, and the free space in and around the ring is characterized by ϵ_0 and μ_0 .

Let H_0 be a time-harmonic magnetic field. Without the existence of any split rings, the application of H_0 would result in an unperturbed magnetic field throughout the cell. However, when applied in the presence of the split rings, H_0 induces a surface current J_s along the ring, and a strong electric field E_2 between the gaps oriented in the direction of the current flow. According to the boundary conditions imposed by Maxwell's Equations, the induced current J_s is the difference between the external magnetic field and magnetic

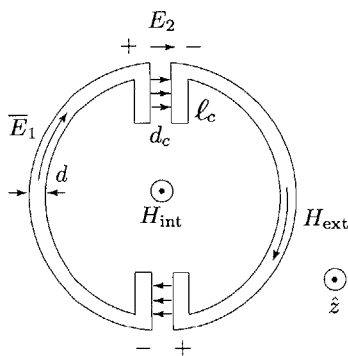


Figure 2-1: A split ring resonator proposed by O'Brien [24].

field inside to the ring radius

$$J_s = H_{ext} - H_{int}. \quad (2.1)$$

The split ring causes an inhomogeneity which complicates the magnetic field within the cell. To simplify the characterization of the magnetic field, we use a homogenization law and utilize an effective bulk permeability μ_{eff} to average the external and internal fields over the area of the cell [25, 24],

$$\mu_{eff}H_{ext} = fH_{int} + (1 - f)H_{ext}. \quad (2.2)$$

We can thus define the effective permeability as

$$\mu_{eff} = \frac{fH_{int} + (1 - f)H_{ext}}{H_{ext}} = \frac{H_{ext} - fJ_s}{H_{ext}} = \left[1 - \frac{fJ_s}{J_s + H_{int}} \right] \quad (2.3)$$

To relate J_s directly to H_{int} , we apply Faraday's law, this time in the integral form,

$$\oint_C E \cdot d\vec{l} = - \int \int \frac{\partial \mu_0 \vec{H}}{\partial t} \cdot d\vec{S} \quad (2.4)$$

where the contour C is the ring's circumference enclosing the area S when d is infinitely small. Assuming the ring is made of perfect conductor such that there is no electric field within the ring structure itself and $E_1 = 0$, the only contributions to the right side of Eq. 2.4 come from the fields within the gaps,

$$\oint_C E \cdot d\vec{l} = -2dE_2 \quad (2.5)$$

corresponding to the voltage accumulated when following the closed contour. Assuming H_{int} is uniform within the ring, the right side of Eq. 2.4 becomes

$$- \int \int \frac{\partial \mu_0 \vec{H}}{\partial t} \cdot d\vec{S} = i\omega\mu_0\pi R^2 H_{int} \quad (2.6)$$

which results in

$$-2dE_2 = i\omega\mu_0\pi R^2 H_{int} \quad (2.7)$$

relating E_2 to H_{int} .

We then apply boundary conditions along the ring gap, which relates the charge density along the ring edge ℓ_c to a difference in the divergence field D normal to the edge of the ring, we get

$$\hat{n} \cdot (\bar{D}_1 - \bar{D}_2) = \rho_s \quad (2.8)$$

where ρ_s is the charge per unit length. Since there is no field within the ring, the equation becomes

$$D = \rho_s. \quad (2.9)$$

Multiplying both sides by ℓ_c and taking the time derivative of this time-harmonic system where $\frac{d}{dt} \rightarrow i$, we get

$$J_s = \ell_c \frac{dD}{dt} = \ell_c \epsilon_0 \frac{dE}{dt} = -i\omega \ell_c \epsilon_0 E \quad (2.10)$$

If we now let $L = \mu_0\pi R^2$ and $C = \epsilon_0 l/2d$ and plug them into μ_{eff} the result is

$$\mu_{eff} = \left[1 - \frac{fJ_s}{H_{ext}}\right] = \left[1 - \frac{f\omega^2}{\omega^2 - \omega_0^2}\right] \quad (2.11)$$

where $\omega_0^2 = \frac{1}{LC}$. After choosing physical parameters ($l = 2.024$ mm, $R = 1$ mm, $\ell_c = 0.875$ mm and $dc = .01$ mm), we can plot Eq. 2.11, and observe that this configuration features an effective permeability that is negative in the frequency range $\omega_0^2 < \omega^2 < \omega_0^2/(1-f)$ (Fig. 2-2).

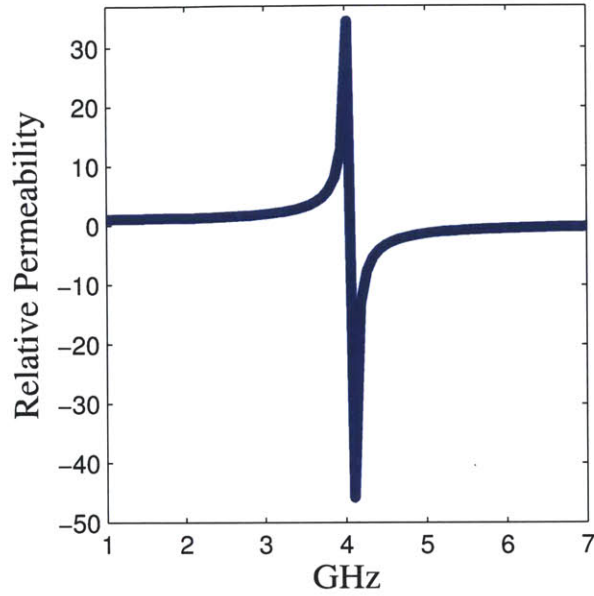


Figure 2-2: The relative permeability of the split ring configuration, which is negative in the post resonance region just above 4 GHz, as calculated using Eq. 2.11.

2.1.2 Parameter Extraction from Reflection and Transmission Data

In addition to analytical derivations, experiments and simulations are also useful for analyzing metamaterial structures. Data from experiments or simulations can be used to observe metamaterial behavior and verify analytical models such as the one in the previous section, or provide an initial estimate of the relative parameters when an analytical model is not available.

We will now review the procedure for extracting the unknown relative permittivity and permeability of a periodic metamaterial structure. Consider a plane wave normally incident upon a medium (Fig. 2-3), which consists of three regions. Region 1 and Region 3 are both free space, represented by ϵ_0 and μ_0 . Region 2 is a metamaterial featuring unknown ϵ and μ , but it has a known thickness d . When the plane wave encounters the boundary between Regions 1 and 2, it results in both reflection R and transmission T determined by

$$R = \frac{1 - \frac{\mu_1 k_2}{\mu_2 k_1}}{1 + \frac{\mu_1 k_2}{\mu_2 k_1}} \quad (2.12)$$

$$R + T = 1 \quad (2.13)$$

where the wavenumber $k_{nx} = \omega\sqrt{\mu_n\epsilon_n}$ within each region.

While the reflected wave no longer encounters any media other than free space, the transmitted wave continues until it reaches the boundary of Regions 2 and 3. What is transmitted at this juncture continues to propagate through Region 3, but the reflected component redirects back towards the boundary of Regions 2 and 1, and the process repeats. The sum of all the reflection and transmission terms is:

$$R_{total} = \frac{R_{01} + R_{12}e^{i2k_2d}}{1 + R_{01}R_{12}e^{i2k_2d}} \quad (2.14)$$

$$T_{total} = \frac{T_{01}T_{12}e^{ik_2d}}{1 + R_{01}R_{12}e^{i2k_2d}}, \quad (2.15)$$

where R_{ab} and T_{ab} represent the reflection and transmission coefficients at that boundary of Regions a and b . If R_{total} and T_{total} are known from a simulation or experiment, then we can use these equations to extract the unknown ϵ and μ from Region 2.

As an example, a simulation of the split ring with the same parameters as before was performed using Ansoft HFSS, a commercially available FEM solver for electromagnetic

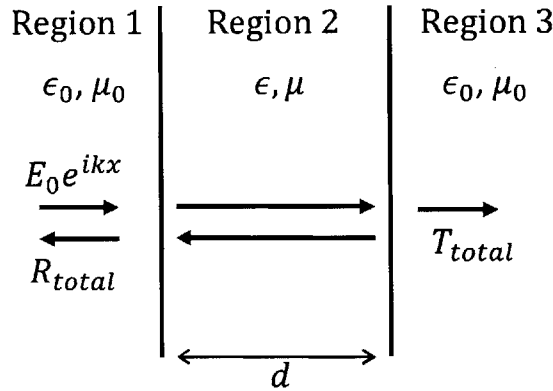


Figure 2-3: A plane wave is incident upon a layered medium, the middle of which contains a split ring array and is of unknown permeability and permittivity. The unknown parameters can be extracted if the total reflection and transmission through the medium is known by way of experiment or simulation.

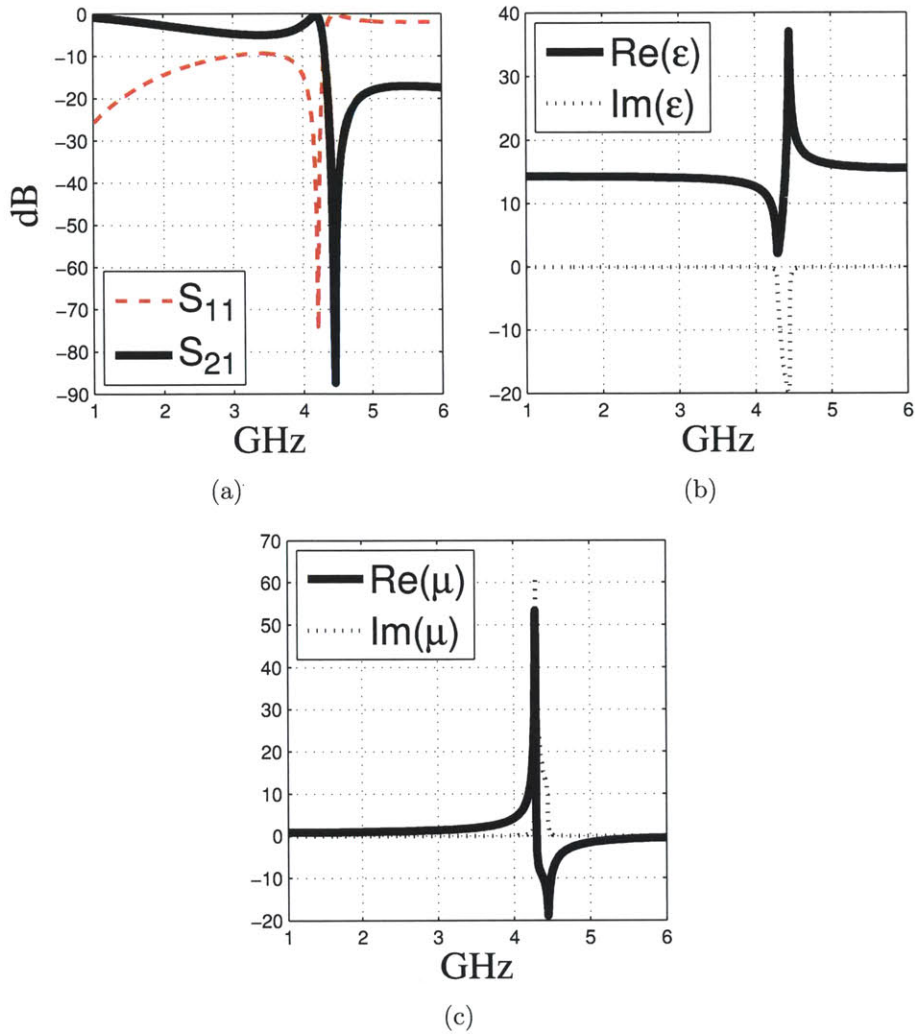


Figure 2-4: (a) The S-parameter output from a split ring simulation which was used to retrieve the relative (c) permittivity and (b) permeability of the split ring medium.

systems. The split ring was oriented along the y-axis and illuminated by a plane wave propagating along the x-axis. Periodic boundary conditions were applied along the y-axis and z-axis to simulate the effects of an array configuration. Reflection and transmission are reported as S_{11} and S_{21} , from which the relative permeability and permittivity can be extracted (Fig. 2-4).

2.2 Review of Metamaterial Fabrication

While theory and simulation are valuable tools for the design and analysis of metamaterial structures, the ultimate goal is validation through experiments, followed by application in an actual device. To that end, the fabrication of materials with engineered electrical properties began in the early 20th century, when metallic inclusions were arrayed within dielectric slabs for the purpose of creating high dielectric constant materials with relatively low densities. Though research on artificial media continued in subsequent decades, interest in metamaterials surged after the prediction and demonstration of negative refraction with arrays of wire and split ring resonators printed on circuit board substrates [26, 25, 27]. Initially operating only at microwave frequencies, it took less than a decade for structures to be fabricated that displayed metamaterial properties into the optical spectrum [28].

The rapid evolution of metamaterials from microwave to optical frequencies was due in part to the availability of robust manufacturing techniques previously developed for the electronics and microfabrication industries. Like other devices such as circuit boards or integrated chips that operate according to electromagnetic principles, the ordered placement of distinct materials is often required for metamaterials to function. In the case of a printed circuit or a micro-electromechanical device, specific patterns of conductors and insulators are needed to complete circuits and allow current flow. Metamaterials likewise require the ordered placement of materials to create the desired electric or magnetic response. By the time metamaterials were rediscovered at the start of the 21st century, semiconductor fabrication methods were already advanced and capable of 100 nm linewidths. This allowed metamaterial geometries resonant at GHz to be scaled with high precision to the small dimensions required for metamaterials to be active at much higher frequencies.

The fabrication of the many metamaterials that have been showcased in the literature often involves a combination of additive and subtractive processes. The choice of available processes for any particular design is dictated both by the frequency range of interest and dimensionality on the level of each individual metamaterial element and the entire device as a whole [11, 27, 29]. The following section contains a list of processes commonly used for the fabrication of 2D metamaterial structures. That is followed by a discussion of 3D

metamaterial fabrication.

2.2.1 Common Fabrication Processes for Metamaterial Structures

Many metamaterial structures are made with PCB or micro-fabrication techniques. Though process details and tools vary for these two manufacturing systems operating at different length scales, PCB and microfabrication methods are similar in their purpose, which is patterning surfaces with structures. Both begin with a substrate material, and use various additive and subtractive processes to alter the the substrate surface. For PCB processes, the substrate is often a polymer such as FR4, polyimide or PET. Microfabrication substrates are commonly silicon, silicon carbide or glass. Some of the processes used to modify those substrate surfaces are:

- Lamination: Used to add layers of copper or other materials through the application of pressure and heat, and often with the aid of adhesives.
- Silk Screen Printing: A process used in PCB production to apply an etch mask directly to a substrate surface through a patterned screen. Once the pattern is applied, substrates are placed in a chemical bath to etch exposed copper metal, leaving only the desired pattern.
- Micromilling: A subtractive process that removes material by cutting with a small milling machine at high spindle speeds. This mechanical process is used in PCB fabrication to form via holes within PCB substrates. It is also useful for other metamaterial designs that require holes. The smallest diameter holes available from commercially produced PCB boards are on the order of 0.1 mm, though end mills with smaller diameters do exist.
- Laser Ablation: A process that uses a laser to remove material. It can be used to pattern a surface or form via holes in films and substrates.
- Direct Write Technology: The use of a stylus to draw lines on a substrate with substances like metallic inks, which create conductive traces.

- **Electroplating:** A electrochemical process used to deposit metals on conductive surfaces. Plating is useful for the deposition of relatively thick layers of material, such as the filling of via holes in PCBs.
- **Sputtering:** A thin film deposition process where a target material is bombarded with high energy ions from a nearby plasma. The plasma particles collide with the target at very high speeds, knocking off small particles from the target material, which then deposit on a substrate below. This process takes place in a low pressure environment to ensure the mean free path of the sputtered particles is sufficiently long so they reach the substrate before reacting with other particles in the local atmosphere. The thickness of deposition is often limited by internal stresses within the sputtered material, which can overwhelm adhesive forces between the film and substrate.
- **Physical Vapor Deposition:** Another thin film deposition process in which a material is heated in a vacuum to the point where it begins to evaporate and particles precipitate on to the substrate surface. For metals, the heat can be generated resistively, while dielectrics often require bombardment with high energy electrons.
- **Photolithography:** A process in which a light sensitive polymer layer is used to pattern an underlying thin film. This process is commonly used for both PCB and microscale production, capable of linewidths ranging from many microns to nanometers, depending on the exposure system used. It usually involves several process steps:
 - **Spin coating:** A process in which liquid photopolymer droplets are placed onto a substrate that is rotating with high angular velocity. While centrifugal forces spread the droplets, a uniformly thin layer remains on the substrate surface due to contact forces.
 - **Development:** A process where a photopolymer is selectively exposed to radiation through a photomask, a transparent film with a darkened pattern printed on its surface. The mask is either placed directly above the surface to be patterned, or imaged through a lens system.
 - **Etching:** After the development process, excess resist is removed via a chemical

solution, leaving an etch resistant pattern atop the underlying thin film. The exposed thin film is removed in a similar fashion, with only the patterned area remaining.

- **Lift Off:** A process where thin films are deposited on substrates that are pre-patterned with a layer of sacrificial material. After the thin film deposition, which must be thin enough to leave some sacrificial material exposed, the sacrificial material is removed by etching, leaving only the thin film pattern on the substrate surface.
- **Electron Beam Lithography:** A process similar to photolithography where only high energy electrons are used to develop resist masks, as opposed to UV or other electromagnetic radiation. The small wavelength of the electrons provides this lithography process resolution on the order of 10 nm, which is useful for the fabrication of metamaterials structures active at THz frequencies.
- **Interference Lithography:** Another process similar to photolithography where the pattern that results on the substrate is an interference pattern created by the diffraction of light through a grating, as opposed to a pattern printed onto a photomask. This process is able to produce periodic patterns with very high resolution.
- **Nanoimprint Lithography:** A patterning process in which a mold is used to mechanically deform a resist or thin film. As a mechanical process, smaller features are possible relative to optical systems which are limited by diffraction.
- **Focused Ion Beam Milling (FIB):** A subtractive process which uses a focused beam of high energy ions to remove material from a substrate surface. The ions bombard the film clad surface, causing the ejection of film or substrate particles. This method is used to pattern films with nanometer resolution, and has a shorter cycle time than other electron beam lithography processes.
- **Shadow Masking:** A process that allows for the direct deposition of patterned thin films by masking the substrate with a monolithic stencil. As an alternative to photolithography, it removes the many process steps involved with chemical etching, but is unable to produce the same quality line widths.

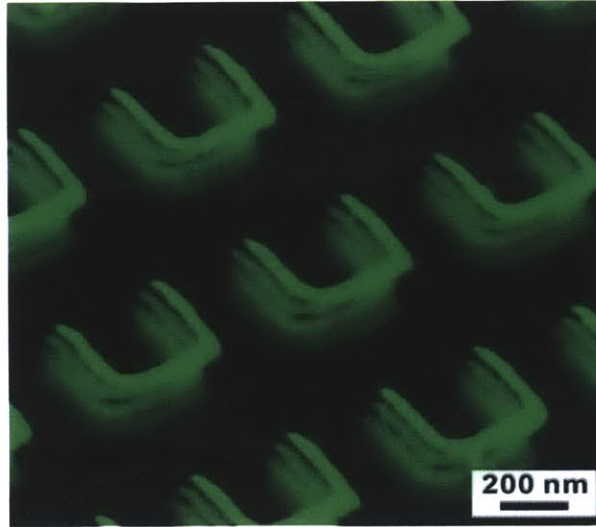


Figure 2-5: A multi-layer stack of split ring resonators, fabricated using electron beam lithography, anisotropic etching and planarization steps [30].

2.2.2 Multilayer and Non-Planar Metamaterial Fabrication

The fabrication of 3D metamaterial structures can be significantly more complicated than 2D structures. Construction of a 2D pattern is simplified by the fact that any point within a 2D plane is always accessible via the remaining spatial dimension. This is not the case for 3D metamaterials, which often consist of stacked 2D layers. Such stacks have been fabricated utilizing processes that incorporate multi-layer PCBs, chemical-mechanical planarization, liftoff and deep anisotropic etching.

The multi-layered fabrication of planar structures is limited because it can be difficult to produce metamaterials sensitive to incident fields polarized along multiple directions. For example, the stack of split rings in Fig. 2-5 only has a magnetic response for radiation incident from within the plane of the image with its magnetic field polarization parallel to the loop normal. The split ring arrangement in Fig. 2-6, which has an isotropic magnetic response, would be very difficult to fabricate using multilayer methods. To achieve the multi directional response, individual layers of planar structures have to be manually assembled and weaved together or manually assembled into the proper arrangement.

Another consideration that affects the viability of multilayer metamaterials is dissipation loss. Many metamaterials have significant losses with only a single layer of material, as

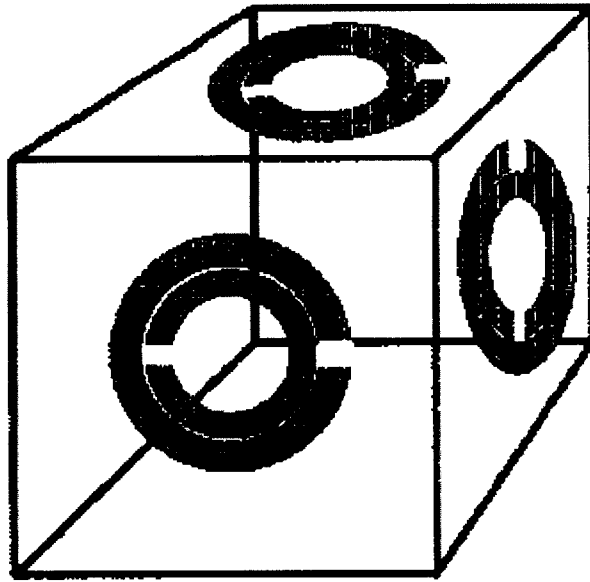


Figure 2-6: A cubic unit cell with split ring oriented in three different directions to create an isotropic response [25].

incident electromagnetic waves propagate through lossy dielectrics and induced currents traverse along the surface of imperfect electric conductors. The inclusion of additional layers compounds the problem, further reducing metamaterial efficiency.

2.3 Additive Manufacturing for Complex 3D metamaterials

In this thesis, I consider additive manufacturing as an alternative method to produce 3D metamaterials. Additive manufacturing techniques have been developed over the last quarter century to enable the rapid prototyping of mechanical components and tooling. Before additive manufacturing, the fabrication of prototypes often involved a significant investment involving multiple tools and machines and extended waiting periods. Today, rapid prototyping techniques can build a newly designed mechanical structure in a matter of hours.

All additive manufacturing processes build parts in layers. While similar to the strategy outlined above for the fabrication of multilayer metamaterial devices, the materials and

techniques used for additive manufacturing are carefully selected for their ability to form monolithic, self-supporting structures.

2.3.1 List of Additive Processes

Some of the more commonly used additive processes for rapid prototyping include [31]:

- Stereolithography (STL): A process in which a vat of photocurable liquid polymer is selectively cured by a UV laser source. The laser is focused on select points in the x-y plane, photopolymerizing the material at those locations. The first hardened layer of the part, which rests on movable platform, is then lowered into the vat to allow the next layer to be added on top. If previous cured material is unable to support subsequent layers, perforated support structures can be formed from the liquid polymer, and removed in a finishing step.
- Fused Deposition Modeling (FDM): A process where parts are produced from stacked layers of thin extruded plastic rods. As each layer of heated plastic is extruded, it partially melts the plastic below, allowing the two layers to bond upon cooling. A support material separate from the model material can also be extruded when required, which is removed upon part completion.
- Selective Laser Sintering (SLS): A process by which a powder is selectively sintered to form an single object. Similar to STL, a laser is used to sinter specified regions in a layer of powder. After each layer is solidified in the desired locations, a new layer of powder is flattened over the previous layers. Unsintered powder is used as the support material. This process is capable producing ceramic, metallic and polymer parts.
- Three-Dimensional Printing (3DP): A process similar to SLS which instead uses adhesive binders to form parts from layers of powder. After being printed, the green parts can be sintered to fuse the powder.

The precision of most of the process in the above list range from .015 GHz to 1 GHz. Similar processes have been developed for micro and nano structures, such as Micro-Stereolithography and Two-Photon Polymerization.

2.3.2 Process Capabilities and Limitations

Additive manufacturing is a geometrically flexible process capable of producing shapes, surfaces and assemblies that are difficult to produce with conventional automated fabrication equipment. The price for that flexibility comes at the expense of the price per part, but also limited material selection, dimensional accuracy and weakened structural properties. In situations where the tolerances are not overly strict such as parts meant for display purposes, these limitations may not be significant. These capabilities and limitations are most relevant when these processes are used to fabricate functional devices. The following will enumerate how the capabilities and limitations of additive manufacturing relate the requirements for electromagnetic and metamaterial devices:

- Geometric flexibility afforded by additive manufacturing is a capability that could be of great value to electromagnetic designs. As discussed in Section 1.1.1, all parts of an electromagnetic system are influenced by geometry. The availability of additive manufacturing for electromagnetics results in a widening of the geometric design space.
- Material availability in additive manufacturing has significant implications for the function of electromagnetic devices that can be fabricated. While processes are capable of building parts from either dielectrics or metals, most cannot incorporate these complementary materials into a single construct due to the incompatible process requirements. This is especially relevant for the fabrication of metamaterials, which may require the strategic placement of both conductors and dielectrics. Many processes do support parts built from two different but materials, which can be useful for the introduction of electrical property gradients.
- Dimensional accuracy of structures is relevant for designs with critical dimensions, such as narrow band resonant structures, and other frequency dependent geometries.
- Weakened material properties are relevant for electromagnetic design, both from the standpoint of limits resulting from structural instability, and how those may be related to adverse affects on electrical properties, such as the reduced conductivity of selectively sintered metal parts relative to parts machined from a bulk slab of conductive material.

2.3.3 Additively Manufactured Metamaterials

Despite the limitations, there remains a large window of opportunity for the application of additive manufacturing to electromagnetic design. The following are three examples of metamaterials fabricated additively:

- Gradient Refractive Index Lens: Sachs and Wang employed slurry based 3DP for the fabrication of gradient index lenses [32]. The printed lenses were built from aluminum nitrate or barium acetate doped silicon dioxide powder. The concentration of the dopant was varied at each point to give the lens its refractive index profile. After printing, the lens went through a heat treatment and sintering procedure, fusing the powder together and transforming the dopant into an oxide. Many aspects of the fabrication process were difficult to control, such as the migration of dopant during sintering which distorted the intended gradient index profile, highlighting the considerations that must be taken to properly incorporate multiple materials in 3D printing or similar additive processes.
- Luneberg Antenna: Liang [33] used a layered photo-polymerization process to fabricate a 3D X-band Luneburg lens antenna, a gradient index structure designed to focus radiation on its outer surface. Instead of using a material dopant to define a gradient index, voids of various sizes were arranged within the printed volume. These voids effectively created a mixture of polymer and free space, the refractive index of which was proportional to the volume of polymer versus free space in any given voxel.
- 3D Split Ring Array: One example can be found in the literature that mentions rapid prototyping of metamaterial blocks including both metallic and dielectric materials. Though few details are given, Mercure [34] discusses the fabrication of a Negative Index material that incorporates both a cubic intersecting grid of metallic wires and an array of metallic helical inclusions. As the helical inclusions are not electrically connected to one another, a dielectric support material is incorporated as a background material.

2.3.4 Surface Modification of Additively Manufactured Structures

While the final example of the previous subsection discusses the fabrication of arrayed metallic elements supported within a dielectric matrix, in today's additive manufacturing market one would be hardpressed find a commercially available machine capable of producing parts that contain both metals and dielectrics. Until that option becomes more widely available, post-process surface modification represents a viable means for overcoming some of the material limitations associated with additive manufacturing. An example of this is presented by Rudolph [18, 35] in the fabrication of an isotropic 3D NRI metamaterial. Each metamaterial unit cell consisted of a 3D cubic frame fabricated via STL. The surface of the polymer frame was then partially metalized with an electroless plating process, after which 12 surface mount capacitors were soldered at the middle of each leg.

2.3.5 Usage of Additive Manufacturing in this Thesis

Additive manufacturing and surface modification techniques were utilized in this thesis for the fabrication of 3D metamaterials and conformal electromagnetic structures:

- In Chapter 3, both a base material for metamaterial unit cells and a scaffold to aid in cell arrangement were produced using FDM and layered photo-polymerization. Surface modification included the addition of copper and polyamide tape for the fabrication of an Artificial Magnetic Conductor substrate.
- In Chapter 4, hundreds of interconnected 3D S-ring structures were fabricated using layered photo-polymerization. The surface was modified with the addition of a metallic layer through a PVD and sputtering processes.
- In Chapter 5, the surfaces of non-planar structures fabricated with layered photo-polymerization were selectively coated with the aid of shadow masks also fabricated with layered photo-polymerization, in a process I have called Conformal Masking.

2.4 Chapter Conclusions

In this chapter, I reviewed the basic electromagnetics of metamaterials and common methods of fabrication. Through the derivation of the split ring resonator's effective permeability, I showed how the introduction of metallic inclusions can be used to change a material's properties. The analysis also provides a clear connection between the geometry of the inclusion, and the frequency dependent nature of the inclusion's effect. While theoretical analysis is not always possible, extraction of parameters via simulation is another viable route, allowing for the study of complicated structural designs.

Though the virtual design space for metamaterials is bounded only by computational resources and Maxwell's Equations, the fabrication space is much more limited. Limitation exists because metamaterials require the ordered mixing of two or more bulk materials, and these materials must be compatible, in that they can be processed side by side in a controllable way. This fabrication challenge is hard, but its one that has been met before by the PCB and microfabrication industries, utilizing the processes listed in this chapter to fabricate metamaterial prototypes.

I also introduced additive manufacturing techniques, which have recently been used in the fabrication of electromagnetic devices, and will be utilized for the fabrication of devices in the coming chapters.

Chapter 3

Artificial Reflection in Depth

In this chapter, I show the design and fabrication of a 3D metamaterial for use as an Artificial Magnetic Conductor (AMC). AMCs are metamaterials designed to affect the reflection of electromagnetic waves by altering a surface's boundary condition. While they have been used for various applications and designed for various frequency bands, I approach the AMC as a solution to the problem of placing RFID tags on metal surfaces, an issue which has plagued the RFID industry for many years [36]. I begin this chapter with a discussion of UHF RFID technology, and the basic physical principles by which it operates. That is followed by the issues that prevent RFID tags from functioning properly while near metal objects, and some of the solutions that have been proposed. One solution that has been offered is through the use of AMCs. After a brief review of related work, I introduce the 3D AMC metamaterial design, as well as fabrication and testing.

3.1 RFID Background

UHF RFID is a system used to wirelessly identify objects. Operating in frequency bands just below 1 GHz, RFID provides cost saving benefits for various applications, the primary being inventory management in warehouses, retail stores and throughout the global supply chain. In its simplest form, an RFID system consists of two distinct components, (1) a Reader and (2) a Tag (Fig. 3-1). For the discussion in this thesis, the reader unit includes signal generating and processing circuitry and an antenna with which it transmits and receives

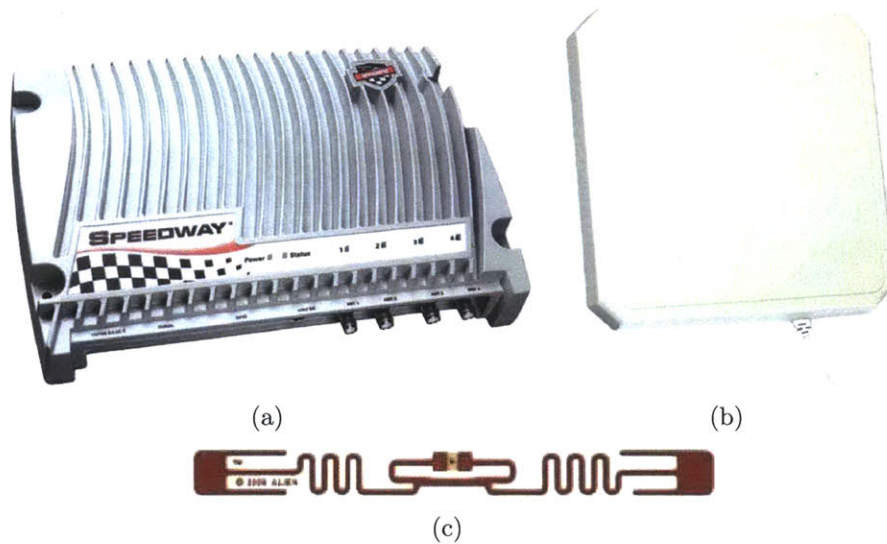


Figure 3-1: (a) An RFID reader with its (b) antenna and (c) a typical UHF RFID tag.

electromagnetic signals to and from multiple RFID tags. An RFID tag consists of an antenna and integrated circuit(IC) chip. The tag antenna serves as both a power harvester and transceiver, while the IC chip is encoded with a unique ID number and the logic required for the tag to respond to queries from an RFID reader. Designed with an eye towards worldwide adoption of UHF RFID systems, passive RFID tags are expected to operate according to global standards and be low cost devices. To that end, the IC chips themselves are relatively simple, capable of performing only a limited number of functions. No battery is included, making tags reliant on the reader as their source of power. Tag antennas are expected to conform to a small footprint, allowing them to be incorporated on to items without causing a disruption.

3.1.1 RFID Physics

UHF RFID systems typically operate by the reader first transmitting a sinusoidal signal into the area around its antenna. Tags in close proximity to the reader harvest some of the transmitted power to allow the tag chip to function. At that point, electromagnetic signals are sent from the reader to the tag and vice versa, with the tag responding to requests from the reader via modulated backscatter.

Leaving the signal processing aside, the governing physics of an RFID system is contained

within the Friis Transmission equation [37],

$$P_r = P_t G_r G_t \left(\frac{\lambda}{4\pi r}\right)^2 \quad (3.1)$$

where P_t is the power transmitted at a particular wavelength λ from one antenna with a gain of G_t . P_r is the power received by a second antenna which has a gain of G_r . It is assumed that both antennas are operating in free space separated by a distance r . While technically this equation must be applied to both the forward link (power sent from the reader to the tag), and the reverse link (power sent back from the tag to the reader), most RFID systems are forward link limited due to the sophistication and sensitivity of modern RFID reader equipment. Consequently, application of the Eq. 3.1 is most useful when applied to the calculation of the tag read-range [38], where

$$r = \frac{\lambda}{4\pi} \sqrt{\frac{P_R G_R G_t \tau}{P_t}} \quad (3.2)$$

with r being the maximum distance at which an RFID tag receives enough power to be read by a reader. This depends greatly on antenna factors such as gain as well as τ , which corresponds to the impedance match between the tag antenna and its IC chip, or how efficiently power received by a tag antenna is delivered to the tag chip. Despite playing a crucial role in the operation of the tag, tag antennas tend to be relatively simple constructs. The dominant antenna design for free space UHF RFID tags is a planar dipole, featuring omni-directional gain in the radiation field perpendicular to the dipole axis, and requiring only slight structural modifications to enable an impedance match with the IC chip. The situation can become more complicated when one considers the material of the object on which the tag is placed, as the radiation pattern can be adversely affected by the tag's environmental surroundings and the task of properly matching the antenna to the chip becomes more difficult. The most complicated such case that utterly cripples UHF RFID tags happens when they are placed on metal objects [39].

3.2 The RFID Metal Problem

When standard RFID tags are placed directly on or near metal objects, their ability to operate is affected significantly by currents induced within the conductive material. In an attempt to satisfy the electromagnetic boundary conditions, which require the electric field tangential to a highly conductive material to be zero at the surface, the free charges within the metal rearrange to cancel out any incident electric fields (Fig. 3-2). This means that in close proximity to a metal surface there is little electric field for a dipole RFID tag antenna to harvest (Fig. 3-3). Even if there was enough electric field, any currents flowing through the antenna and the fields they produce induce mirror image currents in the ground plane 180° out of phase with the actual currents [4]. Equivalently, any electromagnetic waves emitted by the tag antenna incident on the conductive surface reflect with a reflection coefficient $\Gamma = -1$. The fields radiated by the images, or reflected waves, cancel a large portion of any backscattered signals. These effects manifest as a severe drop in the antenna radiation efficiency (Fig. 3-4) and causes an impedance change that makes it difficult to match the antenna with the IC impedance, leaving the tag powerless to function (Fig. 3-5) [36]. In other words, an RFID tag on a metal surface is a dud.

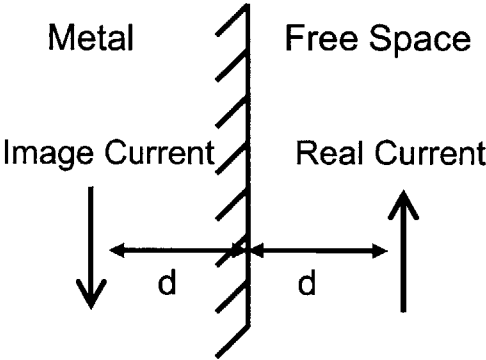


Figure 3-2: The image of currents parallel to the metal boundary appear with a 180° phase shift.

3.2.1 Possible Solutions to the Metal Problem

With millions of metal products in the supply chain that have potential to be tracked with RFID, many solutions have been proposed to solve the problem of placing UHF RFID tags

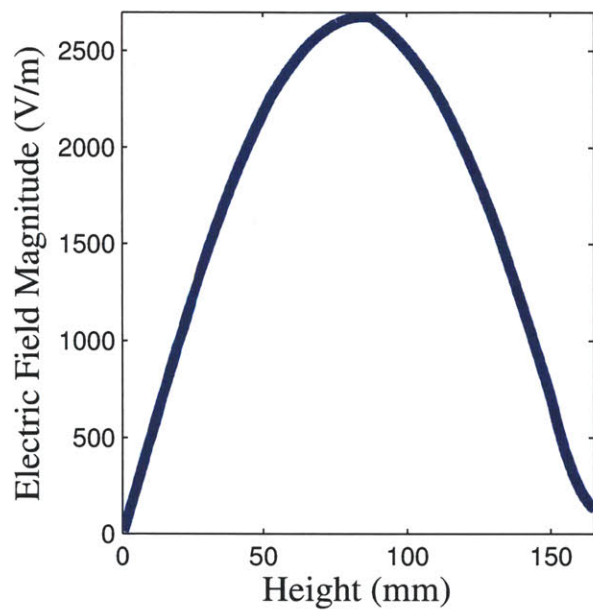


Figure 3-3: Simulated electric field magnitude for a plane wave incident on a metal surface.

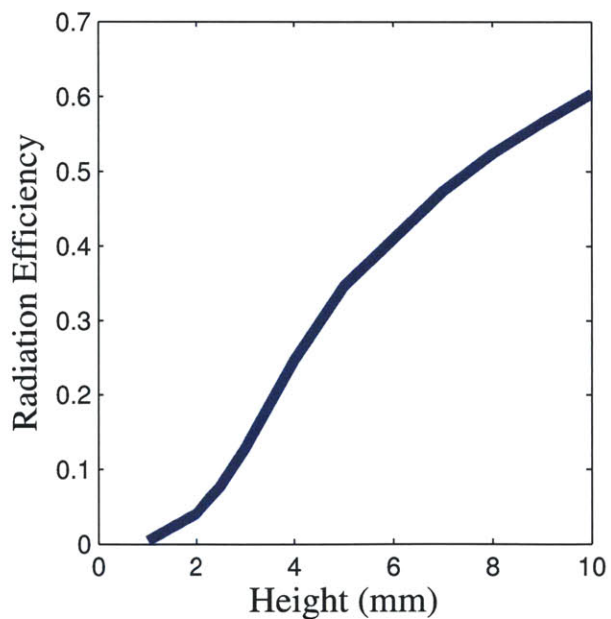


Figure 3-4: Simulated radiation efficiency for an *Alien*© squiggle antenna at various heights above a conductive ground plane.

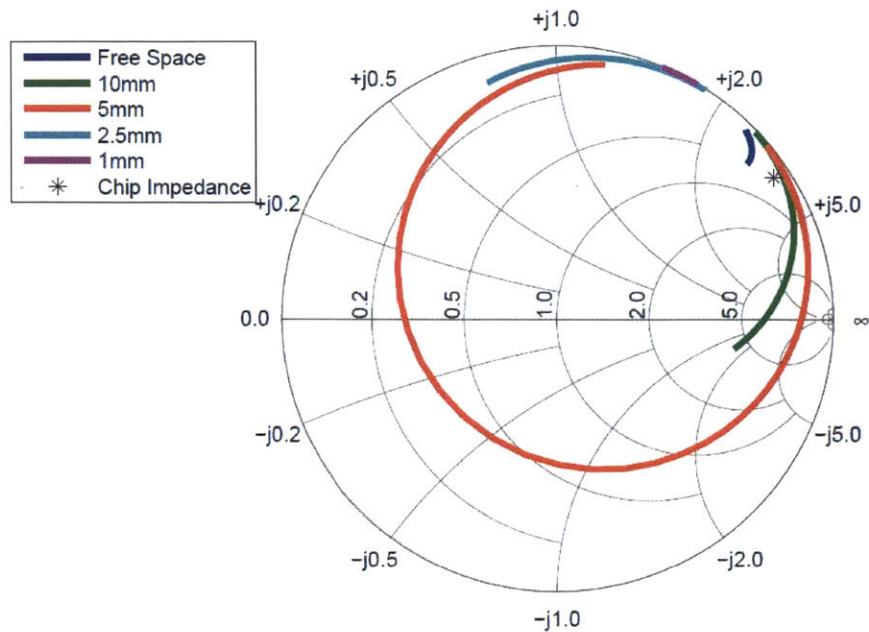


Figure 3-5: Simulated antenna impedance for an *Alien*© squiggle antenna at various heights above a conductive ground plane.

on metal, the advantages and disadvantages of which are discussed below:

- The simplest way to reduce the detrimental effects of metal on the tag is to place a spacer between the tag and the metal surface. While impedance improvements come quickly as the radiation resistance increases, both the available electric field and the tag's broadside radiation pattern reach a maximum only at a distance of $\lambda/4$. At this distance, the electromagnetic waves that reflect off of the metal are in phase, generating high field levels for power harvesting and increasing the tag's radiated power [40]. Unfortunately, $\lambda/4$ is approximately 8 cm for UHF RFID frequencies, which is an excessive spacer thickness for most RFID applications. Thinner spacers, often made from higher dielectric constant materials, do succeed in allowing RFID tags to operate with suboptimal performance, but at distances below 5 mm impedance matching becomes a nontrivial task, severely limiting antenna read range and bandwidth [41].
- Insertion of a thin lossy material layer between the antenna and the conducting surface effectively hides the metal from the tag. The lossy material electrically shields the tag from the metal by attenuating any fields that would induce image currents, thereby

stifling any possible interference with the tag antenna radiation [42]. While these lossy spacers can be thin and functional in practice, they lack the constructive interference advantages of thicker quarter-wave spacers.

- Other solutions involve abandoning the standard dipole tag antenna for different antennas types that can be optimized for near metal performance, such as patch antennas or inverted F antennas. While these have been successful commercially, they remain significantly thicker and more expensive than the standard free space RFID tags [43, 44].

3.2.2 The Ideal Solution

Another solution that could help dipole antennas function on metallic items is to change the surface boundary condition. As mentioned above, the metal surface boundary condition plays a large role in preventing any nearby dipole antenna from radiating properly. According to the electromagnetic boundary conditions required by Maxwell's equations, $\vec{n} \times (\vec{E}_1 - \vec{E}_2) = 0$ [4], the components of the electric field that are tangential to a surface boundary must be continuous. In the case of a perfect electric conductor, which most metals resemble at microwave frequencies, the electric field inside the conductor is always zero. This causes the electric field on the surface of the metal to equal zero as well, which is practically achieved by the movement of free electrons, or image currents, on the metals surface.

One way to improve the situation would be to place a layer of perfect magnetic conductor (PMC) between the antenna and the metal surface. As the magnetic analog of a perfect electric conductor, a PMC is an idealized material with an infinitely high permeability, inside which the magnetic field is always zero. The boundary conditions require all tangential magnetic fields to have a magnitude of zero. Several consequences of this condition are beneficial for low-lying dipole RFID antennas. Firstly, the PMC boundary condition allows for non-zero tangential electric fields, improving the environment for dipole antenna power harvesting. Second, the reflection coefficient for the electromagnetic waves incident upon the perfect magnetic surface changes to $\Gamma = +1$, equivalent to a phase shift of 0 at the boundary, as opposed to a reflection coefficient of $\Gamma = -1$ or a phase shift of 180° for its electrically conducting counterpart (Fig. 3-2). The altered boundary condition leads to

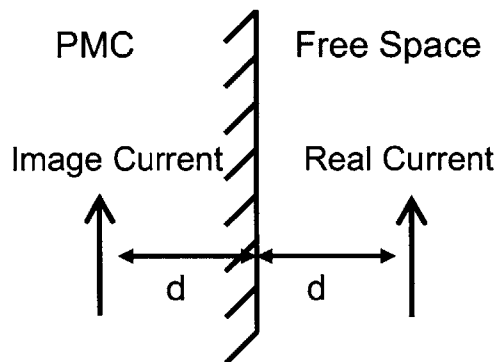


Figure 3-6: The image of currents parallel to the PMC boundary appear without a phase shift.

in-phase reflections and constructive interference for radiated antenna signals. A similar consequence arises when image theory is applied to currents on one side of a perfectly magnetic boundary. While the current's image still appears on the opposite side of the boundary, it's oriented in the same direction, with the same phase. Antennas close to perfect magnetic boundaries can take advantage of these reflection anomalies and in-phase current images to boost performance without having to resort to other, thicker solutions [4]. Unfortunately, as with any idealized material, perfect magnetic conductors with infinite permeability over the entire frequency spectrum are not found in nature. At frequencies below 100 MHz, various forms of ferrite material do possess extremely high permeability, but while these produce magnetic conductor like effects and are beneficial for antennas at the relevant frequencies, their magnetic properties do not extend up to frequencies near the band of UHF RFID.

3.3 The AMC solution

While perfect magnetic conductors don't exist in nature, various metamaterials consisting of periodic surface formations known as artificial magnetic conductors (AMC) have been designed to recreate PMC properties at microwave frequencies. This research topic is nearly a decade old [11]. While not infinitely thin, for the price of a finite thickness AMCs introduce reactive elements which can alter a conductive surface's electrical properties. The reactive elements are realized by covering the metallic surface with arrays of subwavelength structures (Fig. 3-7). These structures, which can be abstracted to have capacitive and inductive com-

ponents (Fig. 3-8), generate a resonance at particular frequencies which affect the phase of reflected electromagnetic waves. When viewing the system as a transmission line (Fig. 3-9), the reactive surface elements which terminate the transmission line are subsumed within a quantity known as the surface impedance Z_s , instead of an otherwise short-circuited conductive boundary. When resonance occurs at $\omega_0 = 1/\sqrt{LC}$, the effective impedance of the surface

$$Z_s = \frac{j\omega L}{1 - \omega^2 LC} \quad (3.3)$$

approaches infinity, resulting in a reflection coefficient Γ

$$\Gamma = \frac{Z_s - Z_0}{Z_s + Z_0} \quad (3.4)$$

that approaches +1 in the limit of $\omega \rightarrow \omega_0$.

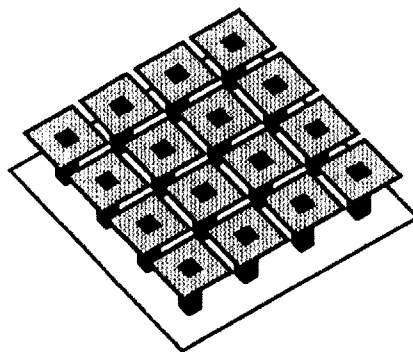


Figure 3-7: Commonly used structure for AMC surfaces [11].

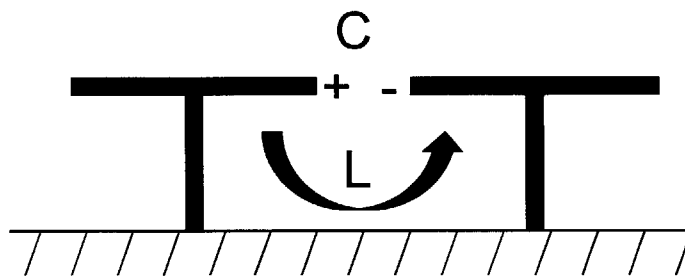


Figure 3-8: Suggested inductance and impedance abstraction for structure in Figure 3-7 [11].

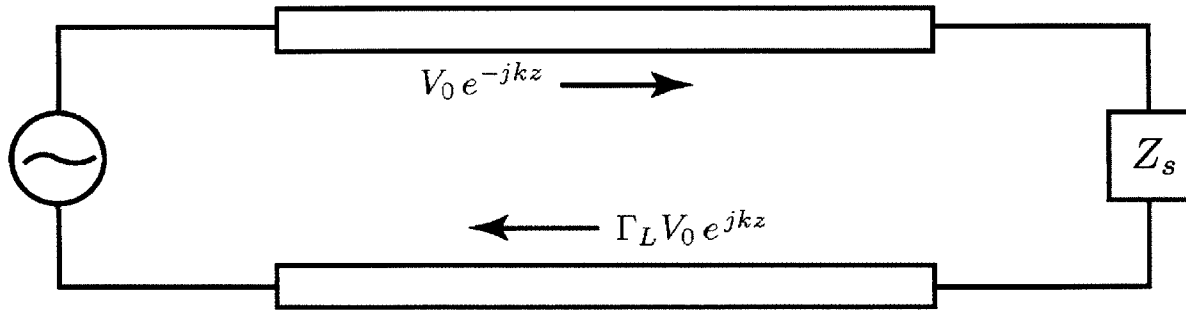


Figure 3-9: Transmission line abstraction for modeling AMC surface impedance [11].

3.3.1 AMC for UHF RFID

A successful AMC substrate for RFID should aim to satisfy several design requirements:

- The resonance frequency must coincide with the RFID band of operation. For the case of UHF RFID in North America this band is between 902 – 928 GHz.
- The substrate thickness should be minimized. Commercially available on-metal RFID tags based on lossy materials or more complex antennas have thicknesses between 1 – 10 mm.
- The bandwidth of the AMC reflection coefficient should be maximized to ensure the beneficial characteristics of the substrate are applicable for all operating frequencies. At least some constructive interference is assured when the phase of the reflected wave is between $\pm 90^\circ$.
- The unit cell footprint should be minimized to create a better bulk material approximation as seen by the antenna, and allow for the miniaturization of the overall tag area.
- Loss within the AMC should be minimized, so the constructively interfering reflected wave increases signal strength.
- Material and fabrication costs should be minimized.

3.3.2 Related Work

Many AMCs designed to benefit antenna systems have appeared in the literature. The first and most frequently referenced AMC unit cell design is known as the Sievenpiper mushroom [11], which consists of a conductive ground plane connected to an array of metallic patches by conductive vias 3-7. Based on a transmission line model for the surface impedance, Sievenpiper designed this structure to introduce capacitance between the mushroom caps and inductance from the conductive loop. Together, the reactive components resonate to generate a reflection coefficient of +1, as well as block the propagation of electric current along the metallic surface, which is also beneficial in certain antenna configurations. While the initial study featured the mushroom AMC built from plated PCB board operated at 15 GHz, Sievenpiper showed how the resonant frequency could be tuned by changing the geometry, with a decrease in thickness increasing the resonant frequency, and an increase in patch size resulting in a lower resonant frequency.

Though patch size and height could be balanced to shift the resonance frequency up or down arbitrarily, as the overall substrate thickness decreases, patch sizes increase significantly to make up for the lost inductance. To limit the patch size in such situations, Sievenpiper also introduced a multi-layered mushroom surface, where extra layers capacitively load the structure [45, 46]. While various forms of capacitive loading are successful at increasing the capacitance without extremely large patches, the price is paid in bandwidth, which varies inversely with capacitance.

Due to the relatively high costs of fabricating vias, various other AMCs have been designed consisting of arrayed metallic patches without vias, electrically isolated and spaced above a ground plane by a dielectric layer. Like the mushroom structures, these purely planar designs also exhibit the characteristic AMC reflection coefficient and are capable of improving antenna performance. While these planar designs lack surface wave suppression which requires the vias to be present, planarity makes them much simpler to fabricate. Low frequencies variations of this design have been explored through multilayer patch configurations and other array designs meant to reach low frequencies through capacitive loading, such as meander lines that maximize patch capacitance, or increasing the dielectric constant

Reference	ϵ	Thickness	Length	$\frac{\Delta\omega}{\omega_0}$	$\omega_0(GHz)$
Sievenpiper [11]	4	$\lambda_0/40$	$\lambda_0/20$.083	2.4
DJKern [48, 49]	36	$\lambda_0/69$	$\lambda_0/14$.05	.860
DeCos [54]	25	$\lambda_0/140$	$\lambda_0/28$.04	.868
Gao [50]	2.6	$\lambda_0/881$	$\lambda_0/26$.006	.810
Gao [51]	2.6	$\lambda_0/111$	$\lambda_0/12$.005	.918
Gao [53]	4.4	$\lambda_0/180$	$\lambda_0/18$.021	.930
Konishi [55]	3.5	$\lambda_0/388$	$\lambda_0/12$.02	.966
This Work	3.2	$\lambda_0/53$	$\lambda_0/26$.058	1.13

Table 3.1: Summary of unit cell parameters from the literature.

of the layer interposed between the patches and the ground plane [47, 48, 49].

Several published works report on the use of AMC substrates, both with and without vias, applied to the problem of placing UHF RFID tags on metal surfaces [50, 51, 52, 53]. To varying degrees of success, they have adapted the Sievenpiper mushroom to operate below 1 GHz, and enable the RFID tag to function (Table 3.1).

3.3.3 New Unit Cell Design

To further explore the space of possible AMC designs, I introduce a new unit cell geometry with the aim of further reducing the overall footprint of the individual unit cells and thickness of the AMC substrate. The chosen geometry is based on Pendry’s split ring resonator [25]. Originally designed for its post-resonance negative effective permeability band, reshaped and exploited for a whole host of applications including cloaking [19] and negative refraction [27], a split ring’s pre-resonance band features a spike in effective permeability, making it an obvious candidate for the cellular element of an artificial magnetic material. Incorporated into a unit cell design, a split ring near resonance would be expected to enhance the lumped surface inductance.

Several factors must be considered when reconfiguring a split ring resonator for use in a low profile UHF AMC. As mentioned above, the first priority is the ability to reach low enough frequencies within the area provided. Though inductance is inherent to any ring structure, capacitance is deliberately added by introducing a split in the ring, with value of the capacitance set by the gap width and surface area. In order to generate capacitance high enough to reach the low frequency resonance needed for UHF RFID, large conductive surface

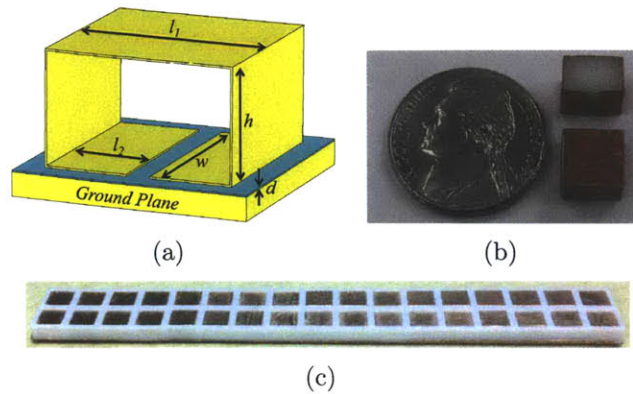


Figure 3-10: (a) Model of the new unit cell derived from a split ring resonator [9], and (b) image of two individual unit cells which were later placed in the (c) scaffold.

areas with small gap widths are required. A second factor is the ring's anisotropy vis-a-vis the polarization of any incoming plane wave, which necessitates the vector normal to the ring's loop be perpendicular to the incoming wave's direction of propagation and properly aligned with the wave's magnetic field vector. Finally, another consequence of the requirement to minimize AMC thickness is that it imposes a restriction on one contributing dimension to the total loop area and suggests the use of a rectangular loop structure [56, 57, 9]. This combination of factors led to the proposal of the three dimensional metamaterial unit cell in Fig. 3-10(a). Though only half the profile of previous split ring resonator iterations, moderately enlarged dimensions and extrusion in the direction normal to the loop provide large capacitive areas when placed in close proximity to a conductive ground plane.

3.3.4 Initial Prototype Fabrication and Characterization

Both simulations and experiments were conducted to confirm that the proposed unit cell exhibits the expected AMC reflection behavior. The initially constructed AMC prototype cells had dimensions $l_1 = 8 \text{ mm}$, $l_2 = 3.5 \text{ mm}$, $w = 8 \text{ mm}$, $h = 4.9 \text{ mm}$, $d = 63.5 \mu\text{m}$ and consisted of 3D printed blocks of polymeric material with a permittivity of $\epsilon = 2$ wrapped in a split ring of copper tape which was precisely cut using a Roland CX-12 plotter. Individual units were placed in a scaffold made from the same material, and then placed over a copper tape ground plane covered with a thin polyamide layer of $\epsilon = 3.2$ (Fig. 3-10).

Simulations to characterize the unit cell reflection coefficient were performed using HFSS,

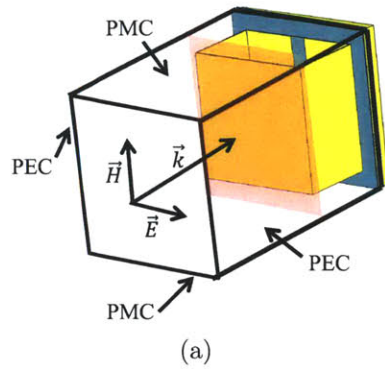


Figure 3-11: The simulation TEM cell, with magnetic boundaries normal to the y-axis, electric boundaries normal to the x-axis, and port reference plane just above the structure.

with one unit cell placed in a TEM cell and exposed to an incident plane wave polarized with the magnetic field vector oriented normal to the structure's loop (Fig 3-11). Taking advantage of symmetries in the periodic array, only a single element needed to be simulated to simulate the surface response. The reference plane for the phase of the incident and reflected waves was just above the 5mm height of the unit cell. The simulation results were indicative of AMC behavior as the phase of the reflected wave passes through zero at

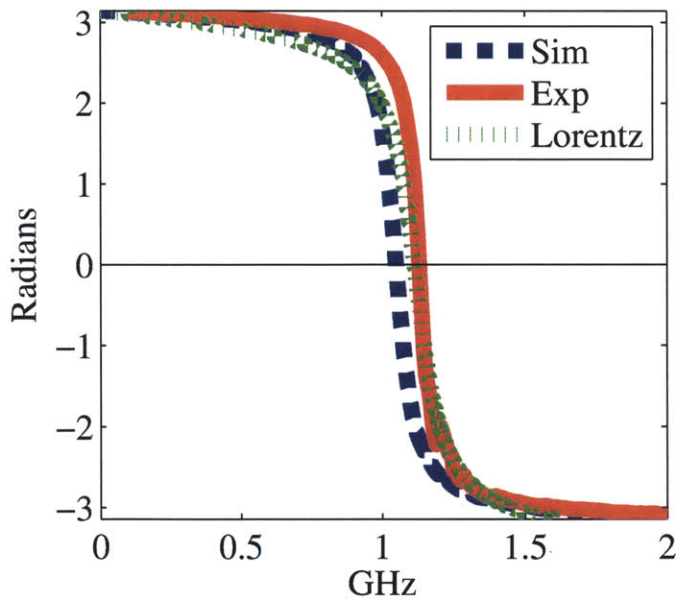


Figure 3-12: Phase of the reflected wave above the surface of the AMC. The Lorentzian material's response is similar to those of the simulated and experimental AMC unit cell.

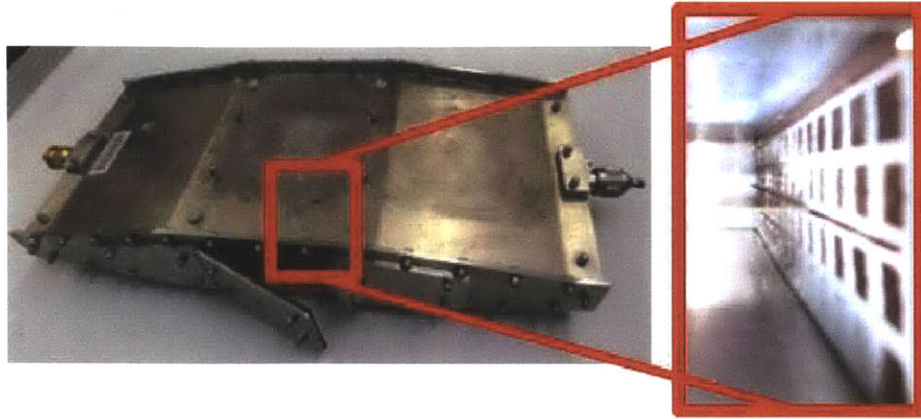


Figure 3-13: AMC arrays loaded in the TEM-F3000 chamber for phase measurements.

1.048 GHz (Fig. 3-12), with an in-phase bandwidth of almost 400 MHz.

For the experimental evaluation, two arrays of 17×2 split ring unit cells were placed inside a F3000-TEM chamber [58] and exposed to an incident wave of the same orientation as in the simulation (Fig. 3.3.4). The procedure of the experiment was as follows.

- The TEM chamber was connected to an HP 8510B Network Analyzer to both generate the incident wave and record the phase of reflected waves.
- As a reference, a metal plate with a known reflection coefficient of $\Gamma = -1$ was placed inside the TEM chamber, and the phase of the reflected wave was recorded.
- The metal plate was subsequently removed and the AMC sample was fitted inside the TEM chamber such that its surface was in the same location as the reference plate. The phase of the wave reflecting off the sample surface was also recorded

By combining the data from both measurements, the phase of the difference between the two signals was shifted by π and plotted in Fig. 3-12. In the regions on the far left or right, the phase is $\pm\pi$, which is the phase change one would expect when encountering a metallic plate. However, in the middle region around 1.13 GHz the phase of the reflected wave crosses through zero, which means there is a reflection coefficient of $\Gamma = +1$ at that frequency.

3.3.5 Antenna Simulations

In order to understand the performance of a planar antenna in close proximity to the AMC, we performed simulations in which a dipole antenna modeled as a 50Ω S-parameter discrete port with variable arm length was placed above a 5 mm layer of dielectric with a Lorentzian magnetic response. The Lorentzian parameters were tuned so the reflection phase response would be similar to the phase response of the AMC unit cell (Fig. 3-12). The homogeneous AMC equivalent is required as a simulation of a full split ring unit cell array would need extensive computational resources. For comparison purposes, the same antenna simulations were performed but with 5 mm of air, which is referred to as the spacer scenario. When com-

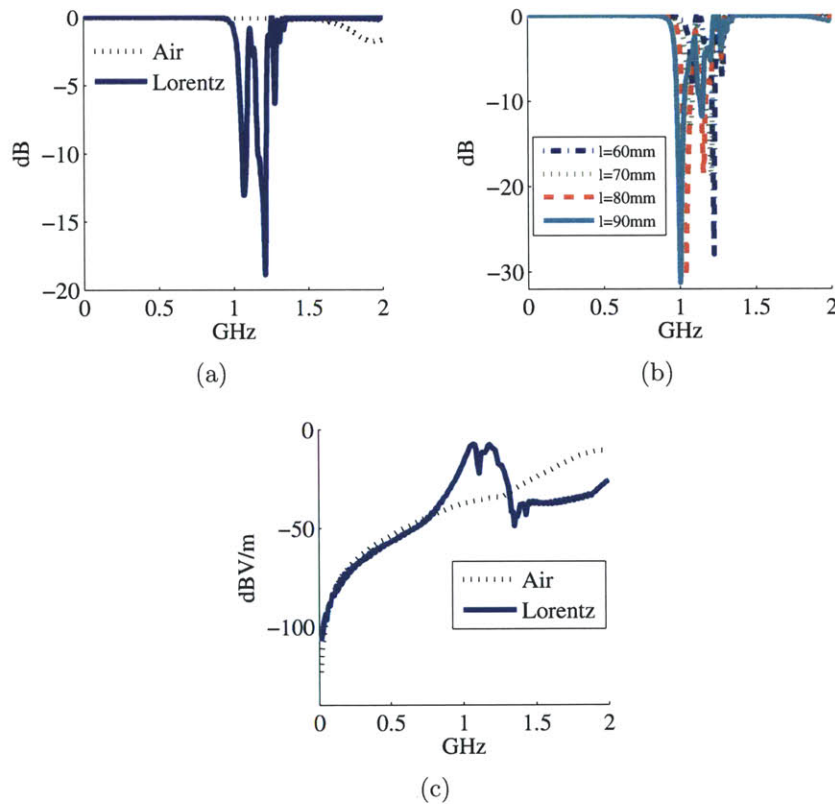


Figure 3-14: (a) S_{11} and (c) power density at 1m for the 80mm dipole, and (b) S_{11} for antennae of various lengths atop the magnetic material substrate.

paring the Lorentzian and spacer scenario results, two details stand out. First, around the Lorentz resonance frequency the antenna displays a reduced return loss signature compared with the spacer (Fig. 3-14(a)), which was expected as evidenced by previous AMC studies

([11, 59, 60]). This return loss effect remained even as the antenna length varied significantly (Fig. 3-14(b)). Second, in that same resonance band the Lorentzian case results in a higher maximum radiated power density than the spacer scenario (Fig. 3-14(c)). Taken as a bulk representation of AMC behavior, the Lorentz material both matches results of previous AMC substrate simulations and predicts significant improvements for antenna power transmission.

3.3.6 Antenna Experiments

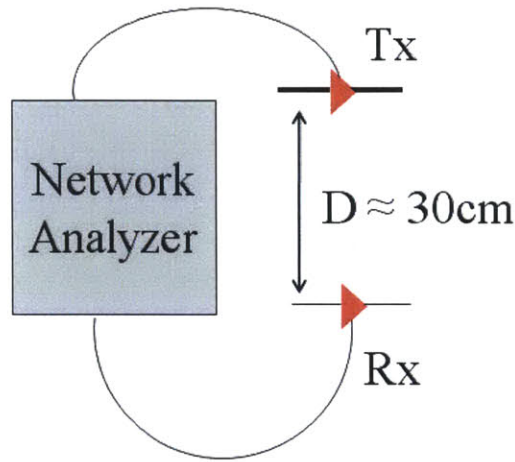


Figure 3-15: Diagram of the experimental setup to evaluate antenna performance. An input signal from the network analyzer propagates through cables to the transmitting antenna, which rests on one of several substrates. Due to impedance mismatch, a portion of that signal is reflected back towards the analyzer (S_{11}). A portion of the power transmitted by the antenna is received by another antenna (S_{21}).

We conducted experiments modeled after the antenna simulations to test the performance of a dipole antenna placed over an AMC sample and several other substrate configurations, including an antenna in free space with no substrate, directly above a metal plate, and spaced 5 mm above a metal plate (Fig. 3-15). To measure both the substrate effect on S_{11} , the return loss, and S_{21} , the transmitted power, we set up an identical receiving antenna 30 cm from the transmitting antenna, and used an HP8501B Vector Network Analyzer for the measurements. To see how changing the antenna geometry would affect performance, we shortened the arms of the transmitting antenna gradually from 60 mm to 5 mm as different substrates were interchanged underneath. The magnitude of S_{11} measured for a dipole of

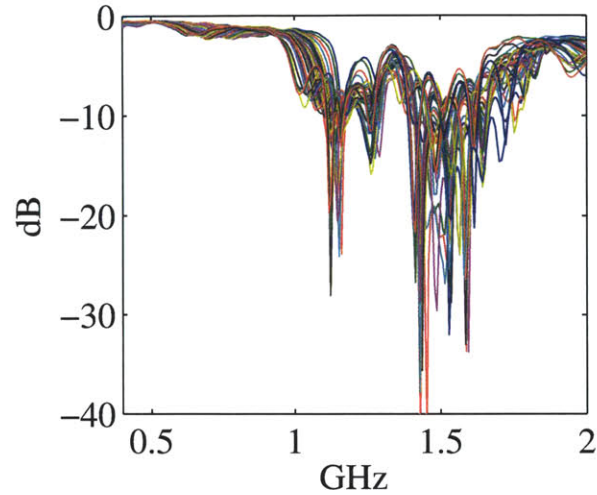


Figure 3-16: Measured S_{11} atop AMC for all antenna lengths, similar to Fig. 3-14(b)

various lengths atop the AMC is shown in Fig. 3-16. While there is some shifting of the S_{11} minimum, the profile is reminiscent of the S_{11} simulation result for the Lorentzian substrate, which was also consistent throughout antenna length changes. It is notable that at least part of this low return loss region corresponds to the positive reflection phase band for the fabricated AMC (Fig. 3-12). The S_{21} portion of the data recorded during the experiment

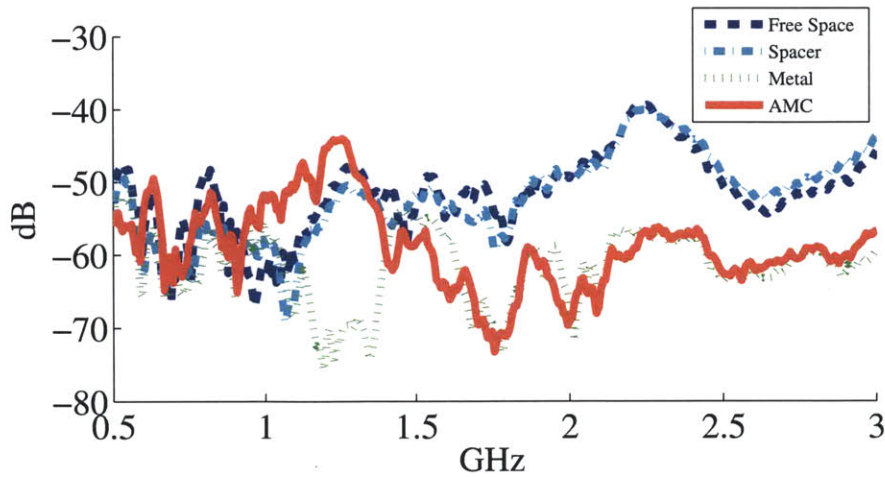


Figure 3-17: Averaged S_{21} for all antenna lengths on all substrates. An AMC performance enhancement is apparent in the 1.13 GHz region. Outside the zero phase region, the antenna atop the AMC behaves like an antenna directly above metal.

relates to how well the antenna in each situation was radiating. Many factors play into

the value of S_{21} , including the return loss, gain and distance between the transmitting and receiving antenna, but given all the parameters held constant in this experiment, S_{21} provides insight as to whether one substrate helps or hurts the antenna it is sitting under. Zooming in on the average S_{21} data in Fig. 3-17, the AMC's resonant region shows an S_{21} level several dB above the rest of the substrates. Additionally, it is interesting to notice trends emerge towards higher frequencies. The cases pair off, with the spacer and free space antenna at a higher S_{21} , and the metal plate and AMC at a lower level. The only time the AMC's performance diverges is where there is anomalous magnetic conductor activity in the region of 1.13 GHz, which boosts the S_{21} of the antenna atop AMC above those of its competitors.

3.3.7 Extension to RFID frequencies

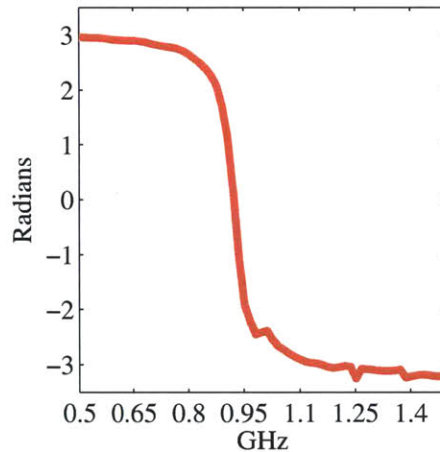


Figure 3-18: Phase of the reflected wave for the 5.1mm thick unit cell.

To verify these results for the RFID frequency band, we performed experiments with a similar AMC prototype, the frequency of which was tuned by making the unit cell slightly thicker at 5.1 mm. This lowered the active frequency by several megahertz to reach 0.92 GHz. The reflection phase measured with the TEM cell confirmed that the resonance was indeed in the correct range (Fig. 3-18), though the bandwidth dropped to around .060 GHz. To measure antenna performance, we again conducted antenna experiments, this time only comparing antennas atop the AMC and 5 mm spacer. Notable about the results are that S_{21} was several dB higher while atop the AMC, even in this case where the input impedance of the antenna

atop the AMC and spacer was about the same (Fig. 3-19). In addition, we performed a test where we placed a commercial RFID tag on top of the AMC substrate 2 meters away from an RFID reader. The reader was able to identify the tag, though with a relatively low RSSI value of -65 dB, indicating there is still room for improvement.

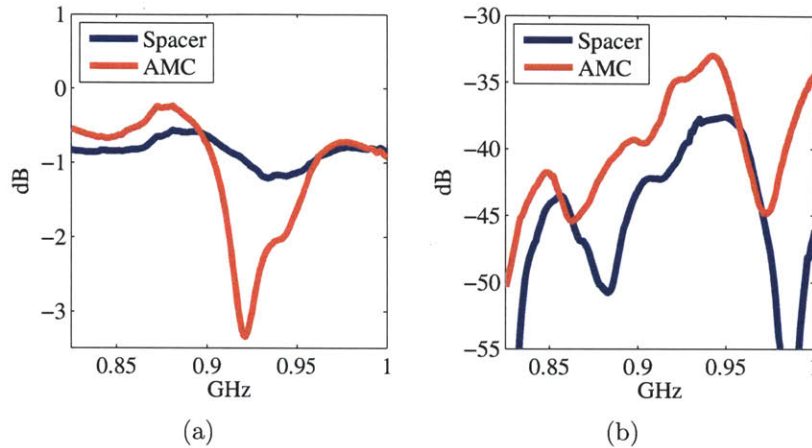


Figure 3-19: (a) S_{11} and (b) S_{21} for antennas placed on top of the AMC and a spacer.

3.3.8 Unit Cell Redesign

While the 5 mm thick unit cell prototypes were successful at reaching the desired frequency, they remain relatively thick compared to other RFID tags designed for metal (Table 3.2). Attempts were made to reduce the overall AMC thickness while keeping the frequency constant by increasing the capacitance to correspond to the decrease in inductive loop height (Fig. 3-20) without any changes to the area of the unit cell. Inductance, which is related to the ring loop size, inevitably dwindles as the cross-sectional area is depleted. In contrast, the capacitance is entirely independent of the unit cell thickness, and can be arbitrarily set by controlling both the size of the ring’s metallic pads, and the thickness and dielectric constant of the material between the ring pads and the ground plane below.

Results of simulations of the thinner structures showed that while it is indeed possible to reduce ring height arbitrarily but retain the resonant frequency by regulating the relevant physical dimensions, it is not without unintended consequences. Figure 3-21 shows that reducing ring height but raising the capacitance causes both an increase in absorption

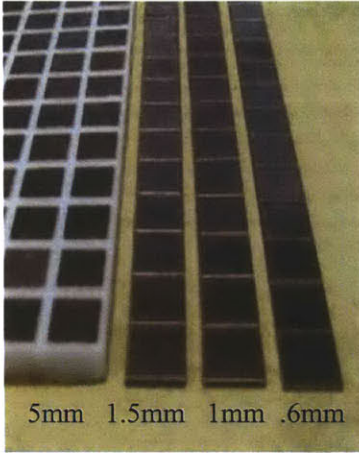


Figure 3-20: AMC prototypes of various heights.

Reference	Thickness(mm)	Read Range (m)
OmniID	1.2	4
Eccopad	1.524	3
MetalCraft	2.16	7.62
Xerafy	2.2	2
Chen2010	3.3	4.2
Nikitin2012	3.62	6.1

Table 3.2: Survey of the reported thickness and read range of commercially available and research tags.

losses within the AMC surface, and a sharp reduction in AMC reflection phase bandwidth. This reduction in bandwidth can be so severe that the AMC phase characteristic effectively disappears.

To better understand the relationship between inductance, capacitance, unit cell dimensions and bandwidth, a model for the AMC surface impedance was considered. The model suggested initially by Sievenpiper for the mushroom array AMC considered contributions to the surface impedance from the capacitance between the mushroom caps and the area of the inductive loop. While sufficient for generating approximate predictions of resonant frequency and bandwidth, several reports have shown that the impedance model assumed by Sievenpiper is overly simplified. Instead, Costa [62] and Samani [61] suggest that the abstracted impedance of the AMC is not dictated solely by the capacitive gap and conductive loop, but should also include the parallel impedance contributed by the conductive ground

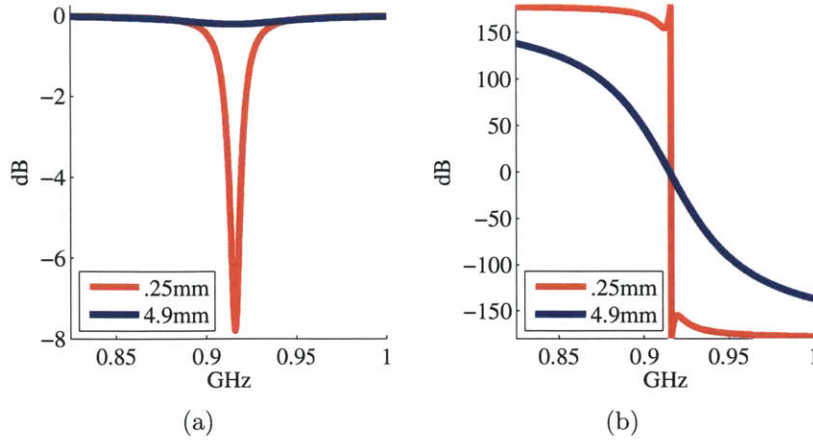


Figure 3-21: (a) S_{11} magnitude and (b) phase for unit cells of different heights resonant at .915GHz.

plane, which reactively represents a conductive short with zero impedance. While this means an infinitely thin AMC would be electrically shorted out, having some finite thickness above the ground plane inserts into the system a transmission line stub (Fig. 3-22). While the stub is still terminated by a short at the conductive ground plane, the reactance no longer has a zero value, instead becomes equivalent to a non-zero inductance

$$L_{sc} = \frac{\sqrt{\frac{\mu\mu_0}{\epsilon\epsilon_0}} \tan\left(2\pi f \sqrt{(\mu\mu_0\epsilon\epsilon_0)h}\right)}{2\pi f} \quad (3.5)$$

where h is the thickness of the AMC, and ϵ and μ are properties of the background material.

To model the reactive components of the surface elements along with the ground plane, Costa [62] suggested that an individual AMC unit cell contributes to the reactance as both a capacitor and inductor in series (Fig. 3-23). Based on that suggestion, and assuming a relation between physical parameters and capacitor and inductor values, Equation 3.4 can be used to derive a reflection coefficient that is a function of physical cell dimensions. For the split ring unit cell introduced above, the capacitance and inductance [63] are

$$C = \frac{\epsilon\epsilon_0 2l_2 t}{d} \quad (3.6)$$

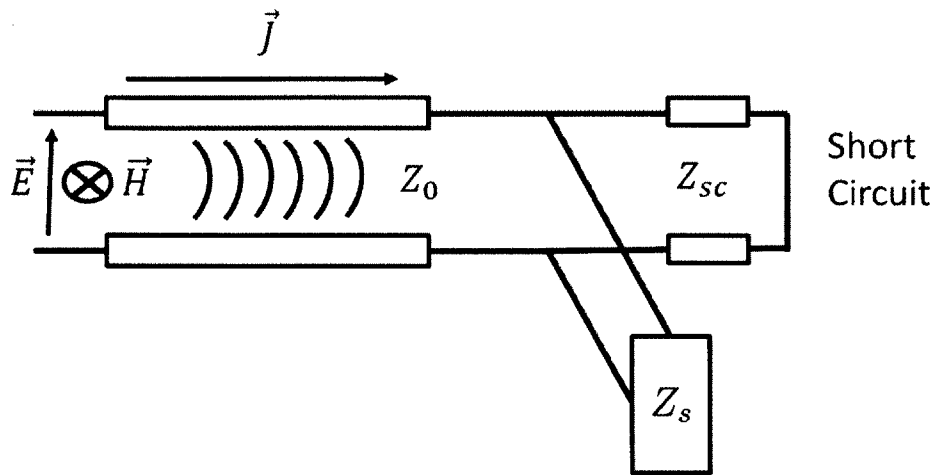


Figure 3-22: Model of AMC surface impedance including the ground plane as a shorted transmission line stub [61].

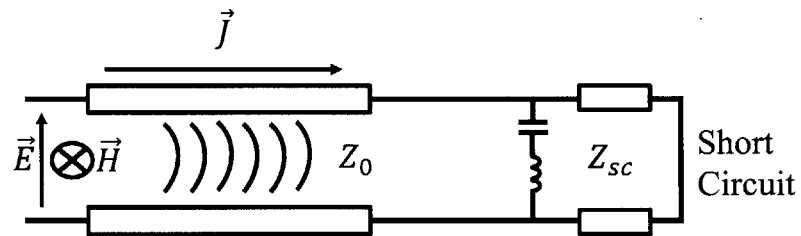


Figure 3-23: Model of AMC surface impedance assuming a series configuration.

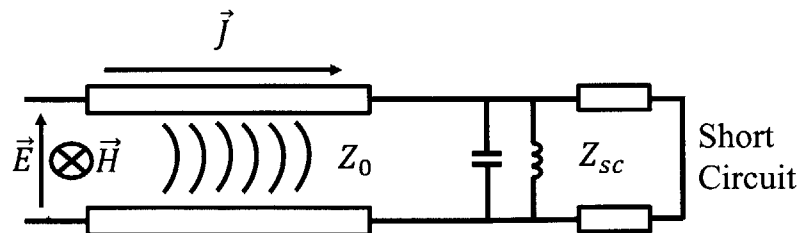


Figure 3-24: Model of AMC surface impedance assuming a parallel configuration.

$$L = \frac{\mu\mu_0 l_1 h}{t} \quad (3.7)$$

where $2l_2 t$ is the surface area of the rings pads, d is the distance between those pads and the ground plane, ϵ is the permittivity of the thin film between the pads, $l_1 h$ is the surface area of the inductive loop, and t is the depth of the loop. The total surface impedance Z_s comes out to

$$Z_s = i\omega \frac{\left(\frac{1}{-\omega^2 c} + L\right)L_{sc}}{\frac{1}{-\omega^2 c} + L + L_{sc}} \quad (3.8)$$

and the reflection coefficient Γ is

$$\Gamma = -1 + \frac{2L_{sc}\omega(-1 + cL\omega^2)}{L_{sc}\omega(-1 + cL\omega^2) - i(-1 + c(L + L_{sc})\omega^2)Z_0}. \quad (3.9)$$

The bandwidth of the phase can be derived by taking the derivative of Γ with respect to frequency at the resonance frequency ω_0

$$\left.\frac{\partial\Gamma}{\partial\omega}\right|_{(\omega=\omega_0)} = -\frac{\pi}{BW}. \quad (3.10)$$

Given that the resonant frequency for this system is

$$\omega_0 = \frac{1}{\sqrt{C(L + L_{sc})}} \quad (3.11)$$

the bandwidth comes out to be

$$BW = \frac{L_{sc}^2}{2c(L + L_{sc})^2 Z_0} \quad (3.12)$$

which means increasing the capacitance or inductance of the unit cell decreases the AMC bandwidth. While decreasing the inductance L as much as possible would increase the bandwidth, in the limit as L approaches zero the formula for the maximum bandwidth is

$$BW = \frac{1}{2cZ_0} \quad (3.13)$$

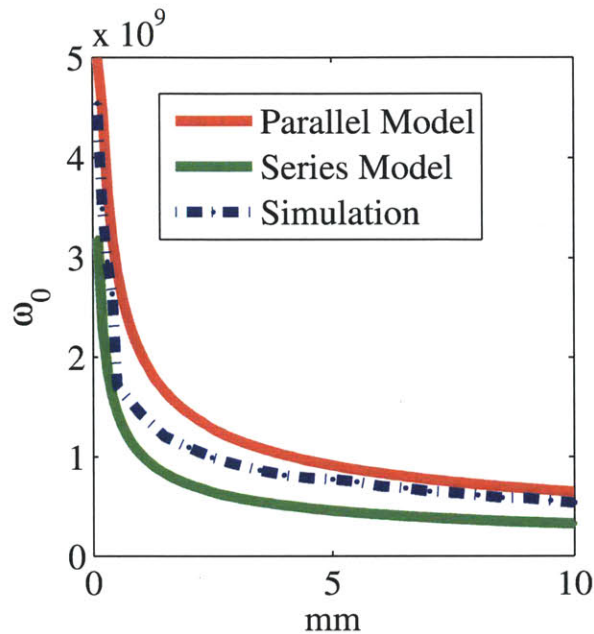


Figure 3-25: The predicted resonant frequency of the split ring AMC.

which would imply that at .915 GHz, an AMC with a thickness of 5 mm has a maximum possible bandwidth of 270 MHz, or 55 MHz if the thickness is reduced to 1 mm. If the Costa model were accurate, this would predict that AMCs would be an excellent solution for near metal RFID tags, as even a substrate half a millimeter thick retains enough bandwidth to benefit an antenna with its positive reflection coefficient over the entire North American RFID band. Unfortunately, the series impedance model was not fully supported by simulations. The model does accurately predict the increase in resonance frequency as substrate thickness drops (Fig. 3-25) and the severe drop in bandwidth as substrate thickness drops while the resonant frequency is held constant (Fig. 3-26). However, the series model fails to explain the rise in bandwidth observed with increased unit cell inductance realized by decreasing the width (w) of the split rings. Instead, I suggest the use of a modified lumped circuit model, one where the contribution of the inductance inherent to the unit cell is in parallel with both the capacitance and the shorted transmission line stub that represents the ground plane (Fig. 3-24). In this model, the surface impedance takes the form

$$Z_s = \frac{wL(-i\omega L_{sc})}{-\omega(L + L_{sc}) + cLL_{sc}} \quad (3.14)$$

and the reflection coefficient Γ is

$$\Gamma = -1 + \frac{i\omega 2LL_{sc}}{Z_0L_{sc} + L(Z_0 + \omega L_{sc}(i - \omega Z_0 c))}. \quad (3.15)$$

and following Equation 3.10 we derived the bandwidth

$$BW = \frac{1}{8CZ_0} \quad (3.16)$$

or

$$BW = \frac{\omega_0^2(L + L_{sc})}{8Z_0} \quad (3.17)$$

which means that increasing the capacitance C , or reducing inductance L , decreases AMC bandwidth. While increasing the inductance contribution from the unit cell structure does increase the bandwidth, it only increases to a certain point. Even if the value of the inductance L becomes very large, because of the fact that

$$\left(\frac{LL_{sc}}{L + L_{sc}}\right) \approx L_{sc} \text{ where } L \rightarrow \infty \quad (3.18)$$

there is a bandwidth limit set by the thickness of the substrate. Of course, in the event the structure itself has less inductance than the shorted stub to the ground plane, the bandwidth can be limited even further. This explains the lack of bandwidth apparent in Figure 3-21, and points to an important design rule, that for low profile AMCs the maximum bandwidth for a particular height can only be achieved when the inductance due the AMC structure and the overall substrate thickness are equal.

While the parallel model offers a more accurate prediction of resonant frequency (Fig. 3-25) and maximum bandwidth for a substrate of a particular height at a given frequency (Fig. 3-26), even for other AMC geometries like the Sievenpiper mushroom, it offers a less positive picture of the potential application of AMCs for UHF RFID. While a 5 mm substrate could be expected to support a bandwidth close to 80 MHz, substrates at 1 mm benefit from only 14 MHz of bandwidth, and only 6 MHz at half a millimeter thickness. This analysis also

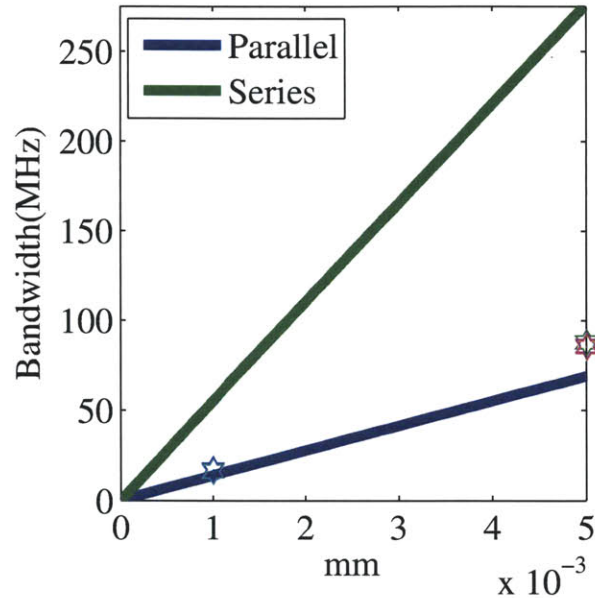


Figure 3-26: AMC bandwidth predicted by series and parallel equivalent circuit models.

demonstrates that the split ring AMC does not offer any significant performance benefits compared to mushroom designs. From a bandwidth perspective, the split ring offers no bandwidth enhancement. Though the split ring was illustrative for the purposes of analysis, intuitively decoupling geometries which contribute separately to capacitance and inductance, the added parallel inductance is shorted by the ground plane, which makes the polarization dependent loop an unnecessary feature.

3.4 Conclusions

In this chapter, I discussed the application of a split ring resonator based Artificial Magnetic Conductor to augment the function of planar dipole antenna based RFID tags used to identify metal objects as part of a UHF RFID system. A 5 mm thick substrate prototype was fabricated and tested experimentally, both to observe the phase reflection characteristics, and to confirm the enhancement of antenna performance. The unit cell was also instructive for the construction of a lumped element model for prediction of AMC resonant frequency and bandwidth.

3.4.1 AMC Implications

The experiments, lumped element model and full wave simulations have led to the conclusion that while AMC substrates can improve planar antenna performance, the beneficial effects of the substrate are very much dependent on substrate thickness. Proximity to the ground plane limits the inductive reactance of the surface and desiccates the available bandwidth over which an AMC constructively reflects electromagnetic waves. Low inductance values also necessitate high capacitance within the AMC structure. While the required capacitance could be achieved with large area plates, it can also be reached with small thickness. The requirement of large capacitance does not, however, place any minimum on the footprint of AMC unit cells.

Reviewing the requirements of an AMC for RFID in light of the findings in this chapter, it is clear that while the bandwidth of thin AMCs may be limited, it is possible to design small unit cells. Whether the beneficial bandwidth available at a particular height is enough to enable a low lying RFID tag to operate is left for future work. Other topics that require study are effective methods to produce thin AMCs with miniaturized unit cells and antenna designs to ensure the tag placed on the AMC is able to function properly.

3.4.2 Fabrication Implications

Though additive manufacturing played a relatively minor role in this chapter given challenges associated with the electromanetics of the problem, the flexibility of additive manufacturing significantly streamlined the task of 3D AMC prototyping. All dimensions of the cubes that made up the core of the individualized cells were systematically varied to shift the cell resonant frequency from 1.13 GHz down to 920 MHz and within the operational band of UHF RFID. Aside from the individual metamaterial units, the scaffold designed to hold the cells in place ensured proper periodicity and structural rigidity, allowing tests to proceed without undesired shifts of geometry and materials.

Chapter 4

Lost in Transmission

Reflecting on my AMC fabrication experience, it was evident that additive manufacturing could be useful for prototyping other metamaterial structures. As mentioned earlier in chapter 2, most conventional metamaterials rely on planar substrates as supports for planar unit cell designs, initially permitting only planar array configurations. In those situations, a dimensional increase for either the unit cells or array would require additional assembly and labor, and at the same time result in a significant increase in loss. While additively manufactured substrates offer only a limited material selection, making it more difficult to incorporate dissimilar material inclusions, they can more readily allow for the extension of metamaterials into a third dimension, acting in supporting roles on both the unit cellular level and for the overall array architecture.

In this chapter, I further demonstrate additive manufacturing for the rapid fabrication of arrayed 3D metamaterial structures. I begin by motivating the need for 3D metamaterials from the perspective of loss reduction and recounting the evolution of S-ring metamaterials, the unit cell employed throughout the rest of the chapter. That is followed by additive fabrication of 3D S-ring arrays and testing their transmissive properties. Finally, to exemplify the utility and flexibility of the fabrication method and cell design, I use additively manufactured S-rings to produce a transmissive metamaterial device, a plano-concave lens, that features a negative refractive index.

4.1 Motivation for 3D Structures: Minimization of Loss

Multilayer stacking and weaving are the two of the standard methods which have been employed to increase the dimensionality of planar metamaterial arrays. Aside from being laborious, the downside of these multilayer approaches is an increase in losses which can seriously diminish the value of undertaking such an assembly project. Losses in metamaterials stem from two sources:

- Ohmic losses: These arise as induced currents flow along conductive elements within a metamaterial, which dissipate energy as heat.
- Propagation losses: Energy dissipates as electromagnetic waves travel through dielectrics substrates with non-zero loss tangents. These substrates are those upon which the current carrying conductive elements are supported.

These losses can be exacerbated by resonances within the metamaterial, resonances which are often necessary to generate negative refraction but in the process cause large currents and high field levels that are rapidly dissipated as heat. A third source of effective loss is the unwanted reflections off of, as opposed to propagation through, the combination of dielectric and conductive material used to fabricate a metamaterial device [21]. Summed together, losses are especially pronounced in multi-layer metamaterial constructs [64, 65] as each layer absorbs and reflects a percentage of the incident energy, severely reducing a device's overall output.

4.1.1 Self-Supporting Metamaterial Designs

Several metamaterial unit cell designs with self-supporting 3D geometries have been proposed that aim to reduce losses by eliminating the requirement of dielectric substrates [66, 67, 68, 69]. In many metamaterial designs that use planar conductive inclusions to generate a negative refraction index material, the dielectric substrates are used merely as support material, serving no purpose other than to keep the more important current carrying elements in place in the array. By fashioning unit cell geometries that are interconnected and self-supporting, the dielectric can be removed at no functional cost, improving efficiency by

not wasting energy that would otherwise be reflected by or absorbed within the substrate material.

4.2 S-Ring Metamaterial Unit Cell

One such unit cell whose geometry invites both interconnected and self-supporting structure is the S-ring. The S-ring was initially introduced as an alternative to the Pendry's original split-ring resonator, which is limited in that its negative permeability and negative permittivity frequency bands do not overlap. Unable to produce a negative refractive index by itself, split-ring resonators are normally combined with wire arrays to satisfy the negative permittivity requirement. In contrast, the S-ring structure has the advantage of simultaneously supporting negative permittivity and permeability without the addition of supplemental elements [70].


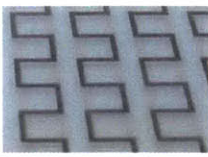
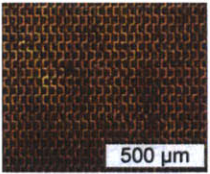


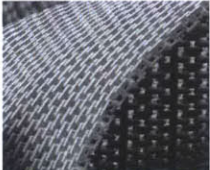
S-Ring	Unit Cell	PCB	μ Fabrication
Original			
Bi-anisotropic			

Figure 4-1: The original [70] and bianisotropic [71] S-ring metamaterial unit cells, the interconnected versions of which were first fabricated using PCB methods [72], and later made into large arrays with microfabrication techniques [73, 74]. The connecting via between the two S shapes makes the bianisotropic S-Ring a self-supporting structure.

4.2.1 Early S-ring Examples

Inherently a 3D design, the first S-rings were fabricated using PCB techniques on FR4 substrates with S-shaped traces etched on both sides(Fig. 4-1). When exposed to properly oriented electromagnetic waves, the applied magnetic fields induce currents through the ring’s two loops resulting in a magnetic resonance and negative permeability, while the metallic strips act like a plasma medium with negative permittivity. Put up against a similarly produced split-ring resonator, dissipation loss through the S-ring was found to be significantly lower at only $-1.75dB/cm$ compared to $-6.53dB/cm$ for the split-ring [70].

To further improve the design, several variations on the S theme were introduced including the crinkled [75] and bi-anisotropic S-rings [71]. Both of these designs lowered resonance frequencies without increasing the the overall structure dimensions by incorporating vias between the two S shaped layers. It was the addition of the vias, however, that proved to be the crucial step, adding another dimension of interconnectivity to the unit cell. This made it possible to produce self-standing S-ring arrays, which were subsequently fabricated entirely out of gold using a three layer UV and X-ray lithography process [74]. The relative dimensions of the S-ring’s metallic segments where thickened such that the structure would be self-standing, instead of being reliant on a substrate to hold the S shape. Referred to as a meta-foil, this implementation contained unit cells with dimensions $30 \times 20 \times 15 \mu m^3$ and a maximum figure of merit

$$FOM = \frac{Re(n)}{Im(n)} \quad (4.1)$$

of 5.6 at 3.47 THz, benefiting significantly from the lack of supporting substrate.

4.2.2 Additively Manufactured S-Rings

The interconnectedness of bi-anisotropic S-rings demonstrated in the metafoil makes them a prime candidate for additive manufacturing. Though the dimensions used in the metafoil implementation are on the order of microns and far below the resolution of automated additive processes currently available, dimensions can be scaled up to more feasible lengths. This scaling of dimensions shifts the structure’s resonance down to a lower frequency band but

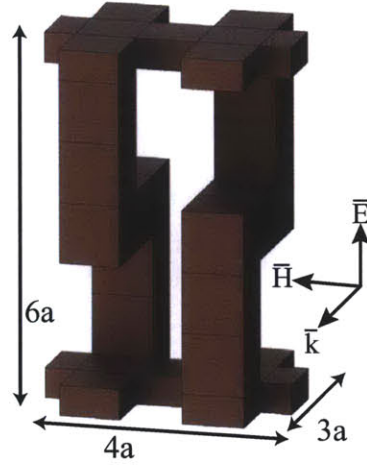


Figure 4-2: Solid model of the S-ring unit cell. As the response of cell is polarization dependent, all experiments were done with the electric and magnetic fields oriented as in this figure. The initial implementation of the cell was with the $a = 1.46$ mm.

preserves the metamaterial characteristics. To study the frequency dependent characteristics of a scaled S-ring with dimensions $13.14 \times 8.75 \times 5.84$ mm³, simulations were performed using commercial finite element software (HFSS, Ansoft). With the unit cell oriented relative to the incident wave as in Fig. 4-2, and surrounded by periodic boundary conditions, the resulting scattering parameters (Fig. 4-3) reveal a transmission peak at 10.7 GHz, with a maximum S_{21} value of -0.2 dB, corresponding to nearly 99.95% transmission. The S-parameters were then used to retrieve effective material parameters (Fig.4-4) according to a standard procedure outlined in [76]. Though the imaginary part of the derived permittivity is negative below 10.7 GHz, precluding the classification of this structure as an effective medium in that regime [73], simultaneous negative permeability and permittivity between 10.7 and 12.2 GHz result in a low-loss NRI region with values ranging from -2 to 0 .

4.2.3 Fabrication and Testing

To verify the simulation results, a 10×10 array of S-ring unit cells was fabricated using additive manufacturing. The sample was constructed by an Objet Connex 500, using the Transparent 720 material. Support material was removed by hand and with the aid of a brush. After the surface was cleaned, silver paint was applied to make the surface of the S-rings conductive. The resistance across the length of the coated array was measured to be

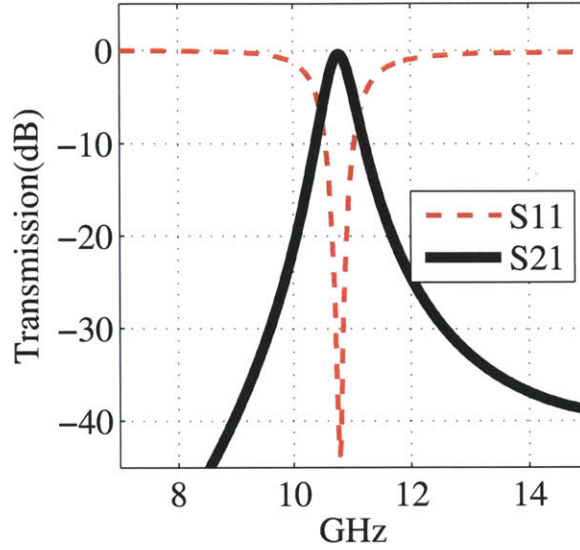


Figure 4-3: The simulated S-parameters for the unit cell when the parameter $a = 1.46$ mm, with the passband centered at 10.7 GHz.

less than $.1 \Omega$ on an analog ohmmeter.

A transmission experiment was performed to verify the electromagnetic characteristics of the metalized S-ring by observing the S_{21} pass band that was found in the unit cell simulation. The sample was placed between transmitting and receiving horn antennas connected to a vector network analyzer. The frequency of the analyzer signal was swept from 6 – 15 GHz, and the transmitted S_{21} was recorded with the metamaterial in place. Due to a lack of calibration for the network analyzer, measurements were also taken with only air between the antennas, to give an idea of potential dissipation loss within the metamaterial. The experimental setup was also replicated in a simulation environment for comparison purposes.

The results from the simulation and experiment are both in agreement regarding the existence of a transmission band (Fig. 4-5). Unlike the S_{21} from the unit cell simulation, which resulted in near perfect transmission, transmission in the array experiment and simulation is below 0 dB, as not all the energy radiated is captured by the finite sized antenna ports. For the analyzer measurements, the lack of calibration resulted in a significant amount of noise being present. Despite the noise, a transmission band centered at 10.6 GHz is discernible. When compared to the transmission through air, the paint-coated metamaterial layers resulted in only a 1 dB/cm drop in transmission corresponding to a loss of about

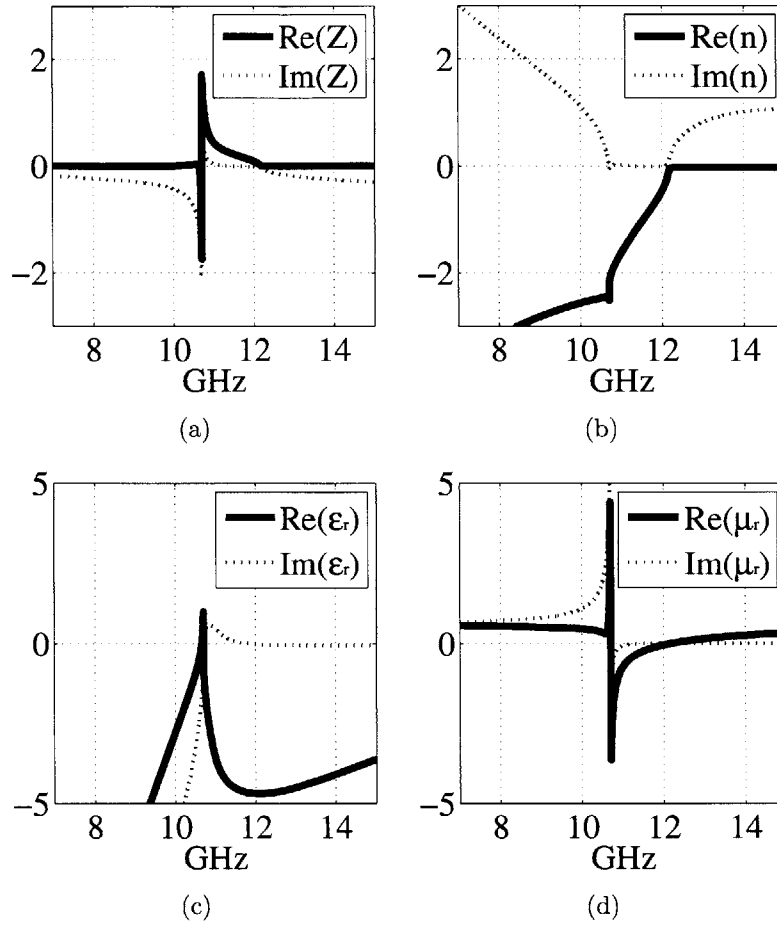


Figure 4-4: Real and imaginary parts of the S-ring’s retrieved (a) normalized impedance, (b) refractive index, (c) effective relative permittivity and (d) effective relative permeability. Real and imaginary parts of the S-ring’s retrieved refractive index. The imaginary part is near zero between 10.7–12.2 GHz, while the real part is negative.

2 dB/cm.

4.3 S-Ring Metamaterial Lens

To further exemplify the utility of additively manufactured metamaterials, I use the S-ring unit cell as the basis for building a metamaterial lens. The lens design is plano-concave, a shape that focuses incident plane waves only when the refractive index of the lens material is negative.

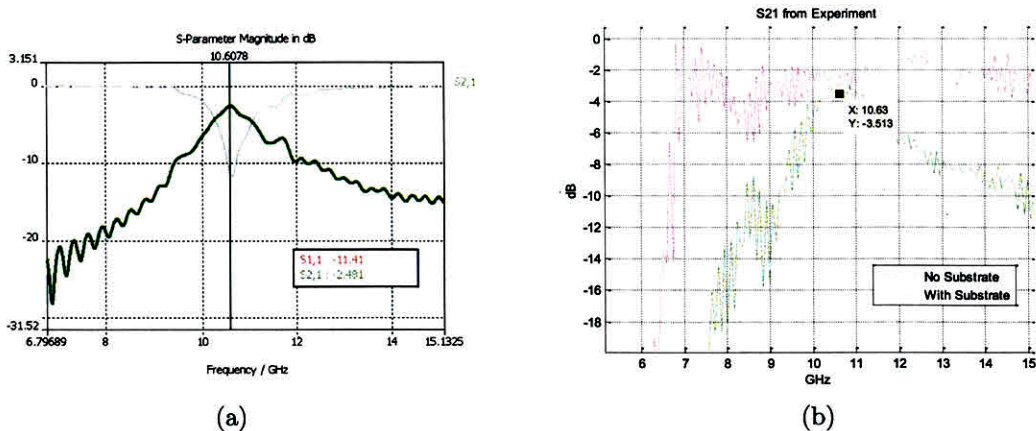


Figure 4-5: (a) Simulated transmission through a single layer of S-rings between two horn antennas has a transmission peak around 10.6 GHz, similar to (b) the results from an experiment where S_{21} was measured with and without the metamaterial substrate between the two horns. The measured results are noisy due to network analyzer operating in an uncalibrated mode.

4.3.1 Negative Index Lenses

Imaging and focusing are two of the primary uses for lens technology, and are seen as possible venues for enhancement with metamaterials. Much attention has been given to the Vesalago perfect lens, which requires cuboid or cylindrical geometries and a refractive index of $n = -1$ to enable sub-diffraction imaging of objects nearby. In contradistinction, the focusing of incident plane waves with homogeneous material is not possible without lenses sporting more complex geometric profiles [77]. Lenses made from positive index material with spherical or hyperbolic convex curvatures can focus incident plane waves, but aberrations and reflections off the lens surface due to an impedance mismatch with free space limit transmitted intensity and increase the size of the focal region. As an alternative to focusing lenses made from positive refractive index material, concavely curved lenses featuring a negative refractive index also allow for focusing, but have the added potential to generate fewer reflections by having an impedance that closely matches the impedance of free space. Negative refractive indices also allow for decreased Seidel aberrations [78], which can reduce the area that contains the transmitted energy on the focal plane. Both increased transmission through the lens and a tighter focusing of that transmitted energy translate into increased field intensity at the lens's focal point. In addition to performance enhancements, negative

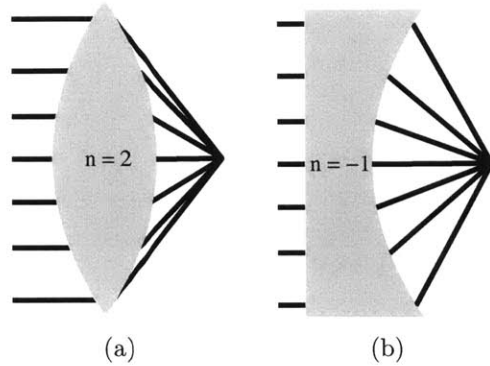


Figure 4-6: (a) A biconvex lens with a positive refractive index and (b) a planoconcave lens with a negative refractive index can both focus incident plane waves, but negative index allows for lenses that are more compact, with few reflections and decreased aberrations.

lenses can be significantly more compact than conventional lenses, requiring only a fraction of the volume needed for a lens made from positive index material. Metamaterials used to realize negative index materials also tend to have lower densities than conventional positive index materials, resulting in lighter weight systems [79].

4.3.2 Related Metamaterial Lens Work

The first implementation of a 3D NRI plano-concave lens relied on an array of split-ring resonators and wires to obtain the required negative constitutive parameters [80]. The lens was designed to have a refractive index of $n = -1$ at 14.8 GHz, and featured a stepwise approximation of a 24.4 cm radius of curvature and had a corresponding focal distance of 12.2 cm. While focusing was observed, unwanted reflections and material losses compounded through the five layer structure prevented significant intensity gains at the focal point when compared to an open aperture, reaching only as high as 5 dB. A positive index lens in the same experiment measured a gain of approximately 10 dB.

An alternative plano-concave lens construction meant to avoid the complexities of 3D split-ring assemblies and operate at much high frequencies was constructed by Beruete et al [81]. The geometry of each unit cell was relatively simple: a circular hole drilled at the center of a rectangular piece of sheet metal. Arrays of holes were drilled then placed atop one another with a thin dielectric layer between each of the ten holey layers. The lens was

built with a 100 mm radius of curvature and refractive index $n = -1$ at 53.5 GHz, making the focal length 50 mm. Though simulations predicted low losses for this unit cell design and simulations of the overall lens predicted a focal point nearly as tight as a homogeneous, non-staircased lens, experimentally this lens failed to produce significant fields in the focal region, reaching a relative gain of only 3 dB versus an open aperture.

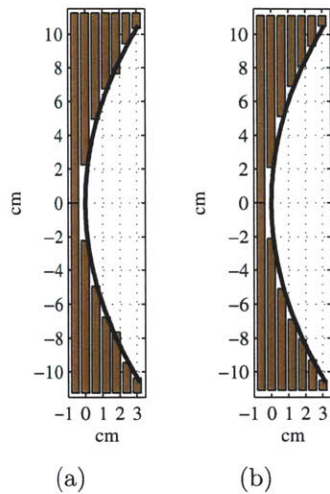


Figure 4-7: The profile of the plano-concave lens after the cells encompassed or cut through by the hyperboloid of Eq. 4.2 were removed from the stack of seven S-ring arrays along, as seen from the \vec{E} (a) and \vec{H} (b) directions.



Figure 4-8: Solid model of the entire planoconcave lens made up of seven S-ring layers.

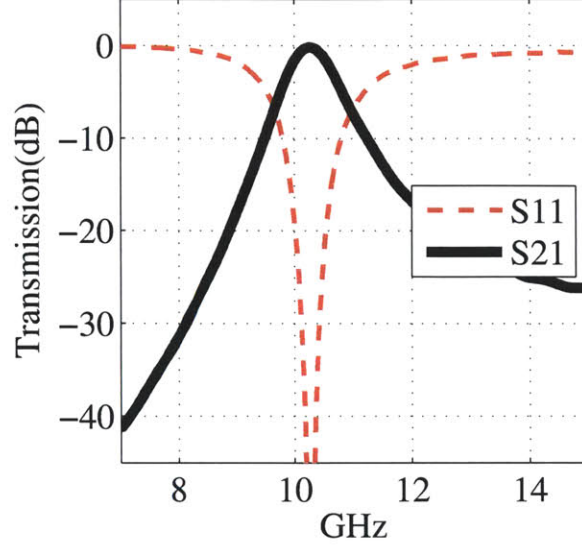


Figure 4-9: The simulated S-parameters for the unit cell when the parameter a is 1.5 mm, with the passband centered at 10.25 GHz.

4.3.3 S-Ring Lens Design

I designed the S-Ring NRI plano-concave lens by virtually stacking seven S-ring arrays atop one another with 1.5 mm between each layer. Unit cells were then removed from the top six layers to give the stack a discretized concave curvature approximating a hyperbolic surface $S(r)$ where

$$(f - n \cdot r)^2 = S(r)^2 + (f - r)^2, \quad (4.2)$$

in which r is the distance from the center axis of the S-ring stack, such that plane waves incident upon the planar surface of an ideal plano-concave lens with this profile will focus at a distance $f = 90$ mm, given a refractive index of $n = -1$. Unit cells cut through by the hyperbolic surface were removed entirely only if their geometric center was within the volume encompassed by the hyperboloid (Fig. 4-7). To bring the unit cell response toward the center of the available measurement equipment, the dimensions of the S-ring were slightly altered by setting $a = 1.5$ mm. This shifted the simulated S_{21} passband to 10.25 GHz (Fig. 4-9), and slightly changed the effective material properties (Fig. 4-10).

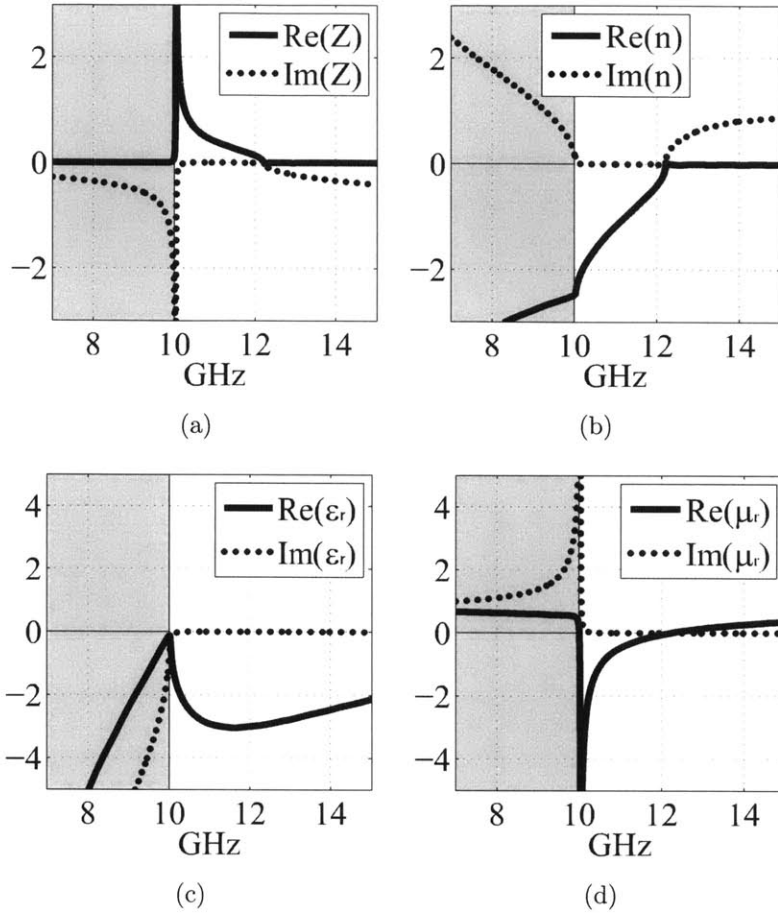


Figure 4-10: (a) Real and imaginary parts of the S-ring's retrieved (a) normalized impedance, (b) refractive index, (c) effective relative permittivity and (d) effective relative permeability were slightly redshifted when the parameter a was changed from 1.46 mm to 1.5 mm.

4.3.4 Lens Fabrication

After creating a graphical model of the lens layers (Fig. 4-8), polymer S-ring arrays were fabricated using the Objet Connex 500. Each array consisted of 35×25 unit cells, minus those subtracted to form the lens curvature. The total number of unit cells in the seven lens layers was just over 4,000. Support material was removed from the printed parts with the aid of a 2% NaOH bath and high pressure water jet system.

The next step in the fabrication process was covering the entire surface of each layer with a conductive coating. Two alternative methods to silver paint were considered, the first being aluminum vacuum evaporation. For this process, parts were suspended by thin

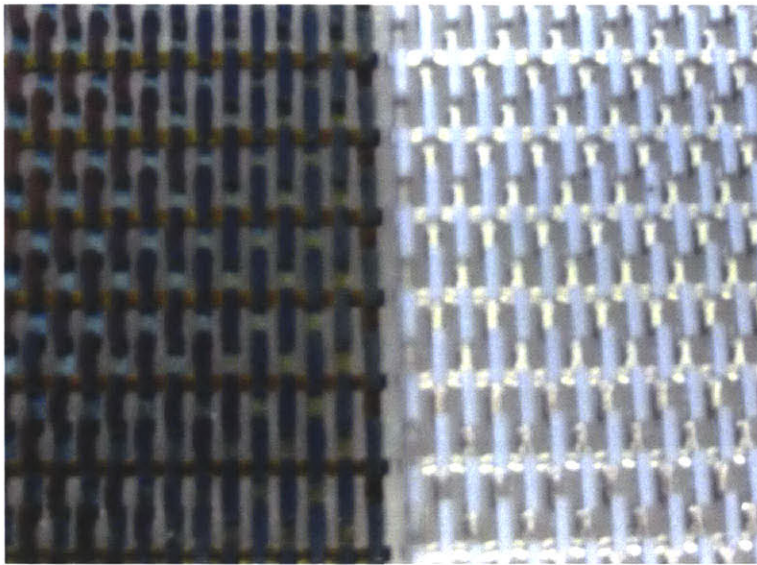


Figure 4-11: A close up of two S-Ring arrays that went through the aluminum evaporation process. The coating on the left appears contaminated as the polymer outgassed during an extended, high rate deposition. The film on the right which was deposited in several stages with a lower deposition rate, appears cleaner and was measured to have a significantly lower resistance than the contaminated film.

wires on a rotating rack inside a large vacuum chamber. Once in a state of vacuum, large currents running through tungsten electrodes caused small pieces of aluminum to evaporate. Once in a vapor state, aluminum particles begin to deposit on the surface of the hanging parts, eventually forming a thin film. One concern regarding the use of vaporized aluminum is that the process of vaporization involves resistive heating. The vaporized metal particles carry a significant amount of that energy and transfer it to the polymer substrate surface. The total incident energy throughout the deposition process adds up with every particle, with little energy leaving the coated surface due to the absence of conductive or convective heat transfer through the vacuum of the deposition chamber. This can pose problems for a polymer S-ring matrix, as the glass transition temperature of the polymer is only 70° Celsius. Without care, deposition could cause melting, warping and out-gassing. One such example occurred when an attempt was made to deposit a 10 μ m film of aluminum in one deposition. It resulted in the polymer melting and out-gassing, ruining several S-ring arrays and all the deposited films, which no longer resembled aluminum in both appearance and conductivity (Fig. 4-11). To prevent damage to other pieces, the time and deposition rate of

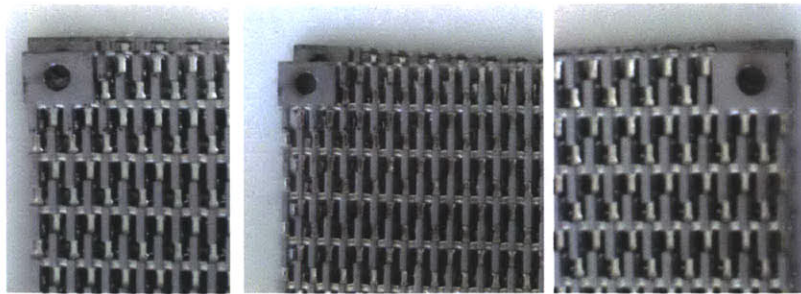


Figure 4-12: Examples of the degree of distortion introduced by softening of the underlying polymer S-rings during the deposition of Aluminum.

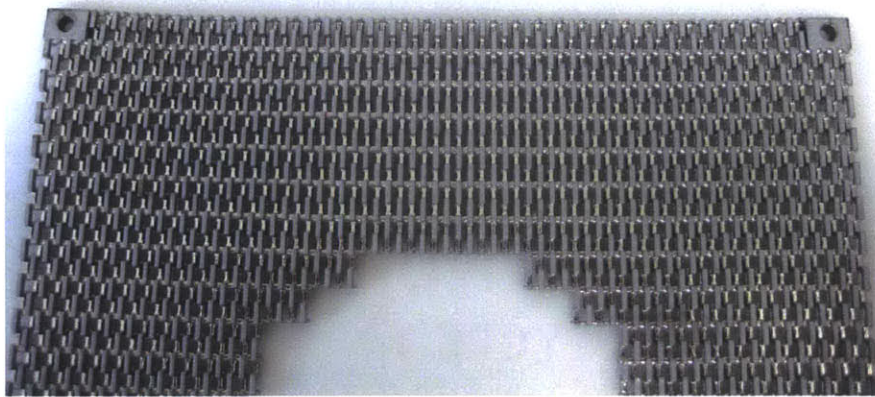


Figure 4-13: Lens layers emerged warped from the evaporation chamber. This layer was hanging by both corners during the deposition, when added heat from deposition particles and gravity joined forces to produce the bow seen here.

the metal films were limited in order to minimize detrimental effects to the polymer matrix. Multiple depositions were performed to ensure full coverage of each layer and to maximize the metal film conductivity of the film. As the aluminum evaporation took place in an industrial facility, it was difficult to monitor the process to ensure all thermal side effects could be avoided, even with the lower deposition rates. Significant warping was observed in several aluminum coated arrays (Fig. 4-12, 4-14), most due to improper fixturing of the parts. Layers were hanging by their corners during the deposition, susceptible to gravity induced strains (Fig. 4-13). Distortions were significant enough to prevent proper lens assembly (Fig. 4-15).

As an alternative to uncontrolled vaporization, access was secured to a Perkin Elmer 4400 sputterer with a chamber large enough to handle individual S-ring layers. Inside the cham-

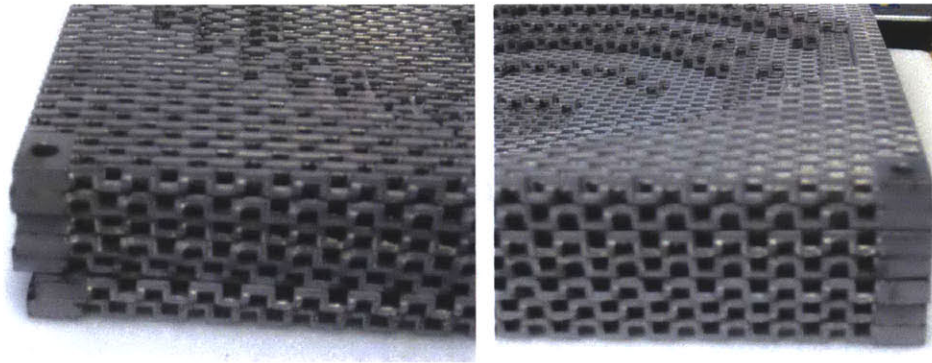


Figure 4-14: Distortions from the Aluminum deposition made it difficult to align the layers.

ber, the S-ring arrays rested on a flat aluminum tray during the depositions, which lasted 15 minutes. In this system, the deposition process begins with the striking of an Argon plasma, the ions of which bombard a charged copper target. Copper atoms are knocked free by the high energy ions, and deposit at a rate of 200 angstroms per minute on the polymer substrate and the surface of the chamber. Both sides of the layers were coated twice, creating a film approximately 4 microns thick. Although sputtering is generally a directional process, the open cellular architecture of the S-ring array allowed for sufficient coating of sidewall surfaces.

While thermal issues loomed over this high energy process as well, the sputter deposition was more controlled, suffering from significantly less distortion and warping as gravity was taken out of the equation. It was observed that immediately after deposition the polymer temperature was elevated, though the interconnected structure was sufficient to support itself and prevent warpage. However, the higher temperatures caused the polymers yield strength to drop to the point that handling immediately after deposition would result in array deformation. To prevent damage, the structure was left to cool at atmospheric pressure until the temperature would normalize, which took only a few moments.

After all layers were coated, they needed to be assembled into the lens (Fig. 4-16). To ease final assembly, solid blocks featuring predefined holes were included at the corners of each layer, through which nylon bolts were inserted. Plastic washers and foam were used to separate the layers. The weight of the assembled lens was 420 gm.

The thermal issues that I had to deal with during fabrication were the result of using low

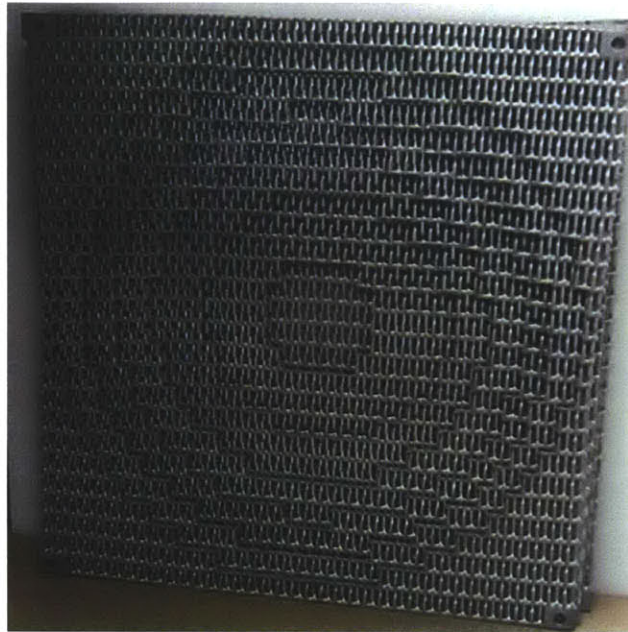


Figure 4-15: The aluminum clad layers for the planoconcave lens, which could not be properly assembled.

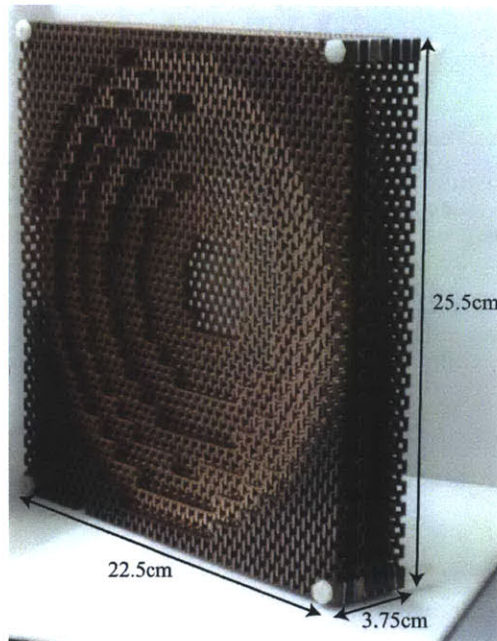


Figure 4-16: The assembled planoconcave lens consisting of 7 copper clad polymer layers in the propagating direction.

temperature polymers to fabricate the S-ring arrays, and using high temperature processes to coat the arrays with conductive films. Other materials and processes could have avoided

some of these difficulties, but raise other issues. For example, direct metal printing, with either 3D printing or selective laser sintering, could have avoided the entire coating step. This option, however was either too expensive an endeavor to undertake, or deemed beyond the capabilities of the process by the practitioners that would have been charged with the task. Printing structures with ceramic material would also have removed any thermal obstacles. Alternative coating methods were also considered, such as electro-less plating, electroplating, or dip coating with conductive paints. These coating options benefit from being near room temperature processes, but may require complex chemistries or suffer from reduced conductivities compared to deposited thin films.

4.3.5 Single Layer Transmission

To experimentally verify the behavior of the S-ring structure and evaluate any difference between the two coating methods, the transmissivity of one complete layer was measured (Fig. 4-17). The layer was again oriented as in Fig. 4-2 with respect to the incident signal and placed between two horn antennas spaced just over 4.5 mm apart. This time, the network analyzer was calibrated, and in the case of only air between the horns measured a drop of 2dB in received power across all frequencies. Measurements with the copper coated layer show a peak in S_{21} that reaches the same -2dB level, confirming the low loss characteristics of the S-ring and the quality of the deposited film. The observed pass band also coincides with the negative refractive index region predicted by simulations for this S-ring geometry. Lower transmission levels at frequencies above the transmission peak are attributed to reflections caused by the impedance mismatch with free space, as opposed to absorption within the metamaterial. Transmission through the aluminum coated array at it highest point was 4.5 db less than the copper S-rings, with the frequency of maximum transmission shifted down to 9.5 GHz. This significant difference in performance is attributed to the higher resistance of the aluminum film. Measured with a digital multimeter, resistance from one corner to the other on the full copper array was less than $.8\Omega$, compared to 1.2Ω for the aluminum. While it is true that the conductivity of bulk copper is slightly higher than that of Aluminum, the reason for the disparity is most likely film quality, given the issues of melting and outgassing shown earlier. The shift in frequency of the aluminum measurements

is likely due to slight warping experienced during the coating process. The sensitivity of the pass band was exemplified earlier, with the S_{21} peak shifting by 500 MHz with only a .04 mm change in design dimensions. Due to the poor transmission performance of the aluminum coated single layer, and fact that assembly was complicated by distortions to most of the layers, further lens experiments were only conducted on the assembled copper coated layers.

4.3.6 Copper Lens Evaluation

The setup used to evaluate the entire lens experimentally consisted of the lens suspended by wood supports centered on the y-axis occupying the space between $y = -40$ mm and 0 mm, in line with a transmitting antenna placed at $y = -340$ mm facing the planar surface of the lens (Fig. 4-18). The distance between the transmitter and lens was 300 mm, ten times the wavelength at 10 GHz, enough for the signal incident on the lens to resemble a plane wave. A receiving X-band horn antenna was placed on a computer controlled XYZ stage directly behind the concave side of the lens. The antenna was stepped at 7.5 mm intervals throughout a $(150\text{ mm})^3$ volume and the received power was recorded for 200 frequencies

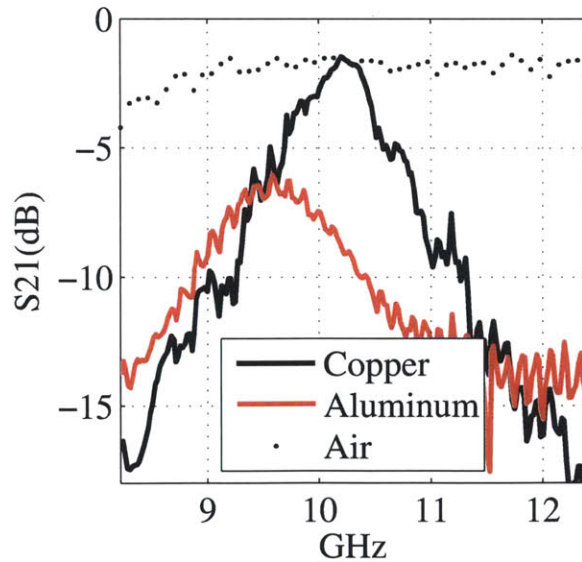


Figure 4-17: The measured transmission through one S-ring array layer when coated with copper and aluminum, compared to transmission through air. S_{21} for the copper samples reaches the level of the uncoated S near 10.25 GHz, while the peak for the aluminum coated array is significantly lower in magnitude and shifted in frequency.

from 8.2 – 12.4 GHz to build a 3D spatial power map. The Z-stage holding the receiver consisted of nonmetal parts to minimize spurious reflections that could disturb the measurements. Numerical simulations of the experimental setup were performed using HFSS with and without the lens in place. Due to limited computational resources, a symmetry plane was used to reduce the memory required for the simulation. The entire volume containing the lens and transmitting antenna was surrounded by a radiation boundary. Simulation results show that while the E-field disperses and weakens as waves propagate away from the small aperture source, there is focusing in the presence of the lens with the E-field magnitude in the focal region much greater than without the lens(Fig. 4-19(a)). Physical measurements were also taken using the experimental setup both with and without the lens in place. A plot of the measured received power levels at 10.9 GHz in the XY and YZ planes behind the lens (Fig. 4-19(b)) clearly shows focusing of the power to a small region centered at 75 mm from the back of the lens. The measurements in the XZ plane at $y = 75$ mm for the same frequency show both a neat focal area and power levels reaching -18 dB (Fig. 4-20(a)). When compared to power levels below -30 dB without the lens in place (Fig. 4-20(b)), the focal gain of 13dB observed here is much higher than previous metamaterial lenses. This high gain can be attributed to both the enhanced intensity expected for NRI plano-concave lenses, and the inherent low loss of the self-supporting metamaterial design. The focal region

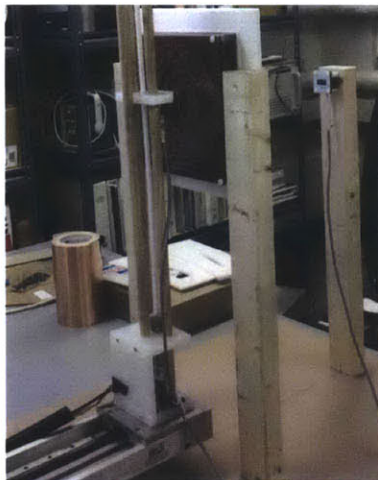


Figure 4-18: A picture of the experimental setup to evaluate the performance of the planoconcave lens.

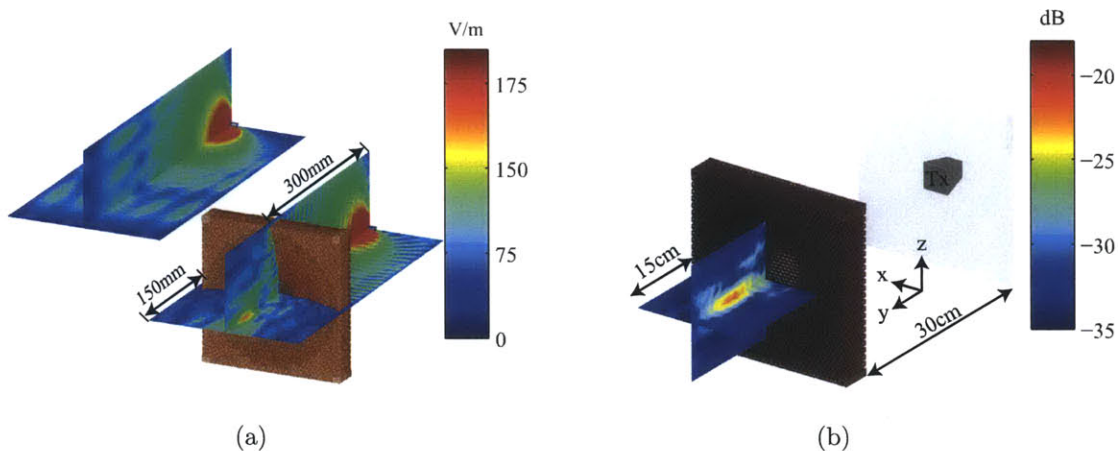


Figure 4-19: The experimental setup with simulated and measured values. (a) The simulated E-Field magnitude with and without the lens at 10.9 GHz shows elevated field levels behind the lens. (b) The experimentally measured power also indicates a focal region approximately 75 mm behind the lens.

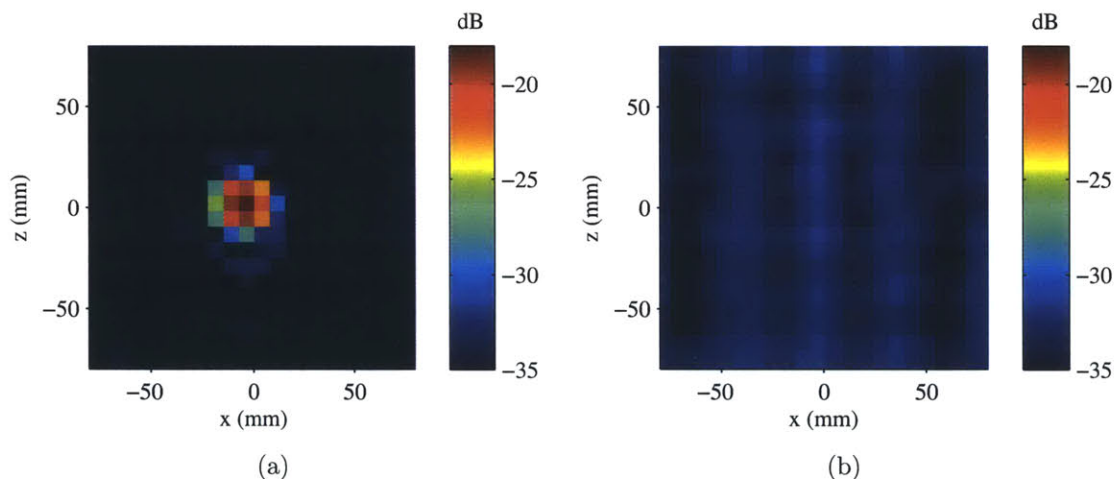


Figure 4-20: The received power measured on the focal plane $y = 75$ mm at 10.9 GHz both (a) with and (b) without the lens in place.

observed in the measurements appears to have a 3 dB spot width in the X and Z directions of less than 7.5 mm. That estimate is limited by the measurement aperture and step size, and could become significantly smaller with more dense sampling in the focal region. While the focal region is centered on the Y-axis as expected, asymmetry in the focal fields is apparent from the measurements, presumably due to reflections from the environment and tolerances in the test setup and fabrication. While the highest received power measured in this experiment was at 10.9 GHz, the focusing effect and gain of the lens was not limited to a

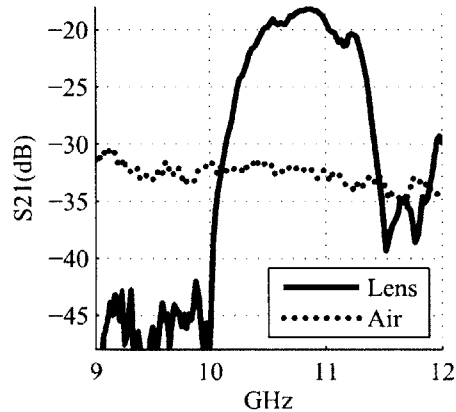


Figure 4-21: The measured received power at $y = 75$ mm on the y -axis with the lens in place is much higher than without the lens within a large swath of the NRI band of the S-ring.

single frequency but evident throughout the entire NRI band of the S-ring (Fig. 4-21), where heightened intensity levels were recorded. A mapping of the measurements along the y -axis shows there are distinct focal regions at each frequency (Fig. 4-22). These areas of high intensity move away from the lens as the frequency rises. This is due to the frequency dependent refractive index of the S-ring unit cell. The trend correlates well with the expected chromatic shift in focal distance of a homogeneous lens of similar geometry and material properties. Below 10 GHz there is no focusing despite the negative refractive index because the imaginary part of the refractive index is too high. The lens approximation seems to break down as the frequency approaches 12 GHz, where the refractive index is a very small negative number, corresponding to the region of extraordinary transmission. Though the focal position measurements match fairly well the calculations based on the refractive index retrieved from simulations, deviations of the measured results could be the result of a number of factors including the metamaterial layer discretization, and variations in the distance between individual layers of the assembled lens. Bowing or bending of the layers away from one another changes the overall unit cell thickness which can raise the refractive index at each frequency in the NRI band, moving the focus further away from the lens or vice versa.

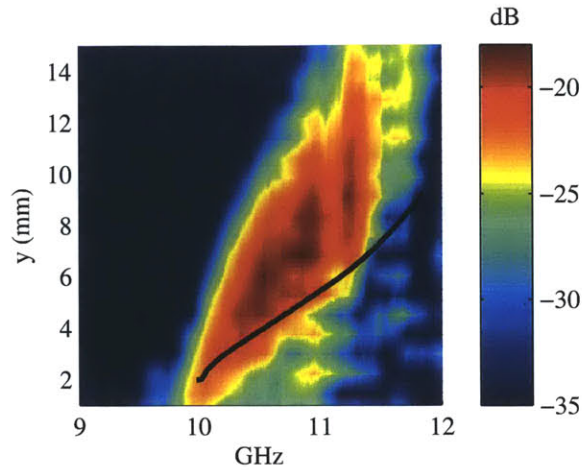


Figure 4-22: The measured power along the y -axis. The line represents the calculated focal length of a theoretical thin lens with the same plano-concave curvature and frequency dependent refractive index.

4.4 Conclusion

In this chapter I introduced the use of additive manufacturing processes to fabricate arrays of 3D metamaterial unit cells. As opposed to other fabrication techniques, which are limited to planar realizations and often require significant manual labor to construct 3D devices, additive manufacturing has the flexibility to build complex 3D metamaterial geometries and can streamline the fabrication process. To exemplify the utility of this technology, I constructed a NRI plano-concave lens made from arrays of S-rings, a metamaterial unit cell that is both self-supporting and low loss. The fabricated S-rings were measured to have minimal transmission losses, and the focal intensity of the assembled metamaterial lens was found to be significantly higher than reported for similar metamaterial lenses.

Chapter 5

Conformable Coverage and Orthomorphic Radiance

In the previous two chapters, I showed that additively manufactured parts make useful substrates to support the conductive material required to generate artificial reflection and enhanced transmission. In addition to that supportive role, the geometric flexibility of additive manufacturing lends itself to another function within the fabrication of electronic devices, the process of patterning. Surface patterning is often an essential step in both PCB and micro fabrication, but like most aspects of those processes, current methods are limited in non-planar situations. In this chapter, I introduce a new fabrication process called Conformal Masking, which is useful for the patterning of non-planar electromagnetic structures and devices. I begin by motivating the need for non-planar patterning and a discussion of current non-planar patterning methods. That is followed by a presentation of two applications of patterning via conformal masking: the fabrication of a conformal frequency selective surface (FSS), and the optimization of a conformal patch antenna array.

5.1 Introduction

Analytical solutions and finite element simulations are useful tools that enable electromagnetic designers to cogitate and optimize new ideas before investing resources on physical prototypes. While full flexibility is available during these initial design stages given the va-

lidity of Maxwell’s equations in all dimensions, the design space itself is often constricted by practical limitations stemming from available time, space, materials, and fabrication equipment capabilities. Fabrication limitations are especially pronounced in designs that call for complex non-planar geometries.

As discussed in earlier chapters, fabrication for electromagnetics by necessity requires a controlled architecture that is a conglomeration of materials with a variety of electromagnetic properties. The most common example of this involves dielectric substrates patterned with a layer of conductive material. When feature sizes allow, PCB processing is the prototyping method of choice, combining material removal through machining and etching with material addition by printing and plating. Often smaller feature sizes are required for higher frequency metamaterials or micro-antennas. In these cases, semiconductor and MEMS fabrication techniques developed for the production of CMOS circuits, sensors and other miniaturized devices are used.

With available fabrication methods focused primary on planar designs, two separate approaches have been taken to solve the problem of creating non-planar electromagnetic structures. The first strategy is to build three-dimensional designs from multiple layers of PCBs or silicon wafers. When required, but often with great difficulty, layers can be diced, spliced and reassembled to increase the dimensionality and complexity for the desired application. This “pattern first-assemble” later approach has been applied to situations beyond simply stacking planar substrates together, such as conforming flat but flexible films to curved surfaces. While straightforward for applying films with planar patterns to singly curved geometries such as cylinders, this has also been used for more complex surfaces such as spheres, by patterning the original film in such way that cut outs conform the curved surface with minimal overlaps and strain [82]. Another example of out-of-plane thinking along this vein is the micro self-assembly of out of plane metamaterial and circuit structures that has been achieved through the clever manipulation of internal stresses in conventionally patterned thin films [83, 84]. This approach, taken to its theoretical limits, is extremely powerful, as it was recently shown that one-dimensional structure can be folded into almost any 3D shape [85], similar to the way 1D chromosome strands form complex globules which enable genes at different locations to work together in close proximity [86].

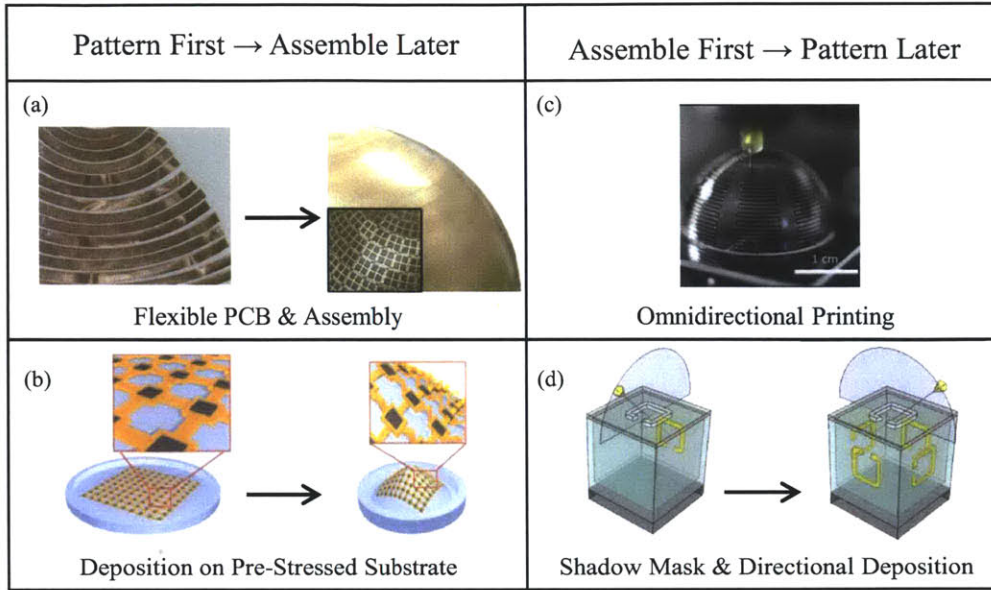


Figure 5-1: Pattern first techniques exemplified by (a) flexible PCB films cut in such a way to fit conformally on spherical surface [82] and (b) pre-stressed substrates that return to their non-planar states after deposition [87]. Assemble first-pattern later includes (c) omnidirectional printing on spherical substrates [88] and (d) directional deposition through planar shadow masks [66].

Other techniques that have been developed to enable the patterning of non-planar surfaces beyond the reach of typical fabrication methods take an “assemble first-pattern later” approach, attempting to conformally pattern surfaces that are already non-planar. On the microfabrication level, this can be accomplished with photoresist methods that utilize spray coating and electrodeposition instead of the standard spin coating, which often fails to properly distribute itself on non-planar surfaces. These resists have allowed conformal conductive traces to be placed on micromachined features up to 400 microns deep [89]. Soft lithography pattern transfer has also proven useful for patterning cylindrically curved surfaces [90]. Another process that follows “assemble first- pattern later” is omnidirectional printing, which uses a stylus on a robotic arm to precisely trace lines on the surface of non-planar substrates. These pens are filled with metal-based conductive inks and used to draw meander line antenna features both in and out of plane on flexible, stretchable, and curvilinear surfaces [88]. While the conductivity of these ink traces is below that of conductive traces formed by other methods, performance losses due to the added resistance are often offset by the ef-

iciency of conformally drawn interfacing connections. Despite these advances, non-planar electromagnetic designs can make for involved projects largely because of limitations associated with fabrication. To address these difficulties, the remainder of this chapter introduces Conformal Masking, a fabrication method which allows for direct conformal patterning on non-planar surfaces. After a description of the fabrication method, the utility of this process is demonstrated through the fabrication of a conformal FSS and patch antenna array.

5.2 Conformal Masking

5.2.1 Other Masking Methods

Masks are an important part of electromagnetic device fabrication, and come in two common forms, photoresist masks and shadow masks. Spin coating and other methods are used to apply photoresist masks to planar surfaces, where they conform seamlessly and allow for sub-micron dimensional control during subsequent exposure and etching steps. Exposure is done using either contact lithography, or projection lithography, both of which have limitations on resolution, but the end result is always a mask fully flush with the substrate surface.

Shadow masks, which amount to stencils by a different name, are another type of mask used to pattern surfaces. While shadow masks benefit from recyclability and can remove several bake-expose-etch steps from a process plan, resolution is typically inferior to that of photoresist masks. Though shadow masks are usually planar layers resting on planar substrates, they are rarely smooth enough to allow for intimate contact with the substrate, leaving gaps through which particles can travel and distort the desired pattern. Despite this lack of intimate contact, shadow masks can be effective in situations where the deposited material is incident on the substrate without a significant velocity component in the direction parallel to the substrate surface. In such a case, the lack of contact won't cause a significant deviation from the mask profile.

While both shadow and photoresist masks are useful for patterning planar substrates, they can be difficult to apply directly to non-planar situations. The combination of photopolymer application, masking, exposure and etching is a significant challenge on non-planar surfaces.

The solution of patterning flexible planar surfaces before applying them to curved surfaces is one that is also fraught with challenges, such as stretching or folding of the underlying substrate, and strain induced cracking or delaminating of deposited patterns.

One step toward a practical solution may be found in the combination of directional deposition and shadow masks. In principle, a perfectly collimated beam of particles incident on a non-planar surface with a properly designed shadow mask interposed would allow for the arbitrary patterning of any surface with a differentiable profile. In practice, however, this method is limited by the fact that fully collimated particle sources are not readily available. While a mask itself could be used to collimate an incoming spread of particles, it would require a significant amount of thickness.

5.2.2 A Non-Conformist Solution

Conformal masking is method of patterning that relies on fully conformal shadow masks to enable the precise patterning of non-planar surfaces without fully collimated particle sources. Enabled by advances in additive manufacturing technology and computer aided design, masks conformal to arbitrarily shaped surfaces can be rapidly fabricated and placed directly onto target substrates. By using the mask to directly pattern the substrate, this method avoids the issues of folding, cracking and delaminating that plague planar patterns forced onto curved surfaces.

The process begins with a model of the desired surface to be patterned. This surface can be generated using graphical modeling software or in the case of an existing surface, 3D scanning can be used to accurately generate a surface model. Once the surface model is built, another graphical object that conformally fits over the substrate surface is modeled, and patterned with the negative of the pattern to be deposited. At this point, additive manufacturing technology is used to build the mask and if needed the substrate to be patterned, layer by layer. This layer by layer approach gives additive manufacturing the flexibility to fabricate a mask with a surface that is a near exact replica of the substrate surface, allowing the mask to conformally come to rest on the non-planar substrate and facilitate a proper deposition.

In the remainder of this chapter, I demonstrate some of the capabilities of conformal

masking, and highlight unique features, challenges and limitations that have been encountered while employing the technology including:

- **Islands:** The design and fabrication of conformal masks enables the seamless incorporation of islands that support closed contour features. Conventional shadow masks cannot support islands, as bridges would interfere with the deposited pattern. Since conformal masks begin as 3D models and are fabricated using additive manufacturing technology, elevated bridges can be fashioned to hold islands in place, designed in such a way as to not impeded the deposition of the full pattern.
- **Thermal Issues:** Many additive manufacturing processes use polymers with low glass transition temperatures as the model material, which can cause problems for masks used with deposition methods that involve elevated temperatures.
- **Conformal Contact Issues:** While masks are designed to fit conformally, the resolution of the mask fabrication method limits the ability of the mask to perfectly match the substrate profile. Without countermeasures, this can lead to an unfaithful pattern transfer. Potential solutions include the use of directional processes to minimize particles capable of depositing under the conformal mask, or methods to improve the overall conformality of the mask, such as adhesives or independently compliant pre-stressed stencil elements that press themselves into the substrate to form a tight seal.

5.3 Conformal FSS

5.3.1 FSS Applications

An FSS is a surface that acts as a filter for electromagnetic waves realized by patterning a surface with an array of metallic structures. Depending on the design, these surfaces can act as band stop or band pass filters. The application of FSS technology is focused primarily on antenna radomes, which are dielectric coverings for antennas that provide protection from the elements [91]. By patterning the surface of a radome with an FSS, signals entering or leaving the radome can be filtered. This filtering ability can be useful for reducing the

intensity of signals at particular frequencies which could interfere with radio observatory observations, or overload infantry or vehicular based electronics during a hostile electromagnetic pulse attack [92].

While demonstration of a surface's filtering characteristics is straightforward with PCB prototypes under plane wave incidence, both FSS design and fabrication for three dimensional antenna systems such as spherical radomes that surround curved reflectors is significantly more difficult [93]. Even from the design perspective, planar arrays are much simpler to analyze. A planar array configuration of planar FSS elements facilitates the use of periodic boundary conditions that can simplify both analytical formulations and finite elements simulations used for FSS characterization. In contrast, non-planar array configurations of non-planar elements lack these periodic simplifications making analytic solutions irretrievable, and requiring full scale simulations to examine electromagnetic behavior. Experimental evaluations of non-planar arrays are further complicated by the complexity associated with conformal FSS prototype fabrication.

5.3.2 State of the Art FSS Fabrication

State of the art fabrication methods for non-planar FSS geometries include the tiling of flat substrates, the application of flexible substrates, and omnidirectional printing. The tiling option, while simplest from a fabrication perspective, is known to generate radar artifacts that are not ideal [94]. The flexible substrate option amounts to FSS deposition on planar but flexible films such as polyamide or parylene [95], which can be patterned conventionally before being placed on curved surfaces. These too are susceptible to folds, bends and tears when applied to spherically curved surfaces, causing artifacts which can negatively affect performance. Omnidirectional printing is an option that is currently employed for the task of drawing non-planar FSS structures, but it is limited by the serial nature of the process and its reliance on expensive metallic inks and their inferior electrical properties [96]. Direct conformal patterning would seem ideal, but is precluded by conventional masking limitations where prevailing patterning procedures are specific to planar surfaces. The development of conformal masking, unencumbered by non-planar surfaces, makes conformal patterning possible and can streamline the fabrication process for curved FSS surfaces.

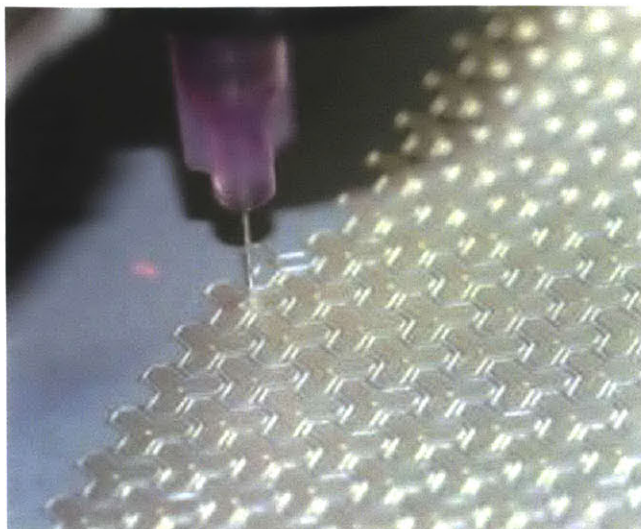


Figure 5-2: An image of an omnidirectional printer drawing FSS elements on a curved surface [97].

5.3.3 FSS Unit Cell Design

The array component chosen for the conformal FSS pattern was a hollowed out cross loop configuration, one that would be difficult to pattern on a non-planar surface without the use of a conformal mask. For the cross loop unit cell with dimensions found in Fig. 5-3, HFSS simulations were performed to first study the response of a periodic planar array of these cells to an incident electromagnetic wave. The simulation environment included one copper cross loop, a 1 mm thick substrate of $\epsilon = 4.4$, and a unit cell periodicity of 14 mm represented by the inclusion of periodic boundary conditions. The results of the simulation confirmed this geometry acts as a bandstop filter centered at 13.3 GHz with a bandwidth of about 1 GHz (Fig. 5-4). The cell response is polarization-independent due to the loop's geometrical symmetry. This and other stop bands that exist for this structure can be shifted up or down the frequency spectrum by shortening or lengthening the feature dimensions, unit cell periodicity, or changing the substrate dielectric.

The behavior of the FSS shown in Fig. 5-4 is only valid for normal incidence and an infinite array. The behavior is not as smoothly defined in the case of a finite planar FSS array and waves incident at different angles. This can be seen from simulations conducted for a finite 5×5 array of cross loops, consisting of the cross loop FSS array and substrate

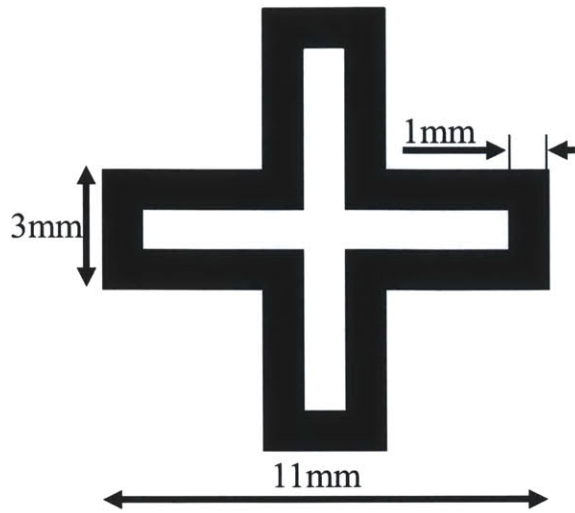


Figure 5-3: The cross unit cell.

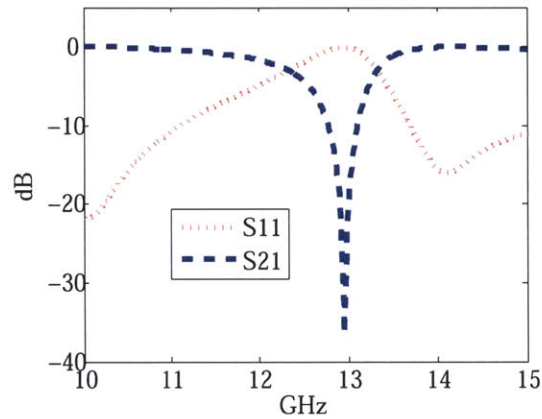


Figure 5-4: The simulated S_{11} and S_{21} response of the cross unit cell.

situated in free space interposed between two X-Band waveguide ports that were separated by a distance of 20 cm. Transmission results show that while the bulk of the filtering activity remained at 13.3 GHz for this finite configuration, there were artifacts present as a result of boundary effects and the angle of incident radiation (Fig. 5-5).

5.3.4 Conformal FSS Design

To enable the fabrication and investigation of the performance of a non-planar FSS, using 3D modeling software the finite array of crosses was projected onto a paraboloid substrate

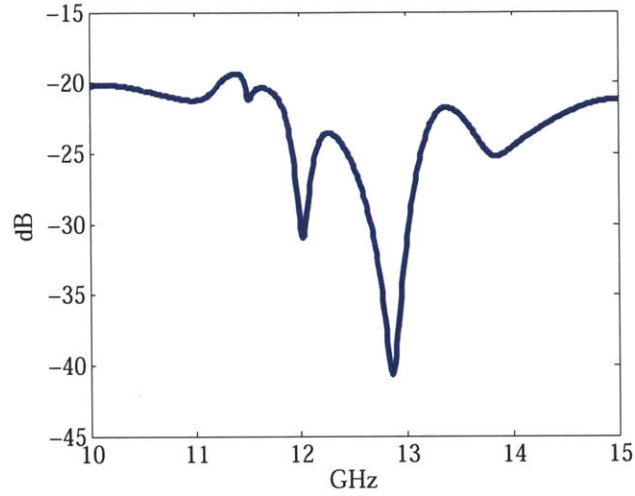


Figure 5-5: Simulated S_{21} for a 5x5 FSS array between two X-Band waveguide ports.

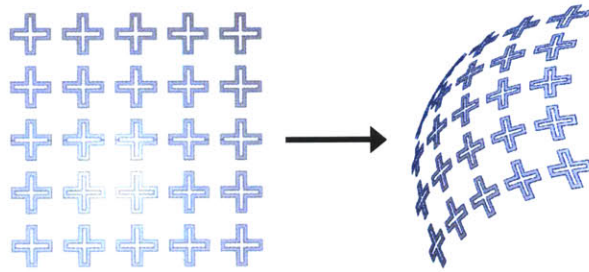


Figure 5-6: The planar FSS elements when conformed to the surface of Eq. 5.1.

with a surface defined by:

$$z = (x/10)^2 + (y/10)^2 \quad (5.1)$$

with z along the central axis of the paraboloid ranging from 0 mm to 25 mm, corresponding to a maximum diameter of 100 mm. Through several extrusion and binary operations, a model of the conformal elements was created that could be used for simulation purposes and for the design of a conformal mask (Fig. 5-6). The curved substrate upon which the elements rested for both simulations and experiments was modeled with a thickness of 1 mm, ensured by extruding the curve of Eq. 5.1 in the direction of the surface normal (Fig. 5-7).

It should be noted that as a result of the surface curvature and simple projection method employed to pattern the paraboloid, the actual dimensions of the cross loop features and

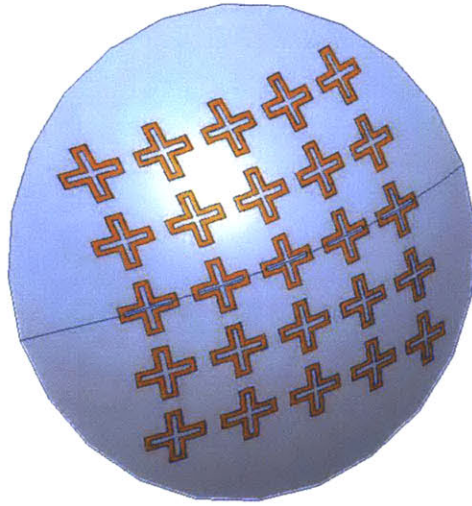


Figure 5-7: A computer model of the paraboloid dome with FSS elements on the surface.

the distance between each cell are slightly enlarged. Since the main focus of this work is the fabrication method for the FSS, this projection side effect is not studied in detail. However, it is interesting to note that if a substrate surface is well defined mathematically, there are straightforward methods for altering the planar design before projection so as to arrive at conformal dimensions on the actual substrate that meet certain criteria, such as all elements being the same length, having the same surface area or preserving the geodesic or absolute distance between cells.

5.3.5 Conformal FSS Fabrication

To fabricate the conformal FSS, a conformal mask was designed to enable the direct deposit of the array pattern on the parabolic dome surface. The mask's lower surface was designed to conformally cover the paraboloid surface to be patterned by using Eq. 5.1. To be sure the mask would fit over the dome and have a finite thickness so it could be handled, the mask's lower surface was thickened in the direction normal to the convex surface of the paraboloid. To pattern the mask layer, a model of the planar FSS array was projected through the mask, and the intersection of the two was subtracted, leaving the mask with a negative of the FSS pattern. At this point in the design process, the one layer mask would be complete for simpler unit cells featuring only open contours. However, because the cross loops are closed

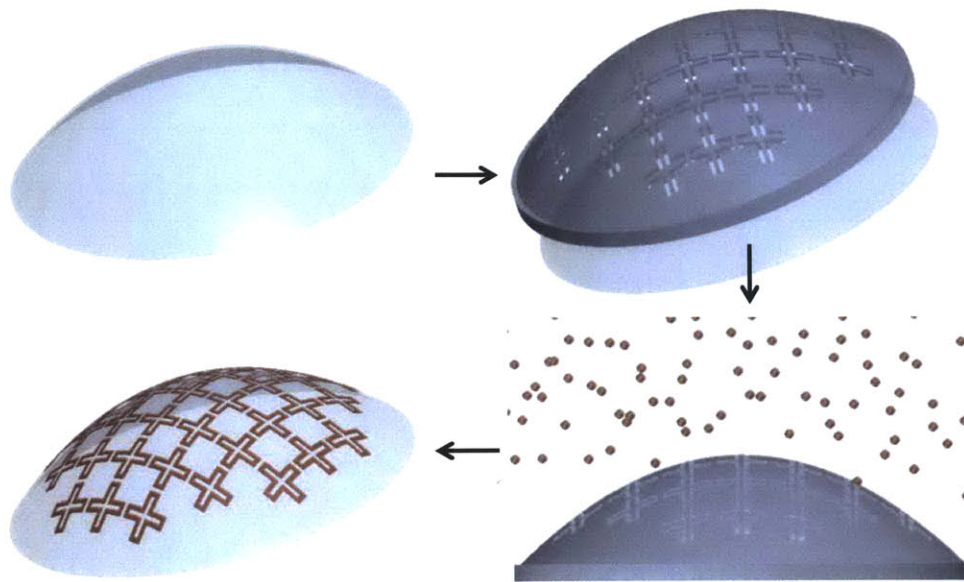


Figure 5-8: The fabrication process for a conformal FSS begins with an (top left) unpatterned dome which covered by a (top right) conformal mask. The two are then placed in a deposition chamber (bottom right) where metal particles deposit themselves on the dome through the holes in the mask, (bottom left) patterning its surface.

contours, at this stage the mask consists of many disjoint sections. To ensure the mask is one piece and can be handled and placed without difficulty, another layer was added to the mask with bridges that connect any floating islands to the body of the mask allowing it to retain its shape and dimensions during future process steps. The bridges could not be included in the original mask layer, as they would prevent deposition where the bridges are flush with the underlying substrate. In order to offset the mask bridges from the surface of the paraboloid and allow material deposition underneath, the bridge layer was placed atop the thickness of the first mask layer, which in this case was set to 3 mm. Since the bridges serve only as support for the pattern's islands, the bridge layer thickness was limited to 1 mm and the width of each bridge was only 0.5 mm. Both the offset from the surface and low surface area reduce the bridge shadowing effect, facilitating the deposition of complete cross features on the curvilinear surface(Fig. 5-9). Several copies of the paraboloid surface to be patterned and its mask were fabricated simultaneously by an Objet Connex 500 using VeroWhite, a UV curable resin that hardens into a stiff material. After the parts were printed, support material was removed by hand and with the aid of pressurized water. Once clean, the mask

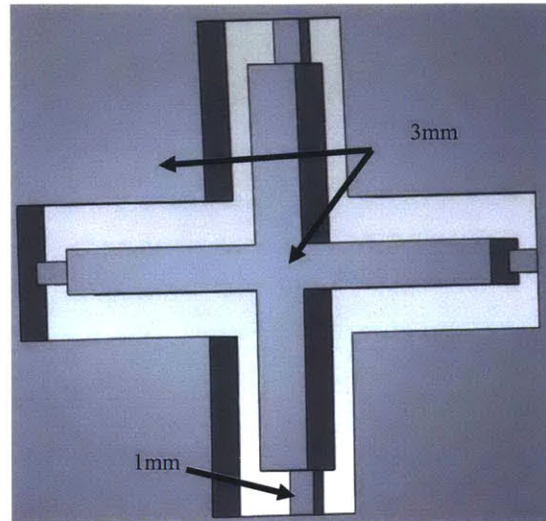


Figure 5-9: A close look at the underside of an island area of the mask. The island itself is the same thickness as the rest of the mask, 3mm, but the bridges that secure it to the mask are only 1mm thick to ensure particles to deposit underneath and complete the cross.

was placed atop the parabolic substrate, and the two were placed together in a deposition chamber (Fig. 5-8).

To deposit conductive material for the FSS pattern, I tried two deposition methods, electron beam evaporation and sputtering. The E-beam operates by focusing a stream of high energy electrons that strike a copper source inside a large vacuum chamber. As the source absorbs the incoming energy, it melts and begins to evaporate. The released copper particles stream upward, embedding themselves into any surface in their path. The sputtering tool, in contrast, operates by ionized Argon plasma knocking off atoms from a target material, in this case copper, which are rapidly ejected from the target to deposit on the substrate surface. The system was configured to sputter down, with the substrate resting on a rotating chuck in the middle of the chamber.

Many complications arose during the deposition which affected the transfer of the conformal FSS pattern to the substrate surface:

- **Thermal Management:** The single most complicating factor during deposition was heat transfer from the depositing particles to the conformal mask and substrate. Normal avenues to remove excess heat were unavailable in this particular circumstance as convective heat transfer was limited by the low pressures within the deposition chambers

and conductive heat transfer was curtailed by the non-planar substrate failing to conform to the support surface within either deposition tool. Coupled with the low thermal diffusivity of the polymer, a rise in the temperature of the polymer mask and substrate was inevitable. Prolonged exposures to depositing particles could raise temperatures beyond the polymer's glass transition temperature, and in the extreme case beyond the melting point. To avoid the catastrophic failures that comes with such a loss of structural integrity, strategies to prevent melting include both faster deposition rates and shorter deposition times, followed by quick reentry to an environment conducive to convective cooling.

- Fixturing: Thermal issues made fixturing slightly more complicated in the case of E-beam evaporation, where the substrate and mask are face down during the deposition. For typical substrates, such as glass or silicon wafers, a few pins on the substrate edge are enough to counter the force of gravity. In the case of the polymer mask and substrate, localized stresses caused by pins result in substrate warping as the yield point of the polymer shifts at elevated temperatures. Instead of pins, I used strips of polyamide tape to reduce stress by distributing the force over a larger area, resulting in reduced warpage. Sputtering did not have a fixturing issue, as the chamber was designed for downward sputtering, and the underlying chuck provided sufficient substrate support.
- Deposition Directionality: One of the main differences between the two processes I used was the directionality of the deposition, which was found to have a significant affect the quality of the deposited pattern.
 - Bridge Shadowing: The extent of shadowing caused by bridges depends on the directionality of the deposition. Bridges built-in to the conformal mask were raised to enable metal particles to deposit underneath. A fully collimated beam of particles from a highly directional deposition would be blocked by a bridge's structure, while a less directional process reduces shadowing by enabling particles to reach the substrate surface. Of the two processes used in this case, E-beam evaporation was significantly more directional than sputtering. To reduce the effect of shadow-

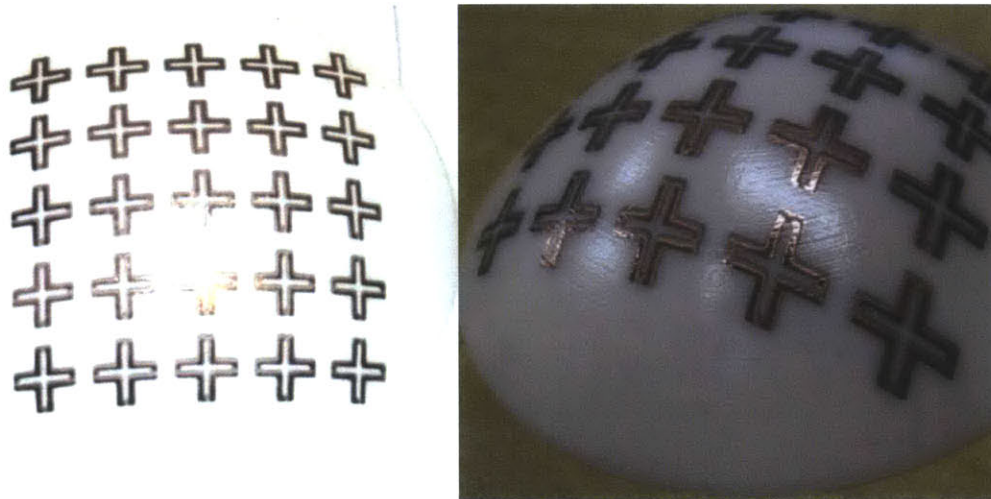


Figure 5-10: A top down and isometric view of the paraboloid dome patterned with the cross loop FSS array.

ing during somewhat directional processes, bridge footprints should be minimized and raised further from the substrate to allow more particles to reach the covered surface.

- Mask Conformality: Though conformal masks are designed to be perfectly conformal, in reality they are not always in intimate contact with the substrate at all locations. This space between the mask and substrate makes it possible for particles to deposit themselves within the gaps, if they have the correct angle of approach, and bleed out beyond the borders of the defined pattern. This is less of a problem for more directional processes, which are collimated by the mask walls. In processes which have more diverse angles of incidence, mask wall height can be raised to further collimate the particles streaming from the source, or steps can be taken to address the conformality issue itself.

After several attempts, FSS elements were faithfully transferred to a paraboloid surface using the E-beam (Fig. 5-10). The mask and substrate were secured with strips of polyamide tape (Fig. 5-12). While artifacts of shadowing were apparent on many of the unit cells, all cross loops were complete (Fig. 5-11).



Figure 5-11: Close up of some copper cross unit cells deposited on the paraboloid dome. Note the deposition at the edge of the cross arms is noticeably light because of shadowing by the raised bridge on the conformal mask.

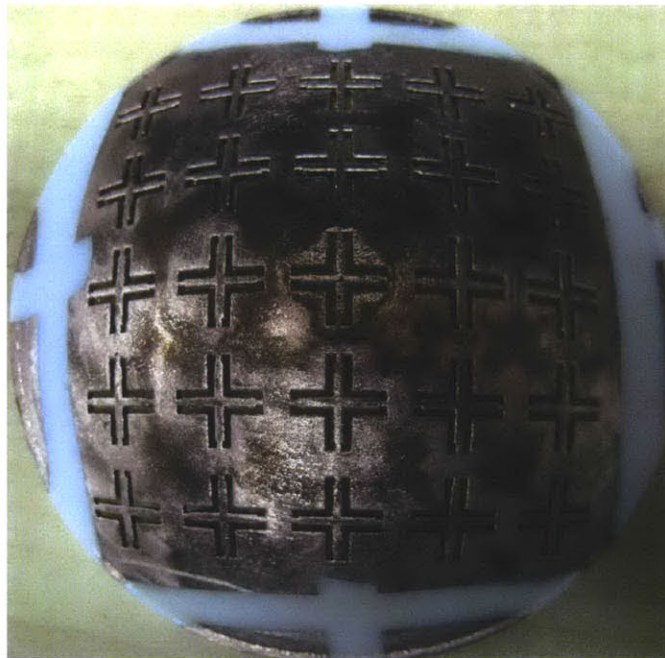


Figure 5-12: The conformal mask used to pattern the dome with the FSS array. Some parts of the mask were not coated in copper as polyamide tape was used to fixture the mask and dome substrate within the E-beam chamber.

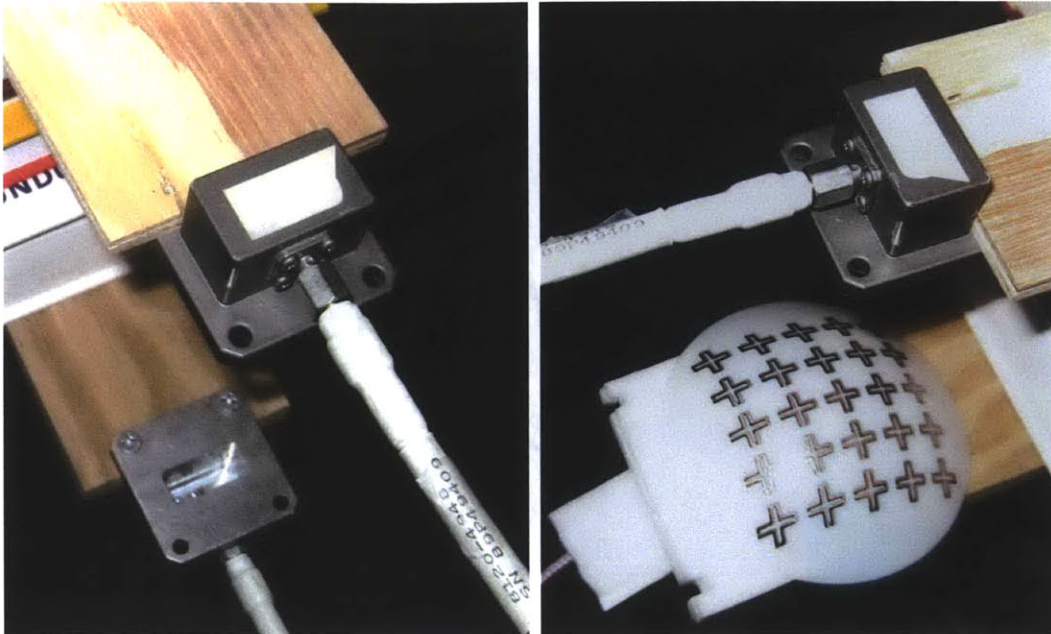


Figure 5-13: A picture of the experimental setup included with the two horns spaced 20 cm apart, with and without the conformal FSS dome covering one of the horns.

5.3.6 FSS Evaluation

An HFSS simulation to evaluate the conformal FSS arrangement was set up by placing the arrayed FSS elements atop a parabolic dome substrate as part of a single graphical model. The FSS assembly was then arranged to encapsulate one of two X-band horn antennas excited as wave port sources with the surrounding space given a radiation boundary condition. The fabricated conformal FSS screen was evaluated in a similar fashion, by placing the paraboloid FSS over one of two X-band coax-to-waveguide adapters connected to the ports of an HP8501B network analyzer (Fig. 5-13). With the waveguides set 20 cm apart, the transmitted power was recorded both with and without the FSS paraboloid in place.

The results from both the simulation and experiment show the FSS stop band does not translate from the planar array to the surface of the paraboloid, though there is a downward frequency shift (Fig. 5-14) which corresponds to the sideband visible to the left of the original stopband for the simulated flat array. This shift is attributable to two factors. First, as a result of the projection used to design the conformal mask, the FSS elements were slightly elongated by the curvature of the paraboloid surface. The degree of elongation was dependent

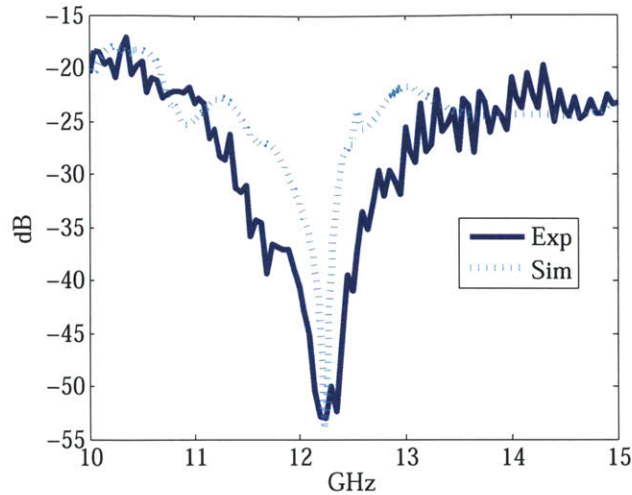


Figure 5-14: Comparison of simulation and experimental transmitted power (S_{21}).

on the distance from the center of the paraboloid. As a result of the distribution of longer FSS dimensions, the stop band is slightly lower and broader than that of the planar FSS array reported above. Additionally, the fact that waves emitted from the waveguide encounter the FSS structures at oblique angles contributes to the lower frequency stop band.

5.4 Conformal Antenna Array

Antennas are another type of electromagnetic device that are often required to be conformal to a non-planar surface. Though antennas often by design include non-planar elements, many industries including aerospace and the military are currently focusing research efforts towards the study of antennas conformal to particular geometries. In the aerospace industry, antennas such as dipoles or curved reflector dishes can pose integration issues as an irregularly shaped antenna may have deleterious effects on the carefully calculated aerodynamics of a vehicle profile. While aerodynamics are not to be ignored on ground vehicles as well, as evidenced by the stylish antennas on some of today's luxury automobiles, militaries have a more pressing issue given the fact that the large dipole or dish antennas needed for communications can significantly increase the visibility of military vehicles in a combat zone. The conspicuous profile created by recognizable military antennas can draw the attention of hostile forces and endanger the lives of service members [98].

Patch array antennas are of particular interest for conformal applications. Useful on account of their flexible radiation pattern and beam steering capabilities, array antennas are most often deployed as planar constructs. While conformal arrays exist, they are typically limited to antennas that locally conform to canonical shapes such as cylinders, or achieve segmented conformality through tiled structures. These state of the art implementations lack full conformality and are unable to perfectly place antennas on arbitrarily shaped structures. Full conformality is possible via direct writing processes, but relies on conductive ink which suffers from poor electrical characteristics.

The remainder of this section explores the use of additive manufacturing as a method to enable direct patterning of conformal antennas through the use of conformal masks. This fabrication option offers solutions that can be tailored to specific geometries on both the antenna element and array level of integration. The remainder of this section proceeds as follows. First, a non-planar substrate to be patterned with a conformal antenna is presented. Then, a planar patch antenna is designed, and analyzed in its non-planar configuration. That is followed by a comparison between the simulated performance of a planar and non-planar antenna array, and the compensation required to account for the affects of the non-planar geometry. Finally, a planar and non-planar array are fabricated and tested.

5.4.1 Non-planar Substrate

A plot of the non-planar substrate for the conformal array antenna is shown in Fig. 5-15. The substrate includes an array of four concave or convex features fitted to 2D Gaussian functions, where the height of the substrate $z(x, y)$ is defined by,

$$\sum_{n=0}^4 z = A_n e^{\frac{-(x-x_n)^2+(y-y_n)^2}{2\sigma^2}} \quad (5.2)$$

where $\sigma = 10$ mm, (x_n, y_n) are the center coordinates of the Gaussians, and the amplitude A_n is either 10 mm or -10 mm.

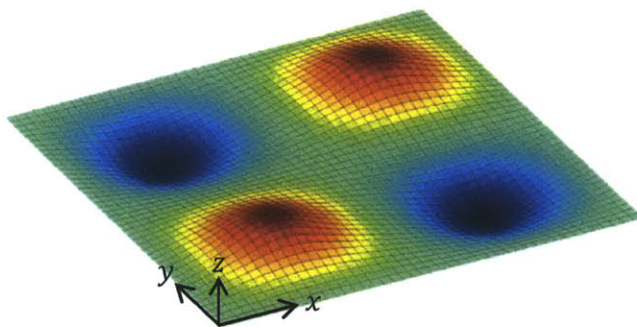


Figure 5-15: The form of the substrate used for the conformal antenna featured an array of concave and convex 2D Gaussian features.

5.4.2 Planar and Conformal Patch Antenna

Planar Patch Element

Before designing a conformal antenna array, I began with a single planar patch antenna element. Key parameters for the design of an individual patch are the shape of the patch, center frequency, substrate material and substrate thickness. For simplicity, I chose square patches and a center frequency of 4 GHz, which suited the available measurement equipment. The material used in the design was Verowhite, which was measured to have a dielectric constant of $\epsilon = 2.8$ and a loss tangent of $\delta = .02$ over the relevant frequency band. The substrate was given a thickness of 1.7 mm, which was dictated by the 50 Ω SMA connector available to feed the antenna from a signal generator. A single planar patch antenna element was modeled using HFSS, separated from a large ground plane by a material with the same properties as Verowhite (Fig. 5-16). The initial patch size was $\lambda/3$, including two insets near the feed point. The dimensions of the patch and the insets were varied to improve the impedance match of the single element. The feed line dimension of 1.21 mm was determined using a standard calculator [99] to match the feed to an impedance of 100 Ω , given the eventual need for a impedance matching network when the patch is incorporated into an array. The final planar design was a square patch with a 21.5 mm width and length and insets that were 2 mm \times 5 mm, which resulted in a return loss of $S_{11} = -40$ dB centered at 4.09 GHz and a -10 dB bandwidth of 0.14 GHz (Fig. 5-17). This antenna had a gain of 5.12 dB at 4.09 GHz and a radiation pattern as shown in Fig. 5-18.

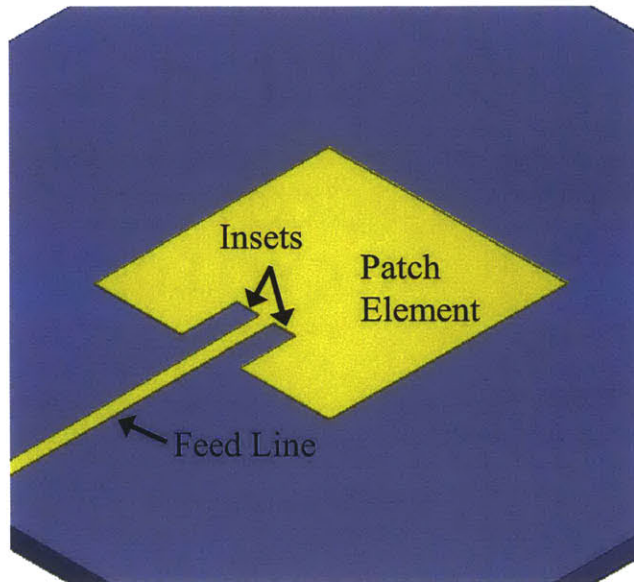


Figure 5-16: A model of the planar patch elements used to design the patch array, featuring a square patch with 21.5 mm sides, a feed line of width of 1.21 mm, corresponding to a stripline impedance of 100Ω .

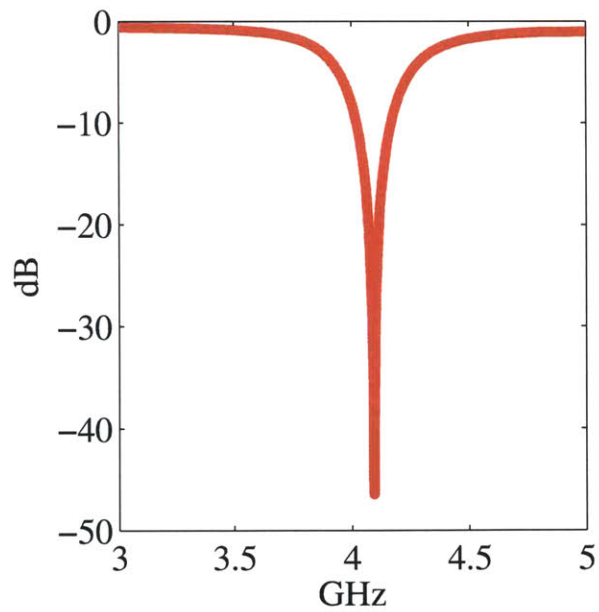


Figure 5-17: Plot of the simulated return loss (S_{11}) for the planar patch element.

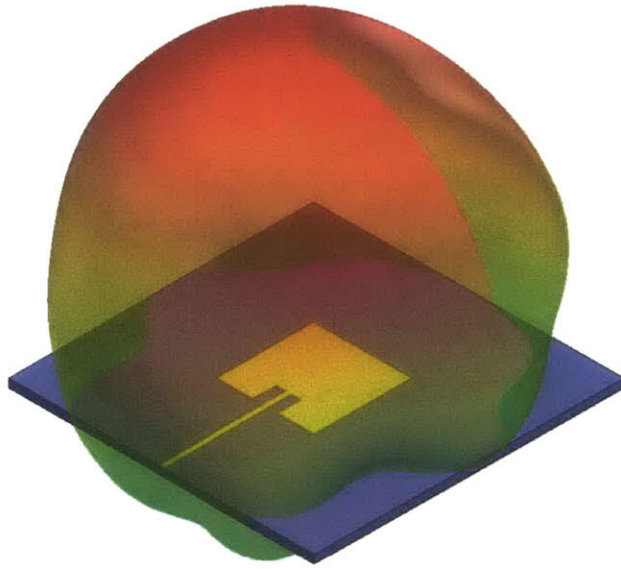


Figure 5-18: The radiation pattern of the planar patch element, which has a maximum gain of 5.12 dB.

Conformal Patch Element

To model a conformal patch antenna, the geometry of the antenna patch, substrate and ground plane were altered to represent a single Gaussian. Substrate thickness normal to the surface was a constant 1.7 mm. The patch antenna model was designed by projecting the planar antenna conformally onto the substrate surface. Simulation results of a parametric sweep of A from -10 mm to 10 mm show the return loss center frequency shifts slightly as the geometry of the element deviates from planarity (Fig. 5-19). The shift is caused by the increase in antenna surface area, which can be compensated for by slight modifications to the patch dimensions. Note the shift in center frequency is larger for the concave patch than the convex patches, possibly due to intra-patch interactions in the concave patch that are blocked by the ground plane in the convex patch. The radiation pattern of the curved patches remains unchanged, with only a 1 dB drop in gain for the concave patch, as a result of lower radiation efficiency.

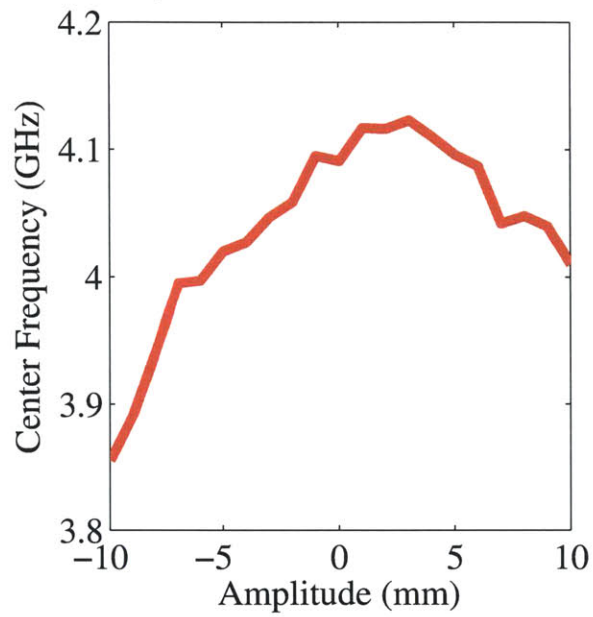


Figure 5-19: The center frequency of the antenna element's return loss shifts down from 4.09 GHz as the exponential surface amplitude deviates from planar. The frequency shift is likely due to the extension of antennas dimensions that result from the original patch shape being projected onto a non-planar surface.

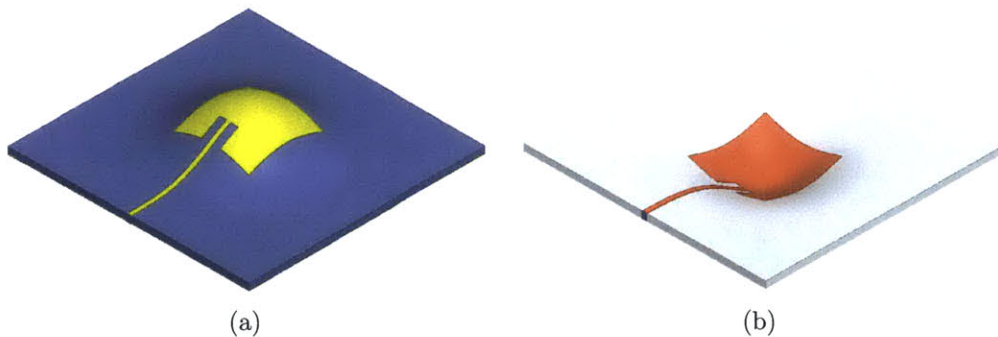


Figure 5-20: Model of a (a) convex and (b) concave patch element, corresponding to an amplitude of $A = 10$ and $A = -10$ respectively.

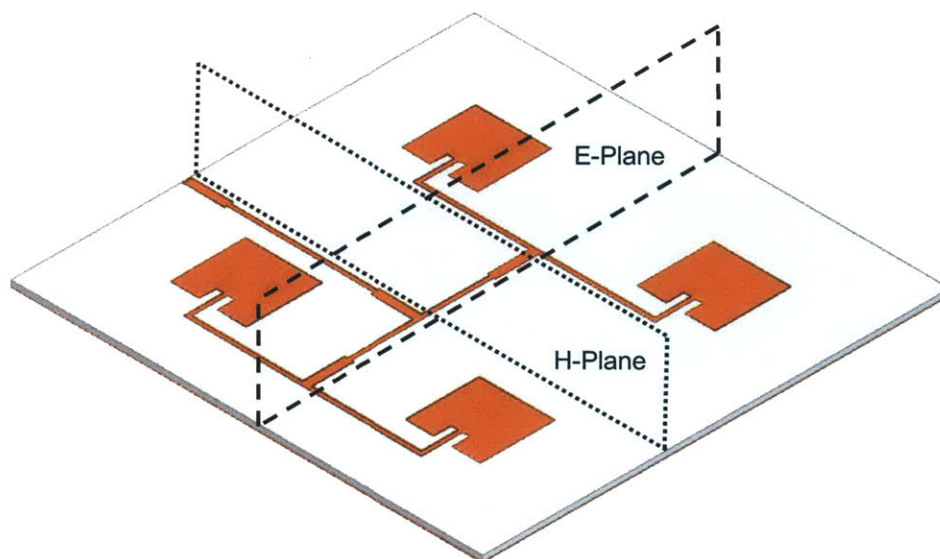


Figure 5-21: A graphical representation of the planar patch antenna array, which includes 4 square patches and a feed network. E and H-planes specified here are referenced in the measurement results.

5.4.3 Array Antenna Simulations

Planar Patch Array

After gauging the performance of individual elements, patch antenna elements were arranged in a square array formation. The planar array consisted of four planar patch elements with 21 mm between each element, arranged on a square substrate with 132 mm long sides. The space between the elements was kept below $\lambda/2$ to prevent the formation of significant sidelobes, though it was large enough to accommodate a symmetrical feed network, with each elemental feed line entering the patch from the same direction. The feed network utilized $\lambda/4$ transformer lines, with stripline widths of 4.5 mm for 50Ω segments and 2.5 mm for 100Ω segments (Fig. 5-21). The simulated return loss for the planar array showed that the four patch system had a center frequency of 4.08 GHz and a 10 dB bandwidth of 0.218 GHz (Fig. 5-22). The radiation pattern of the array was more directive than the single patch, achieving a maximum gain of 8.83 dB (Fig. 5-23).

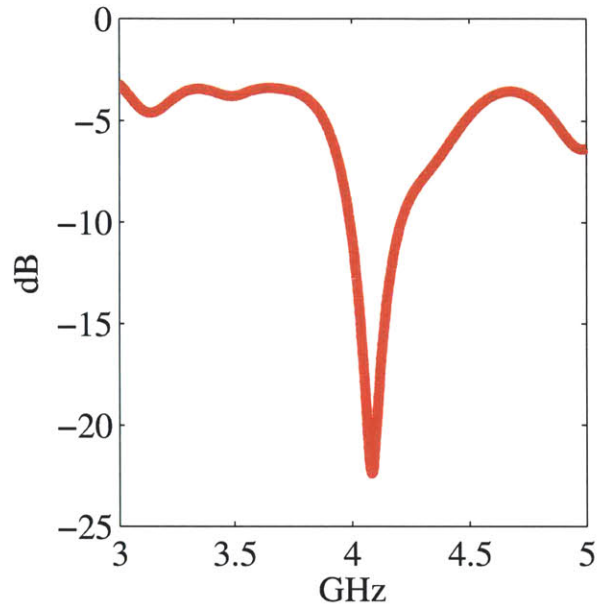


Figure 5-22: The simulated return loss of the planar patch antenna array is similar to the response of a single patch element, with the center frequency at 4.08 GHz.

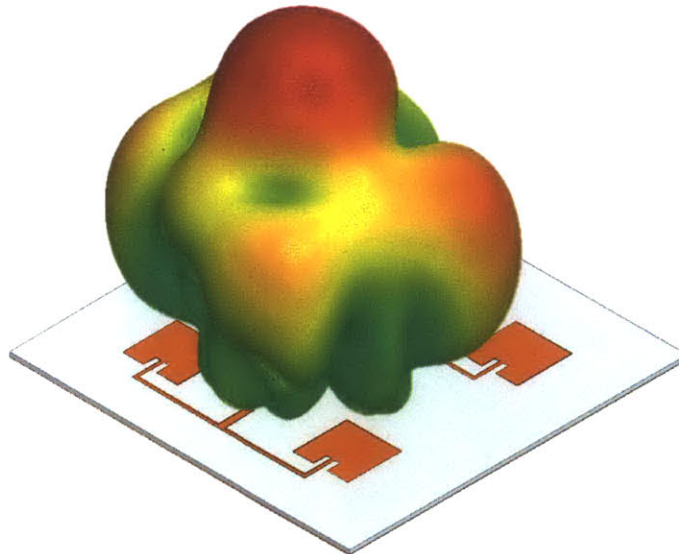


Figure 5-23: The radiation pattern from the planar patch array simulation shows a highly directive response typical of antenna arrays, with a maximum gain of almost 9 dB.

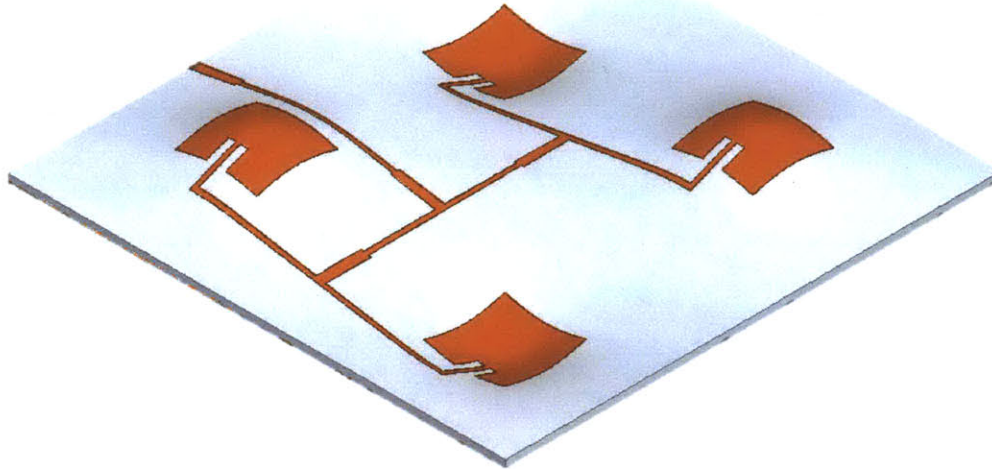


Figure 5-24: The conformal antenna array, with the patches and feedlines projected directly onto the non-planar surface.

Conformal Patch Array

The surface used for the conformal patch array was designed with concave and convex Gaussian functions centered at the position of each patch. The planar patches and feed network were projected directly onto the curved surface (Fig. 5-24) to form the conformal antenna array. Simulation results for return loss of this configuration show the change of surface topography had an impact on the return loss. The center frequency shifted to 3.94 GHz, though the S_{11} at 4 GHz was still below -10 dB (Fig. 5-25). The radiation pattern also reveals the influence of the non-planar geometry, significantly lowering the antenna array gain to a maximum of only 5.7 dB, less than 1 dB above the gain of a single patch.

To compensate for the change in topography and shift the conformal array radiation back to the directivity of the planar array, the dimensions of the concave patch elements and feedline network were modified. As shown earlier, the concave geometry caused a shift in the S_{11} minimum of the patch to 3.85 GHz. Slightly lowering the patch element size by 0.5 mm to 21 mm shifted the center frequency back to towards 4 GHz, equalizing the frequency characteristics of the individual patches. In addition to resizing the concave patch elements, the

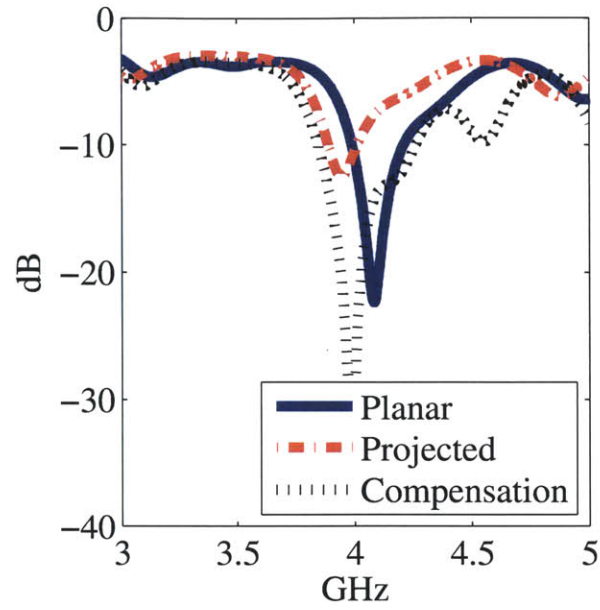


Figure 5-25: The simulated return loss of the patch antenna array on the non-planar surface with and without feedline compensation.

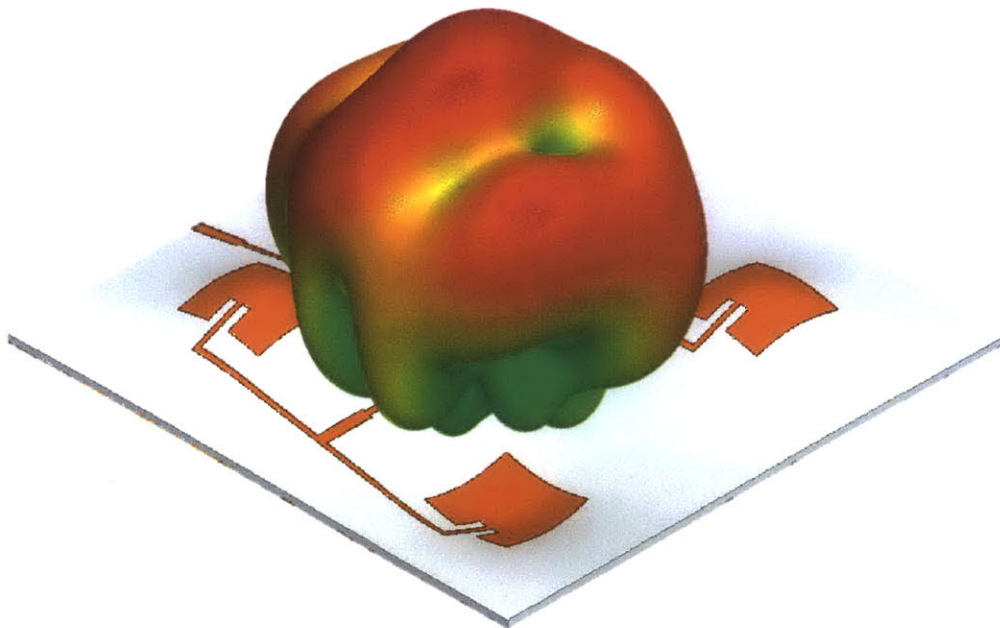


Figure 5-26: A simulation of the conformal array without compensation reveals a significant change in the shape of the radiation pattern.

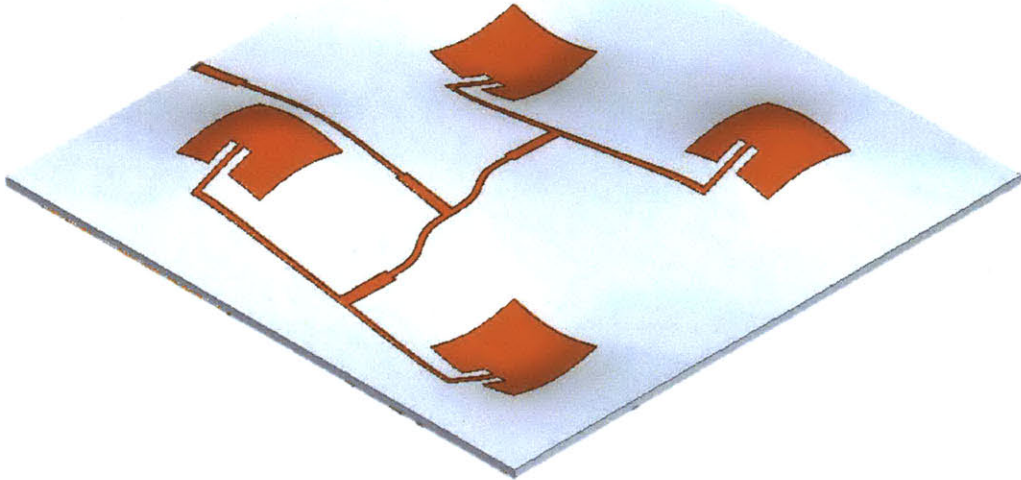


Figure 5-27: The conformal antenna array including adjustments to the concave patch size and feed network to redirect the radiation pattern.

feedline network needed to be modified to compensate for the difference in patch antenna height. Having the radiating elements either above or below the original surface of the substrate causes a phase mismatch in the radiation emitted by each antenna, disrupting the radiation pattern. To match the phase, the two nodes that split off to the actual patches were shifted by 5 mm from their central locations towards the concave patches. Other slight modifications to the feedline were included to facilitate the shifting of the node without distortion of the other lengths of the antenna feeds and reintroduce the problem(Fig. 5-27). After the aforementioned modifications, simulations showed that the compensation of 5mm toward the concave patches along with the smaller patch size both recentered the conformal array return loss to 4 GHz and restored the radiation pattern to its previous directive form(Fig. 5-28). The maximum realized gain of the pattern was 9.5 dB, slightly more than the gain of the planar array.

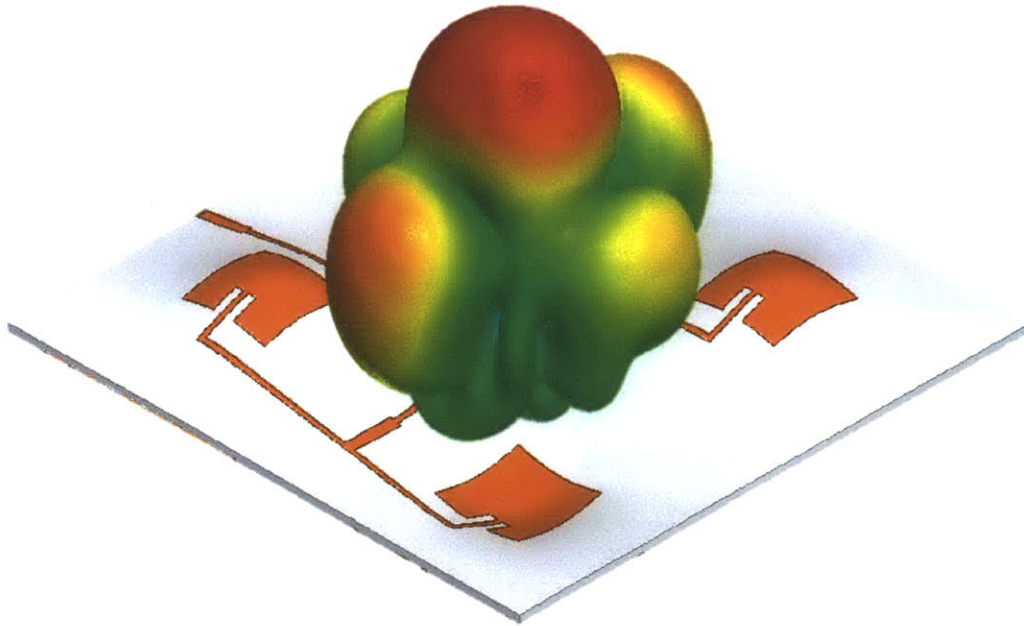


Figure 5-28: The radiation pattern of the conformal array after compensation had a directivity similar to the original planar array, and a slightly improved realized gain of $9.5dB$.

5.4.4 Fabrication

Both a planar and non-planar patch antenna array were fabricated using the method of conformal masking. From the three dimensional models used to study the behavior of both array geometries, planar and conformal masks were designed with the areas of the patches and feedlines cut out. Substrates and masks were then fabricated using the Objet Connex 500. In addition, a conformal base was fabricated upon which the non-planar substrate could rest to preserve the substrate shape during handling and coating. Both E-beam and sputtering were considered for coating of the antenna array patches. In the case of the E-beam, fixturing again proved a challenge, as polyamide tape alone was insufficient to prevent deformation caused by the combination of gravity and the heat of deposition. Bleed through during sputtering remained an issue due to the lack of intimate contact between the mask and substrate.

A single solution that addressed both of these problems was the application of an adhesive layer to the mask. The adhesive layer provided a decentralized force to keep the mask in place and retain its form while secured to the substrate and the substrate base.

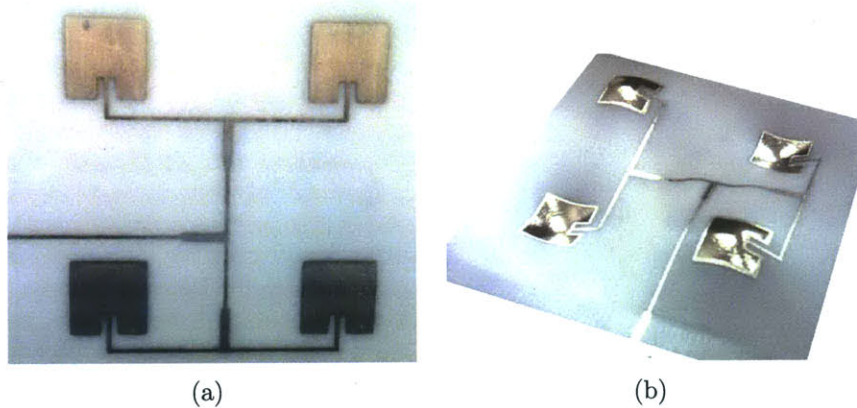


Figure 5-29: (a) A planar patch array fabricated using a planar mask patterned with copper via E-beam. Mask adhesion for this sample was provided by a thin layer of Tango+ on the underside of the mask. Thermal damage to the mask caused the mask to deform slightly near the patch insets. The loss in conformality resulted in deposition beyond the region desired by the mask. The copper film began to flake after multiple depositions. (b) A conformal substrate sitting atop the conformal base, the copper patch antenna array pattern deposited using a sputterer.

The adhesive also filled in the gaps between the mask and substrate, allowing the mask to conform more accurately. Two different adhesives were tested. The first was a standard industrial removable adhesive 3M-75. The second material was Tango+, available as part of the Connex 500 system. Thin layers of the material proved to be fairly tacky, providing a significant amount of adhesion between the mask and substrate. The combination of these two adhesion methods resulted in very strong adhesive bond, making it difficult to separate the mask from the substrate after deposition (Fig. 5-30). Despite the two precautions taken to prevent thermal damage and increase mask conformality, there were several failures before any successful depositions (Fig. 5-29). During one sputter deposition, a portion of the conformal mask warped due to residual stress, lifting several millimeters off the substrate against the pull of gravity.

Another issue that surfaced during antenna fabrication was the conductivity of the final deposited film due to the roughness of the surfaces produced by layered manufacturing. On a very flat substrate, even a micron layer of copper yields resistances below 1Ω on a standard digital ohmmeter. On a rougher surface the resistance is much higher. The patch antenna patterns deposited conformally on the substrates were measured hundreds of ohms from



Figure 5-30: Conformal masks can be fragile, unable to withstand significant strains. In this image, a conformal mask broken while trying to remove it from the substrate. This mask included both a layer of Tango+ and a removable spray adhesive. The two together require a significant amount of force to separate the mask and substrate, resulting in mask damage.

patch to patch after several microns of deposition, implying that a thicker metallic coat may be required when depositing on rough surfaces. Thicker metal deposition is one option to lower the resistance, though they can result in films with elevated levels of residual stress that lead to peeling, as well as increased thermal damage (Fig. 5-29). Another option for thicker metallic layers is electroplating atop a deposited seed layer. This method is able to produce very thick films without residual stress or thermal problems.

5.4.5 Antenna Array Testing

A fabricated planar and compensated conformal patch antenna array were tested in an anechoic chamber at AFRL, Wright Patterson AFB Ohio. Cross-sections of the measured radiation patterns are shown in Fig. 5-31. For reference, the measured gain of the planar array shows a good fit for the main lobe, sidelobe level and null positions of the simulated results for the planar antenna array. Measurements of the compensated conformal array came in with maximum gain higher than the planar array gain, as predicted by the array simulations, and almost 5 dB above the gain of the uncompensated patch antenna array. While the plot of the E-plane for the conformal array shows sidelobe levels and nulls that

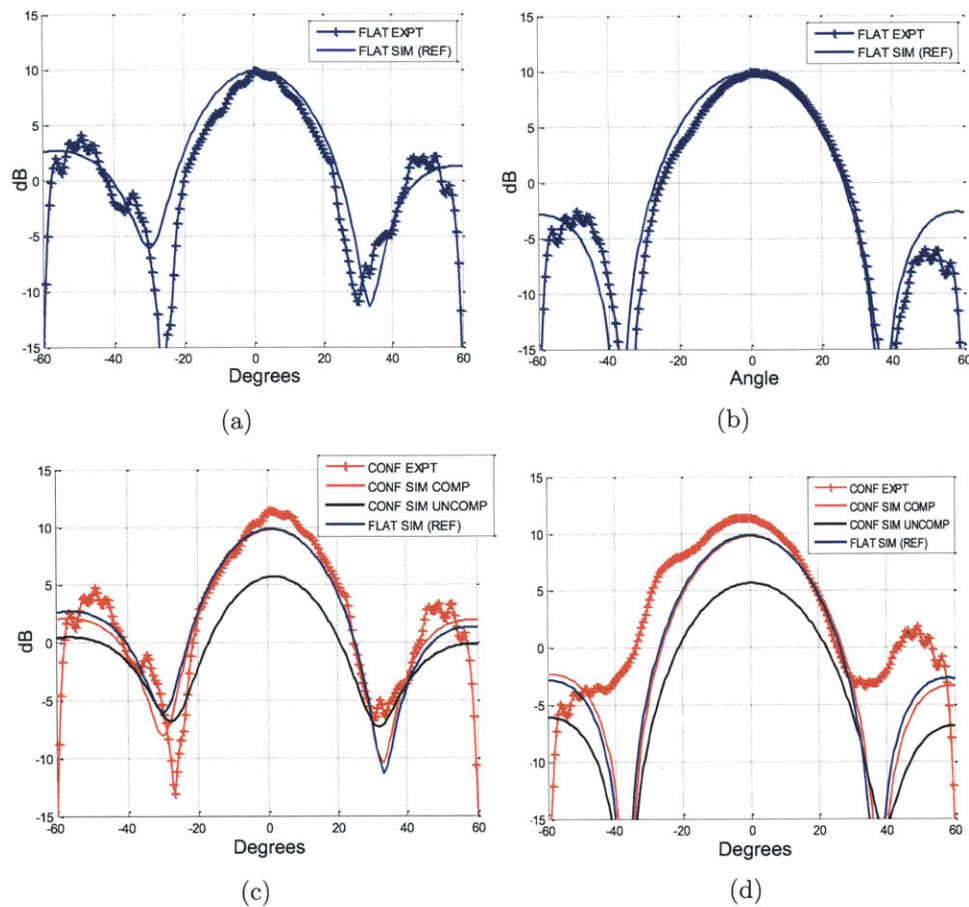


Figure 5-31: The measured radiation pattern of the ((a) & (b)) planar antenna array agrees well with the radiation pattern from simulations. ((c) & (d))The pattern of the conformal patch antenna shows increased gain as per the simulation results, but also elevated sidelobe levels in the H-plane.

match simulations well, measurements in the H plane show elevated sidelobes slightly higher than the simulated values, the source of which may have been modeling, measurement or fabrication errors.

5.5 Conclusion

In this chapter I introduced Conformal Masking, a method that enables the patterning of non-planar surfaces and objects. Leveraging the flexibility of additive manufacturing techniques such as 3D printing to replicate the curvilinear features of an arbitrary substrate, conformal masks can be used to fabricate conformal electronics without the need for flexible substrates

or the limitations of conductive inks. Two examples of conformal masking were demonstrated by an FSS array and patch antenna array.

The conformal FSS featured a paraboloid surface which was patterned with an array of cross loop elements. As a closed contour, the cross loop element would have been difficult to fabricate without the use of an additively manufactured conformal mask featuring raised bridges. Several fabrication challenges arose during the coating step, relating to conformality of the conformal mask and the heat generated through the conductive coating process. After a successful coating through the conformal mask, filtering characteristics of the conformal FSS were confirmed via experiment. A further demonstration of the capabilities of conformal masking was shown with the fabrication of a conformal patch antenna array. The patch array was first designed for a planar surface, then modified to retain its performance when forced onto a highly non-planar geometry. Both the planar and conformal arrays were fabricated and tested, with good agreement between simulation and measurement results.

Chapter 6

Conclusion

In this thesis, I have demonstrated the fabrication of 3D metamaterials, non-planar patterned geometries and constructed several electromagnetic devices. In this final chapter, I summarize the underlying metamaterial challenges that led to the device designs and experimental results presented herein, and reiterate the thesis contributions. Finally, I conclude with a brief section devoted to future work based on this research.

6.1 Metamaterial Fabrication

Metamaterials have revolutionized the design of electromagnetic systems, but their practical application remains limited by the effective parameters of metamaterial structures that we can actually fabricate. Standard PCB and semiconductor manufacturing processes are sufficient for producing 2D prototypes of metamaterials, but these have limited application in three dimensions.

In this thesis, I explored both the design of 3D metamaterial unit cells, and located the manufacturing tools and techniques necessary to fabricate them.

- Additive Manufacturing: A suite of fabrication processes capable of producing 3D structures that have intrinsic metamaterial function, or are able to support modular metamaterial placements in a 3D array.
- Metallization: Methods to introduce material heterogeneity into otherwise homoge-

neous 3D structures.

- Conformal Masks: Masks to ensure the precise placement of said material inhomogeneity on non-planar surfaces to generate a desired electromagnetic response.

6.2 Summary of Contributions

I began my study of 3D metamaterials by pursuing an artificial magnetic conductor substrate to improve the performance of UHF RFID tags in close proximity to metal surfaces. Toward that objective, I introduced a 3D split ring AMC unit cell, an array of which was fixtured in a custom designed scaffold produced using additive manufacturing. Experiments confirmed the AMC operated at 0.92 GHz and enhanced near metal antenna performance.

I continued to explore the use of additive manufacturing to prototype a metamaterial S-ring array, which became the basis for a 3D plano-concave negative index lens consisting of over 4000 unit cells. I showed experimentally that the constituent S-rings contributed negligible dissipation losses, resulting in the lens focal field gain being higher than any other metamaterial lens reported to date.

Finally, I introduced a new fabrication method called Conformal Masking, a method to generate conformal stencil structures and pattern complex non-planar surface geometries. In combination with graphical and electromagnetic simulation software, I designed and fabricated conformal masks to pattern a paraboloid radome with frequency selective elements, and optimize the performance of a patch antenna array that conformed to a highly non-planar substrate.

The specific contributions of my thesis are as follows. I have

- designed and fabricated a 3D unit cell for use as an AMC for UHF RFID,
- proposed an updated lumped element model for AMC design and analysis,
- proposed the use of Additive Manufacturing to produce scaffolds for the precise placement of metamaterial unit cells or modules,

- fabricated a 3D S-ring metamaterial unit cell array using a combination of additive manufacturing and conductive coating techniques that was measured to have low loss,
- fabricated a plano-concave lens using self-supporting 3D S-ring metamaterials that was measured to have the highest gain of any metamaterial lens to date,
- outlined a new patterning process for non-planar surfaces called Conformal Masking,
- used a conformal mask to produce an FSS on a paraboloid surface,
- used a conformal mask to produce a patch antenna array on a non-planar surface.

6.3 Future Work

The contributions of this thesis pave the way towards practical metamaterial devices, devices that will provide performance enhancements in addition to being aesthetic physical demonstrations. In this section, I outline the directions were I hope to take this work in the near future, beginning with extensions to the projects presented in the previous three chapters, and concluding with a general vision of where the ideas and methods presented in this thesis may lead.

6.3.1 Thin AMC Manufacturing

In chapter 3, I presented a 3D AMC unit cell in contrast to the planar PCB based designs employed in other works. While a 5 mm thick AMC substrate was shown to enhance antenna performance, my efforts to reduce the thickness were confounded by reduced bandwidths and fabrication difficulties. The ensuing analysis of AMC bandwidth in relation to unit cell geometry led to the conclusion that AMC bandwidth is limited by substrate thickness and capacitance per unit area. While both planar and 3D AMC designs are capable of satisfying the capacitance requirement, the film thicknesses required are significantly thinner than those available through commercial PCB fabrication venues. The aim of future work in this area will be to evaluate thin, low area unit cell designs, and evaluate prototypes with an eye towards mass production and cost targets that meet the requirements of the RFID industry.

6.3.2 Self-Supporting Metamaterials Devices

In chapter 4, I presented a high gain plano-concave lens made from self-supporting S-ring metamaterial layers. This work can be extended to other lenses fabricated using similar methods but with varied cell structure, surface curvature, focal length, gradient index of refraction, and frequency band of operation. The extent to which the operating frequency can be shifted up the spectrum is dependent on both the capabilities of employed additive manufacturing systems, and high frequency properties of available conductive materials. How far today's processes and materials can be extended while retaining performance and low loss is of primary concern.

In addition to variations on the S-ring metamaterial lens theme, additive manufacturing at the macro scale is a process which enables the investigation of alternative low-loss 3D metamaterial structures for other applications. This includes structures that may be polarization insensitive, or capable of extension in all three spatial directions resulting in bulk 3D material media, as opposed to the assembly of individual 3D S-ring layers.

While additive manufacturing is key to the rapid prototyping of 3D metamaterials, it is not a cost effective method of mass production. To that end, in the future we hope to investigate the utilization of alternative fabrication methods such as casting or injection molding, which are well suited for producing self-supporting, interconnected structures.

6.3.3 Conformal Masking Process Development

In chapter 5, I introduced Conformal Masking as a process for patterning non-planar surfaces. While I successfully transferred both an FSS and patch antenna array to curved surfaces using this method, there is much to be done to improve the process and many questions to be answered about process capabilities. One such issue is assessing and maximizing mask conformality, and the steps that can be taken to minimize deviation of the mask from the substrate surface. Potential solutions that require further investigation include the incorporation of independently supported pre-stressed features, compressible mask elements and adhesives. Future work will also define a conformal mask process window by characterizing process accuracy, reliability and repeatability in terms of minimal line widths and edge

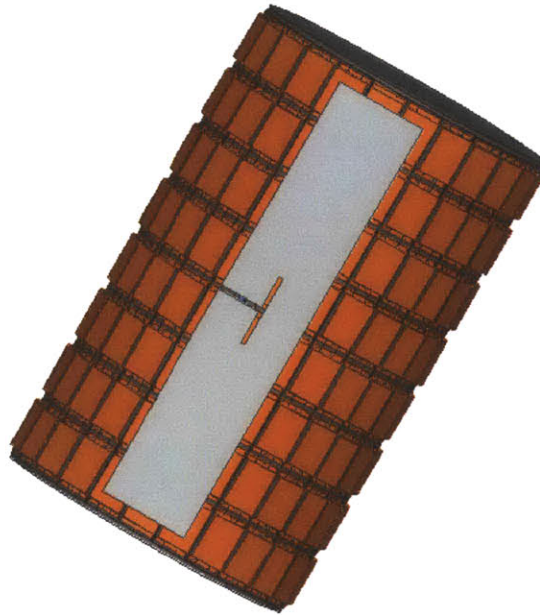


Figure 6-1: A model of a cylindrical array of AMC unit cells held within a cylindrical scaffold.

roughness. Overall, this will involve a design for manufacturing optimization of mask geometries for particular surface curvatures and coating processes.

One method for extending the capabilities of conformal masking is to combine the additive manufacturing based method with other fabrication methods. Castings of conformal masks can be produced to improve mask structural properties, as well as produce multiple masks via a more economical process. Another extension of Conformal masks may involved the integrations of mask modules produced using micro-stereolithography, to facilitate a reduction in linewidth.

6.3.4 Combining 3D and Non-Planar

While the AMC of chapter 3 and S-ring arrays of chapter 4 were certainly three-dimensional, they were only presented in the form of a planar array, or as a stack of planar arrays. As evidenced by the curvilinear geometries of chapter 5, there is no need to limit the fabrication of Split Ring AMCs or S-rings to such planar planar geometries. Indeed, these arrays of 3D structures can be altered to conform to cylinders, spheres, or more general curvilinear surfaces(Fig. 6-1).

6.3.5 Changing the Mindset

As I showed in my thesis, additive manufacturing is a useful tool for realizing metamaterials and other electromagnetic structures that would be difficult to fabricate using other methods, useful despite its intended mechanically or artistically oriented audience. In order for additive manufacturing to open itself to electromagnetic development, I propose that research and industry efforts into tomorrow's additive manufacturing broaden their mindset to incorporate the needs of the electromagnetic community, including

- full frequency dependent characterization of measurable electromagnetic properties for all materials used in additive manufacturing
- development of new materials with optimized electromagnetic properties
- development of systems capable of using multiple structural materials of varied electromagnetic properties
- development of robust systems that incorporated conductive and dielectric materials in the same job

Research in these directions will create the fabrication tools and materials necessary to build the next generation of 3D electromagnetic devices.

Bibliography

- [1] C. Caloz and T. Itoh, *Electromagnetic Metamaterials: Transmission Line Theory and Microwave Applications*. John Wiley & Sons, 2005.
- [2] G. V. Eleftheriades and K. G. Balmain, eds., *Negative-Refractive Metamaterials: Fundamental Principles and Applications*. John Wiley & Sons, 2005.
- [3] M. A. Saville, *Investigation of Conformal High Impedance Ground Planes*. PhD thesis, Air Force Institute of Technology, 2000.
- [4] J. A. Kong, *Electromagnetic Wave Theory*. EMW, 2008.
- [5] T. J. Cui, D. R. Smith, and R. Liu, eds., *Metamaterials: theory, design, and applications*. Springer, 2010.
- [6] S. Enoch, G. Tayeb, P. Sabouroux, N. Guérin, and P. Vincent, “A metamaterial for directive emission,” *Phys. Rev. Lett.*, vol. 89, p. 213902, 2002.
- [7] R. Ziolkowski and A. Kipple, “Application of double negative materials to increase the power radiated by electrically small antennas,” *Antennas and Propagation, IEEE Transactions on*, vol. 51, no. 10, pp. 2626 – 2640, 2003.
- [8] B. Wu, W. Wang, J. Pacheco, X. Chen, T. M. Grzegorzczuk, and J. A. Kong, “A study of using metamaterials as antenna substrate to enhance gain,” *Progress In Electromagnetics Research*, vol. 51, pp. 295–328, 2005.
- [9] B.-I. Wu, H. Chen, J. A. Kong, and T. M. Grzegorzczuk, “Surface wave suppression in antenna systems using magnetic metamaterial,” *Journal of Applied Physics*, vol. 101, no. 11, 2007.
- [10] B. Zhang, B.-I. Wu, and H. Chen, “High directive antenna with virtual aperture,” in *IEEE Antennas and Propagation Society International Symposium*, pp. 1 –4, 2009.
- [11] D. Sievenpiper, L. Zhang, R. Broas, N. Alexopolous, and E. Yablonovitch, “High-impedance electromagnetic surfaces with a forbidden frequency band,” *Microwave Theory and Techniques, IEEE Transactions on*, vol. 47, no. 11, pp. 2059 –2074, 1999.
- [12] D. Sievenpiper, J. Schaffner, H. Song, R. Loo, and G. Tagonan, “Two-dimensional beam steering using an electrically tunable impedance surface,” *Antennas and Propagation, IEEE Transactions on*, vol. 51, no. 10, pp. 2713 – 2722, 2003.

- [13] Z. Duan, B. Wu, J. Kong, F. Kong, and S. Xi, "Enhancement of radiation properties of a compact planar antenna using transformation media as substrates," *Progress In Electromagnetics Research*, vol. 83, pp. 375–384, 2008.
- [14] P.-H. Tichit, S. N. Burokur, D. Germain, and A. de Lustrac, "Design and experimental demonstration of a high-directive emission with transformation optics," *Phys. Rev. B*, vol. 83, p. 155108, 2011.
- [15] E. Hecht, *Optics*. Addison-Wesley, 2001.
- [16] J. B. Pendry, "Negative refraction makes a perfect lens," *Phys. Rev. Lett.*, vol. 85, pp. 3966–3969, 2000.
- [17] N. Fang, H. Lee, C. Sun, and X. Zhang, "Subdiffraction-limited optical imaging with a silver superlens," *Science*, vol. 308, no. 534, 2005.
- [18] S. Rudolph and A. Grbic, "Super-resolution focusing using volumetric, broadband nri media," *Antennas and Propagation, IEEE Transactions on*, vol. 56, no. 9, pp. 2963–2969, 2008.
- [19] J. Pendry, D. Schurig, and D. Smith, "Controlling electromagnetic fields," *Science*, vol. 312, no. 5781, pp. 1780–1782, 2006.
- [20] U. Leonhardt, "Optical conformal mapping," *Science*, vol. 312, pp. 1777–1780, 2006.
- [21] C. Soukoulis, S. Linden, and M. Wegener, "Past achievements and future challenges in the development of three-dimensional photonic metamaterials," *Nature Photonics*, vol. 5, no. 523, 2011.
- [22] H. Chen, Z. Liang, P. Yao, X. Jiang, H. Ma, and C. T. Chan, "Extending the bandwidth of electromagnetic cloaks," *Phys. Rev. B*, vol. 76, p. 241104, 2007.
- [23] C. Brewitt-Taylor, "Limitation on the bandwidth of artificial perfect magnetic conductor surfaces," *Microwaves, Antennas Propagation, IET*, vol. 1, no. 1, pp. 255–260, 2007.
- [24] S. O'Brien and J. B. Pendry, "Magnetic activity at infrared frequencies in structured metallic photonic crystals," *Journal of Physics: Condensed Matter*, vol. 14, p. 6383, 2002.
- [25] J. Pendry, A. Holden, D. Robbins, and W. Stewart, "Magnetism from conductors and enhanced nonlinear phenomena," *Microwave Theory and Techniques, IEEE Transactions on*, vol. 47, no. 11, pp. 2075–2084, 1999.
- [26] J. Pendry, A. Holden, D. Robbins, and W. Stewart, "Low frequency plasmons in thin-wire structures," *Journal of Physics: Condensed Matter*, vol. 10, p. 4785, 1998.
- [27] R. Shelby, D. Smith, and S. Schultz, "Experimental verification of a negative index of refraction," *Science*, vol. 292, pp. 77–79, 2001.

- [28] S. Z. Jason Valentine, T. Zentgraf, E. Ulin-Avila, D. A. Genov, G. Bartal, and X. Zhang, "Three-dimensional optical metamaterial with a negative refractive index," *Nature*, vol. 455, pp. 376–379, 2008.
- [29] V. M. S. Alexandra Boltasseva, "Fabrication of optical negative-index metamaterials: Recent advances and outlook," *Metamaterials*, vol. 2, pp. 1–17, 2008.
- [30] Z. Lu, J. A. Murakowski, C. A. Schuetz, S. Shi, G. J. Schneider, and D. W. Prather, "Three-dimensional subwavelength imaging by a photonic-crystal flat lens using negative refraction at microwave frequencies," *Phys. Rev. Lett.*, vol. 95, no. 15, 2005.
- [31] S. Kalpakjian and S. R. Schmid, *Manufacturing Engineering and Technology*. Prentice Hall, 2010.
- [32] H. Wang, M. Cima, B. Kernan, and E. Sachs, "Alumina-doped silica gradient-index (grin) lenses by slurry-based three-dimensional printing," *Journal of Non-Crystalline Solids*, vol. 349, no. 360, 2004.
- [33] M. Liang, W. Ng, K. Chang, M. Gehm, and H. Xin, "An x-band luneburg lens antenna fabricated by rapid prototyping technology," in *IEEE Microwave Symposium Digest*, 2011.
- [34] P. Mercure, P. Haley, A. Bogle, and L. Kempel, "Three-dimensional isotropic metamaterials," in *Antennas and Propagation Society International Symposium*, vol. 1B, pp. 623–626, 2005.
- [35] S. Rudolph, C. Pfeiffer, and A. Grbic, "Design and free-space measurements of broadband, low-loss negative-permeability and negative-index media," *Antennas and Propagation, IEEE Transactions on*, vol. 59, no. 8, pp. 2989–2997, 2011.
- [36] D. M. Dobkin, *The RF in RFID: Passive UHF RFID in Practice*. Newnes, 2008.
- [37] T. Rappaport, *Wireless communications : principles and practice*. Prentice Hall, 2002.
- [38] K. Rao, P. Nikitin, and S. Lam, "Antenna design for uhf rfid tags: a review and a practical application," *Antennas and Propagation, IEEE Transactions on*, vol. 53, no. 12, pp. 3870 – 3876, 2005.
- [39] J. Griffin, G. Durgin, A. Haldi, and B. Kippelen, "Rf tag antenna performance on various materials using radio link budgets," *Antennas and Wireless Propagation Letters, IEEE*, vol. 5, no. 1, pp. 247–250, 2006.
- [40] S. Best, "Improving the performance properties of a dipole element closely spaced to a pec ground plane," *Antennas and Wireless Propagation Letters, IEEE*, vol. 3, pp. 359 – 363, 2004.
- [41] D. Deavours, "Improving the near-metal performance of uhf rfid tags," in *IEEE International Conference on RFID*, pp. 187–194, 2010.

- [42] M. Hausladen, T. Nash, N. Mitchell, and J. Duffy, "Rfid composite for mounting on or adjacent metal objects," 2002.
- [43] M. Hirvonen, P. Pursula, K. Jaakkola, and K. Laukkanen, "Planar inverted-f antenna for radio frequency identification," *Electronics Letters*, vol. 40, no. 14, pp. 848 – 850, 2004.
- [44] T. Bjorninen, K. Delzo, L. Ukkonen, A. Elsherbeni, and L. Sydanheimo, "Long range metal mountable tag antenna for passive uhf rfid systems," in *RFID-Technologies and Applications (RFID-TA), 2011 IEEE International Conference on*, pp. 202 –206, 2011.
- [45] D. Sievenpiper, H.-P. Hsu, J. Schaffner, G. Tangonan, R. Garcia, and S. Ontiveros, "Low-profile, four-sector diversity antenna on high-impedance ground plane," *Electronics Letters*, vol. 36, no. 16, pp. 1343 –1345, 2000.
- [46] A. Sanada, C. Caloz, and T. Itoh, "Planar distributed structures with negative refractive index," *Microwave Theory and Techniques, IEEE Transactions on*, vol. 52, no. 4, pp. 1252 – 1263, 2004.
- [47] D. W. D.J. Kern, "A genetic algorithm approach to the design of ultra-thin electromagnetic bandgap absorbers," *Microwave and Optical Technology Letters*, vol. 38, p. 6164, 2003.
- [48] D. Kern, D. Werner, A. Monorchio, L. Lanuzza, and M. Wilhelm, "The design synthesis of multiband artificial magnetic conductors using high impedance frequency selective surfaces," *Antennas and Propagation, IEEE Transactions on*, vol. 53, pp. 8 – 17, jan. 2005.
- [49] D. W. D. J. Kern, "Magnetic loading of ebg amc ground planes and ultrathin absorbers for improved bandwidth performance and reduced size," *Microwave and Optical Technology Letters*, vol. 48, pp. 2468 – 2471, 2006.
- [50] B. Gao, K. Cheung, C. Wong, M. Yuen, and R. Murch, "Ultrathin low cost electromagnetic band gap (ebg) materials as uhf rfid tag substrate," in *International Conference on Electronic Materials and Packaging*, pp. 1 –4, 2006.
- [51] B. Gao, C. H. Cheng, M. Yuen, and R. Murch, "Low cost passive uhf rfid packaging with electromagnetic band gap (ebg) substrate for metal objects," in *Electronic Components and Technology Conference, 2007. ECTC '07. Proceedings. 57th*, pp. 974 –978, 2007.
- [52] B. Gao and M. Yuen, "Passive uhf rfid with ferrite electromagnetic band gap (ebg) material for metal objects tracking," in *Electronic Components and Technology Conference, 2008. ECTC 2008. 58th*, pp. 1990 –1994, 2008.
- [53] B. Gao and M. M. F. Yuen, "Passive uhf rfid packaging with electromagnetic band gap (ebg) material for metallic objects tracking," *Components, Packaging and Manufacturing Technology, IEEE Transactions on*, vol. 1, no. 8, pp. 1140 –1146, 2011.

- [54] M. de Cos, F. Las Heras, and M. Franco, "Design of planar artificial magnetic conductor ground plane using frequency-selective surfaces for frequencies below 1 ghz," *Antennas and Wireless Propagation Letters, IEEE*, vol. 8, pp. 951–954, 2009.
- [55] T. Konishi, T. Miura, Y. Numata, S. Sato, A. Sanada, and H. Kubo, "An impedance matching technique of a uhf-band rfid tag on a high-impedance surface with parasite elements," in *Radio and Wireless Symposium, 2009. RWS '09. IEEE*, pp. 67–70, 2009.
- [56] A. Erentok, P. Luljak, and R. Ziolkowski, "Characterization of a volumetric metamaterial realization of an artificial magnetic conductor for antenna applications," *Antennas and Propagation, IEEE Transactions on*, vol. 53, no. 1, pp. 160–172, 2005.
- [57] A. Erentok, D. Lee, and R. Ziolkowski, "Numerical analysis of a printed dipole antenna integrated with a 3-d amc block," *Antennas and Wireless Propagation Letters, IEEE*, vol. 6, pp. 134–136, 2007.
- [58] F. Cox, V. Sharma, A. Klibanov, B.-I. Wu, J. Kong, and D. Engels, "A method to investigate non-thermal effects of radio frequency radiation on pharmaceuticals with relevance to rfid technology," in *28th Annual International Conference of the IEEE Engineering in Medicine and Biology Society*, pp. 4340–4343, 2006.
- [59] F. Yang and Y. Rahmat-Samii, "Reflection phase characterizations of the ebg ground plane for low profile wire antenna applications," *Antennas and Propagation, IEEE Transactions on*, vol. 51, no. 10, pp. 2691–2703, 2003.
- [60] H. Mosallaei and K. Sarabandi, "Antenna miniaturization and bandwidth enhancement using a reactive impedance substrate," *Antennas and Propagation, IEEE Transactions on*, vol. 52, no. 9, pp. 2403–2414, 2004.
- [61] M. Samani and R. Safian, "On bandwidth limitation and operating frequency in artificial magnetic conductors," *Antennas and Wireless Propagation Letters, IEEE*, vol. 9, pp. 228–231, 2010.
- [62] F. Costa, S. Genovesi, and A. Monorchio, "On the bandwidth of high-impedance frequency selective surfaces," *Antennas and Wireless Propagation Letters, IEEE*, vol. 8, pp. 1341–1344, 2009.
- [63] V. Korenivski and R. B. van Dover, "Magnetic film inductors for radio frequency applications," *J. Appl. Phys.*, vol. 82, p. 5247, 1997.
- [64] C. Soukoulis, S. Linden, and M. Wegener, "Negative refractive index at optical wavelengths," *Science*, vol. 315, no. 47, 2007.
- [65] N. I. Zheludev, "The road ahead for metamaterials," *Science*, vol. 328, no. 5978, pp. 582–583, 2010.
- [66] B. Burckel, J. Wendt, G. Eyck, R. Ellis, I. Brener, and M. Sinclair, "Fabrication of 3d metamaterial resonators using self-aligned membrane projection lithography," *Advanced Materials*, vol. 22, pp. 3171–3175, 2010.

- [67] D. Gney, T. Koschny, M. Kafesaki, and C. Soukoulis, "Connected bulk negative index photonic metamaterials," *Optics Letters*, vol. 34, no. 506, 2009.
- [68] D. Gney, T. Koschny, M. Kafesaki, and C. Soukoulis, "Intra-connected three-dimensionally isotropic bulk negative index photonic metamaterial," *Optics Express*, vol. 18, no. 12348, 2010.
- [69] C. Soukoulis and M. Wegener, "Optical metamaterials more bulky and less lossy," *Science*, vol. 330, no. 1633, 2010.
- [70] H. Chen, L. Ran, J. Huangfu, X. Zhang, K. Chen, T. M. Grzegorzczuk, and J. A. Kong, "Left-handed materials composed of only s-shaped resonators," *Phys. Rev. E*, vol. 70, p. 057605, 2004.
- [71] X. Cheng, H. Chen, L. Ran, B.-I. Wu, T. M. Grzegorzczuk, and J. A. Kong, "Negative refraction and cross polarization effects in metamaterial realized with bianisotropic s-ring resonator," *Phys. Rev. B*, vol. 76, p. 024402, 2007.
- [72] X. Cheng, H. Chen, T. Jiang, L. Ran, and J. A. Kong, "Free space measurement of the cross-polarized transmission band of a bianisotropic left-handed metamaterial," *Applied Physics Letters*, vol. 92, no. 17, p. 174103, 2008.
- [73] H. Moser, J. A. Kong, L. Jian, H. Chen, G. Liu, M. Bahou, M. Kalaiselvi, S. Maniam, X. Cheng, B. Wu, P. Gu, A. Chen, S. Heussler, S. bin Mahmood, and L. Wen, "Free-standing thz electromagnetic metamaterials," *Optics Express*, vol. 16, pp. 13773–13780, 2008.
- [74] H. Moser, L. Jian, H. Chen, M. Bahou, S. Kalaiselvi, S. Virasawmy, S. Maniam, S. Cheng, S. Heussler, S. bin Mahmood, and B. Wu, "All-metal self-supported thz metamaterial the meta-foil," *Opt. Express*, vol. 17, pp. 23914–23919, 2009.
- [75] H. Chen, L.-X. Ran, B.-I. Wu, J. A. Kong, and T. M. Grzegorzczuk, "Crankled s-ring resonator with small electrical size," *Progress In Electromagnetics Research*, vol. 66, pp. 179–190, 2006.
- [76] X. Chen, T. M. Grzegorzczuk, B.-I. Wu, J. Pacheco, and J. A. Kong, "Robust method to retrieve the constitutive effective parameters of metamaterials," *Phys. Rev. E*, vol. 70, p. 016608, 2004.
- [77] V. G. Veselago, "The electrodynamics of substances with simultaneously negative values of epsilon and mu," *Physics-Uspekhi*, vol. 10, no. 509, pp. 509–514, 1968.
- [78] D. S. D. Schurig, "Negative index lens aberrations," *Phys. Rev. E*, vol. 70, no. 65601, 2004.
- [79] C. Parazzoli, R. Gregor, J. Nielsen, M. Thompson, K. Li, A. Vetter, M. Tanielian, and D. Vier, "Performance of a negative index of refraction lens," *Applied Physics Letters*, vol. 84, pp. 3232–3234, 2004.

- [80] R. Greeger, C. Parazzoli, J. Nielsen, M. Thompson, M. Tanielian, D. Vier, S. Schultz, D. Smith, and D. Schurig, "Microwave focusing and beam collimation using negative index of refraction lenses," *IET Microwaves, Antennas, Propagation*, vol. 1, pp. 108–115, 2007.
- [81] M. Beruete, M. Navarro-Cía, M. Sorolla, and I. Campillo, "Planoconcave lens by negative refraction of stacked subwavelength hole arrays," *Opt. Express*, vol. 16, pp. 9677–9683, 2008.
- [82] D. J. Gregoire, "3d artificial impedance surfaces," in *IEEE Antennas and Propagation Society International Symposium*, pp. 1 –2, 2012.
- [83] H. In, S. Kumar, Y. Shao-Horn, and G. Barbastathis, "Nanostructured origami: 3d fabrication and assembly of electrochemical energy storage devices," in *Nanotechnology, 2005. 5th IEEE Conference on*, pp. 374 – 377 vol. 1, 2005.
- [84] J.-H. Cho, M. Keung, N. Verellen, L. Lagae, V. Moshchalkov, P. Van-Dorpe, and D. Gracias, "Nanoscale origami for 3d optics," *small*, vol. 7, pp. 1943–1948, 2011.
- [85] K. Cheung, E. Demaine, J. Bachrach, and S. Griffith, "Programmable assembly with universally foldable strings (moteins)," *Robotics, IEEE Transactions on*, vol. 27, no. 4, pp. 718 –729, 2011.
- [86] E. Lieberman-Aiden, N. L. van Berkum, L. Williams, M. Imakaev, T. Ragoczy, A. Telling, I. Amit, B. R. Lajoie, P. J. Sabo, M. O. Dorschner, R. Sandstrom, B. Bernstein, M. A. Bender, M. Groudine, A. Gnirke, J. Stamatoyannopoulos, L. A. Mirny, E. S. Lander, and J. Dekker, "Comprehensive mapping of long-range interactions reveals folding principles of the human genome," *Science*, vol. 326, no. 5950, pp. 289–293, 2009.
- [87] S. Wang, J. Xiao, J. Song, H. Ko, K. Hwang, Y. Huang, and J. Rogers, "Mechanics of curvilinear electronics," *Soft Matter*, vol. 6, 2010.
- [88] J. Adams, E. Duoss, T. Malkowski, M. Motala, B. Y. Ahn, R. Nuzzo, J. Bernhard, , and J. Lewis, "Conformal printing of electrically small antennas on three-dimensional surfaces," *Advanced Materials*, vol. 20, 2011.
- [89] N. P. Pham, E. Boellaard, J. Burghartz, and P. Sarro, "Photoresist coating methods for the integration of novel 3-d rf microstructures," *Microelectromechanical Systems, Journal of*, vol. 13, no. 3, pp. 491 – 499, 2004.
- [90] J. Kim, N. Takama, B. Kim, and H. Fujita, "Optical-softlithographic technology for patterning on curved surfaces," *J. Micromech. Microeng*, vol. 19, 2009.
- [91] B. A. Munk, *Frequency Selective Surfaces: Theory and Design*. John Wiley & Sons, 2000.

- [92] S. Scott, C. Nordquist, M. Cich, T. Jordan, and C. Rodenbeck, "A frequency selective surface with integrated limiter for receiver protection," in *Antennas and Propagation Society International Symposium (APSURSI), 2012 IEEE*, pp. 1–2, 2012.
- [93] D. Raynes and J. DeLap, "Design of a finite array with a radome incorporating a frequency selective surface," in *Antennas and Propagation, 2007. EuCAP 2007. The Second European Conference on*, pp. 1–5, 2007.
- [94] T. Cwik and R. Mittra, "The effects of the truncation and curvature of periodic surfaces: a strip grating," *Antennas and Propagation, IEEE Transactions on*, vol. 36, no. 5, pp. 612–622, 1988.
- [95] X. Liu, S. MacNaughton, D. Shrekenhamer, H. Tao, S. Selvarasah, A. Totachawattana, R. Averitt, M. Dokmeci, S. Sonkusale, and W. Padilla, "Metamaterials on parylene thin film substrates: Design, fabrication, and characterization at terahertz frequency," *Appl. Phys. Lett.*, vol. 96, 2010.
- [96] B. Y. Ahn, E. Duoss, M. Motala, X. Guo, S. Park, Y. Xiong, J. Yoon, R. Nuzzo, J. Rogers, and J. Lewis, "Omnidirectional printing of flexible, stretchable, and spanning silver microelectrodes," *Science*, vol. 323, pp. 1590–1593, 2009.
- [97] Source: <http://www.si2technologies.com/absorber-systems/>) as of Jan 1, 2013.
- [98] L. Josefsson and P. Persson, *Conformal Array Antenna Theory and Design*. John Wiley & Sons, 2006.
- [99] C. A. Balanis, *Advanced Engineering Electromagnetics*. John Wiley & Sons, 1989.